Frequency Chirp and Spectral Dynamics in Semiconductor Lasers

Thesis by

Jing Feng

In Partial Fulfillment of the Requirements

for the Degree of

Doctor of Philosophy

California Institute of Technology

Pasadena, California

1997

(Defended August 6, 1996)

To My Parents and Jing

Acknowledgments

I am very grateful to my advisor Professor Yariv for his guidance, patience, and assistance during my graduate career. I have been greatly inspired by his scientific vision and keen physical insight and benefited by his abilities to provide the necessary resources. It truly has been a privilege for me to work with talented students and research fellows in his group. The success of my research can be largely contributed to the open, intellectually stimulating and creative atmosphere Professor Yariv has created and maintained in his laboratories. His encouragement and trust in my abilities have been inspiring me over the years and will always be appreciated.

Special thanks to Professor T.R. Chen who provided most of the lasers for my research and collaborated with me on many projects. I would also like to thank Professor Amir Sa'ar, who introduced me to the experimental world of semiconductor quantum structure devices and taught me device fabrication and measurement techniques. I am grateful to Dr. Bin Zhao, who had spent many days to help me with the experimental set-up for frequency chirp measurement as well as Drs. Lars Eng, Ali Shakouri and Nao Kuze who grew the MBE samples for my experiments.

I would like to express my appreciation to Drs. John Iannelli and Thomas Schrans who closely worked with me on different research projects over the years and with whom I can always consult. Many thanks go to Yuhua Zhang, Drs. Randy Salvatore, Volnei Pedroni, Gert Cauwenberghs, Gilad Almogy, John O'Brien, Xiaolin Tong, Dan

Provenzano, Yuanjian Xu, Bill Marshall, Matthew McAdams, and Reginald Lee. Thanks are also extended to many other current and former members of the group.

I would like to express my appreciation to Jana Mercado, whose administrative assistance was always appreciated very much. The appreciation also goes to Ali Ghaffari, Kevin Cooper, and Paula Samazan.

I owe a great debt to the people who made the experimental work possible. In particular I am grateful to Larry Begay who had skillfully constructed many parts for my experiment. Without his help, it is impossible to imagine that my research could be so fruitful.

Beyond the boundaries of Caltech, I would like to thank Dr. Joe Paslaski, who came to Caltech to help me to adjust the photodiode for my frequency chirp experiment, and Norman Kwong for his expertise in high speed measurement.

This thesis is dedicated to my father, mother, and my wife Jing, whose love, support, expectation, and faith in me have always inspired me for excellence and success. Without their love and support, none of this would have been possible.

Abstract

A study of the effects of the longitudinal distribution of optical intensity and carrier density on the static and dynamic characteristics of semiconductor lasers has been performed. Through a self-consistent way, a static model for above threshold operation of a single mode distributed feedback (DFB) laser is developed by calculating the longitudinal optical intensity and carrier density distribution. A dynamic model for large signal modulation of the DFB laser is also presented based on time-dependent coupled-mode equation for electric traveling waves in the laser. The spatial hole burning (SHB) has been analyzed in a quarter wavelength shifted DFB laser and a conventional DFB laser.

A small-signal model is developed by including the optical intensity and carrier density distributions. Expressions are derived for the intensity modulation and resonance frequency, the frequency chirp and FM modulation, and the linewidth enhancement factor. Theoretical analysis of the frequency chirp in the DFB lasers has been used to support our experimental results. The model has led us to a new understanding of frequency chirp in DFB lasers and discovery of the ultra small chirp lasers.

The spectral dynamics and high speed response of uncooled DFB lasers have been studied. The most distinguished element differentiating the uncooled DFB lasers from uncooled FP lasers is that in uncooled DFB lasers; the wavelength detuning plays an important role in determining their spectral and high speed characteristics at high temperatures. Comparing with lasers lasing at gain peak, the DFB lasers with large negative wavelength detune could have better high speed performance at room temperature, but they might have higher threshold current. We can achieve optimum performance of uncooled DFB lasers by choosing wavelength detuning properly based on the laser applications.

Contents

1 Introduction **1**

1.1 Optical communication systems 2

1.2 Single longitudinal mode semiconductor lasers 5

1.3 Outline of the thesis 6

2 Theoretical Model in Distributed Feedback Lasers **10**

2.1 Introduction 10

2.2 Coupled-mode equations in DFB lasers 12

2.2.1 Effective index approximation for waveguide modes 12

2.2.2 Coupled-mode equations 14

2.3 F-matrix method 16

2.4 Gain, effective index 18

2.5 Carrier and photon density 20

2.6 The lasing condition in DFB lasers 23

3 Numerical Simulation of Distributed Feedback Lasers **28**

3.1 Introduction 28

3.2 Threshold simulation of DFB lasers 30

3.3 Above-threshold simulation 32

3.4 Large signal modeling 39

4 Small Signal and Spectral Characteristics of Distributed Feedback Lasers 47

4.1 Introduction 47

4.2 Solving the coupled-mode equations by Green's Function 48

4.2.1 Green's function for coupled-mode equations 48

4.2.2 Green's function solution for electric field 51

4.2.3 Small signal rate equations 53

4.3 Amplitude modulation 54

4.3.1 Expression for AM modulation in DFB lasers 54

4.3.2 Resonance frequency in single section DFB lasers 55

4.3.3 High speed response in two-section DFB laser 58

4.4 Linewidth, effective linewidth enhancement factor 63

4.5 Conclusion 73

5 Small Frequency Chirp Distributed Feedback Lasers 77

5.1 Introduction 77

5.2 Simple relation between intensity modulation and frequency chirp 79

5.3 Propagation of optical signals in fibers 81

5.3.1 Time-bandwidth product of chirped pulses 81

5.3.2 Transmission of chirped pulses over single-mode fibers 83

5.4 Theoretical foundation of the frequency chirp reduction in two-section DFB lasers 86

5.5 Measurement of the frequency chirp in two-section DFB lasers under small signal modulation 91

5.5.1 Experiment No. 1: Frequency chirp in 1.55μm two-section DFB laser 91

5.5.2 Experiment No. 2: Frequency chirp in 1.3μm InGaAsP/InP quantum well two-section DFB laser 97

5.6 Measurement of the frequency chirp in two-section DFB lasers under large signal modulation 103

5.7 Control of the frequency chirp in DFB lasers 112

5.8 Conclusion 122

6 Spectral Dynamics and High Speed Performance of Uncooled Distributed Feedback Lasers 126

6.1 Introduction 126

6.2 Gain spectrum 129

6.2.1 Gain expression 129

6.2.2 Collisional dephasing time 131

6.2.3 Gain spectrum in detuned DFB lasers 132

6.3 DC characteristics of uncooled DFB lasers 134

6.3.1 Threshold current density 134

6.3.2 Carrier leakage in quantum well lasers 136

6.3.3 Internal loss in quantum well lasers 137

6.3.4 External differential quantum efficiency 138

6.4 Gain spectrum of uncooled DFB laser 139

6.4.1 The measurement of gain spectrum 140

6.4.2 The influence of the corrugation grating on the measured gain spectra 141

6.5 Linewidth enhancement factor, linewidth of uncooled DFB laser 150

6.5.1 Measurement of α factor 150

6.5.2 Calculation of α factor in uncooled DFB lasers 153

6.5.3 Linewidth of uncooled DFB lasers 156

6.6 High speed response of uncooled DFB lasers 159

6.7 Conclusion 165

List of Figures

1.1 A simple intensity-modulated optical fiber communication system 3

1.2 A coherent heterodyne optical fiber communication system 4

2.1 Schematic diagram of DCPBH DFB laser 12

2.2 F-matrix for DFB laser 16

2.3 General DFB laser structure 23

3.1 Algorithm to solve lasing condition 31

3.2 Algorithm for self-consistency above threshold 34

3.3 The photon, electron density and effective index distribution in a quarter wave shifted DFB laser above threshold ($R_f=R_b=0.3$) 36

3.4 The photon, electron density and effective index distribution in a DFB laser above threshold ($R_f=0.1$, $R_b=0.7$) 37

3.5 The photon density distribution in quarter wave shifted DFB lasers with different coupling coefficients above threshold ($R_f=R_b=0.3$) 38

3.6 Optical response of λ/4 phase-shifted DFB laser with pulse current injection 43

3.7 Frequency chirp of λ/4 phase-shifted DFB laser modulated with pulse function for : (a) $\varepsilon=10^{-17}cm^{-3}$, and $10^{-16}cm^{-3}$; (b) $\alpha=2.5$, and 5 44

4.1 The calculated η parameter for DFB lasers 57

4.2 The resonance frequency of a two-section DFB laser versus square root of the optical power for various I_2, the injection current into section two 59

4.3 The damping rate of the DFB laser versus the optical power for various I_2 60

4.4 A measured linewidth as function of P^{-1} in DFB laser 65

4.5 The measured linewidth of a 1.55μm two-section DFB laser at different current ratios 67

4.6 The calculated linewidth of the two-section DFB laser at different current ratio of the two electrodes for various assumed values for facet phases 68

4.7 The calculated threshold and lasing wavelength of the DFB laser 69

4.8 The longitudinal photon distribution in the DFB laser 70

4.9 The calculated effective linewidth enhancement factor of the 1.55μm DFB laser 71

5.1 A two-section distributed feedback semiconductor laser 89

5.2 A 1.55μm two-section DFB laser used in experiment 91

5.3 (a) The measured spectrum width of 1.55μm two-section DFB laser
(b) The calculated chirp of the two-section DFB laser 94

5.4 Calculated photon and carrier densities of the 1.55μm two-section DFB laser 95

5.5 (a) Calculated $C_N(z)$ and (b) calculated $N_1(z)$, $N_1(z) \bullet Im(C_N(z))$ 96

5.6 Experimental setup for measuring FM/AM response in DFB lasers 97

5.7 A typical output intensity from Fabry-Perot interferometer 98

5.8 The measured β/m of 1.3μm InGaAsP/InP QW two-section DFB laser 101

5.9 The phase difference $\theta_2-\theta_1$ as a function of the current density ratio i_2/i_1 from the measured FM spectrum of the two-section DFB laser under AM modulation 102

5.10 Measured threshold of the 1.3μm two-section DFB laser ($L_1=400\mu m$, $L_2=100\mu m$) for various current ratios 104

5.11 Experimental setup for the measurement of the chirp of two-section DFB laser under large signal modulation 106

5.12 The measured frequency chirp of the two-section DFB laser 107

5.13 The calculated frequency chirp for the two-section DFB laser 110

5.14 Optical pulse propagation in optical fibers 113

5.15 Time-averaged power spectra from directly modulated DFB lasers 114

5.16 The measured time-averaged optical power spectrum of a two-section DFB laser at 5 GHz modulation for various injection current distributions 116

5.17 The calculated spectral density of the optical field of a single mode laser under 5 GHz modulation 119

5.18 Calculated photon density and the product of $N_1(z)$ and $Im\{C_N(z)\}$ in the two-section DFB laser 120

5.19 Calculated phase difference $\theta_2-\theta_1$ of the directly modulated two-section DFB laser 121

6.1 Optical gain of 1.3 InGaAsP material as function of wavelength for various carrier densities 129

6.2 The calculated optical gain of 1.3 InGaAsP material as function of wavelength at various temperatures for carrier density $N_C=6x10^{18}cm^{-3}$ 132

6.3 Calculated gain of 1.3μm InGaAsP material as function of injection carrier density for various wavelength detunes 133

6.4 Measured L-I of a 1.3μm InGaAsP/InP QW DFB lasers at various temperatures 136

6.5 The spectrum of a 1.3μm InGaAsP/InP QW DFB laser at 20°C 143

6.6 The spectrum of the DFB laser at 40°C 143

6.7 The spectrum of the DFB laser at 60°C 144

6.8 The spectrum of the DFB laser at 80°C 144

6.9 The spectrum of the DFB laser below threshold for λ=1290 nm-1315 nm 145

6.10 The spectrum of the DFB laser below threshold for λ=1315 nm-1340 nm 145

6.11 The estimated modal gain of the DFB laser at 20°C 146

6.12 The estimated modal gain of the DFB laser at 40°C 146

6.13 The estimated modal gain of the DFB laser at 60°C 147

6.14 The estimated modal gain of the DFB laser at 80°C 147

6.15 Measured wavelength detune of the 1.3μm InGaAsP/InP QW DFB laser at different temperatures 148

6.16 Calculated normalized gain deviation versus normalized deviation 149

6.17 Measured β/m of 1.3μm InGaAsP/InP QW DFB laser as function of modulation frequency at different temperatures 152

6.18 Calculated linewidth enhancement factor of 1.3μm DFB laser as function of temperature 155

6.19 The experimental setup for linewidth measurement 156

6.20 Measured linewidth of 1.3μm InGaAsP/InP QW DFB laser vs. the inverse of optical power at 20°C, 40°C, 60°C, and 80°C 158

6.21 The calculated $dg/dN \bullet g$ as function of temperature in DFB lasers with various wavelength detunes 160

6.22 (a) The measured resonance frequency as function of square root of optical power in 1.3μm DFB laser ($\Delta\lambda_D$=-5 nm) for various temperatures 163

6.22 (b) The measured damping rate as function of optical power in 1.3μm DFB laser 163

6.23 (a) The measured resonance frequency as function of square root of optical power in 1.29μm DFB laser (*$\Delta\lambda_D$=-10 nm*) for various temperatures

(b) The measured damping rate as function of optical power in 1.29μm DFB laser 164

Chapter 1

Introduction

Continuous progress in semiconductor lasers has enhanced the performance of high speed and long haul optical fiber communication systems. The development of the erbium doped fiber amplifier (EDFA) [1-3] also greatly extends the transmission distance of optical signals in fibers. The fastest transmitter has been reported to reach modulation bandwidth of 40 GHz [4]. However, as current digital communication systems approach data rates of 10 Gbits/s, without dispersion compensation, the transmission distance of the optical signals from directly modulated single longitudinal mode (SLM) lasers is severely limited by large laser chirp, typically on the order of 1 Å for large signal modulation. Numerous research efforts are pursuing various approaches for alleviating this problem, such as using external modulators, dispersion compensated fibers [5-6], optical phase conjugation [7-9], and pre-chirped laser pulses [10-12].

In addition to this limitation, the laser transmitters have to satisfy the following conditions to be suitable for long haul, high speed optical communications.

For CATV applications:

- Low threshold current
- Single longitudinal mode (SLM) operation
- Super linearity of the dependence of optical power on injection current
- Narrow linewidth
- Low relative intensity noise (RIN)
- Low harmonic and intermodulation distortions for analog modulation

For digital communications:

- SLM operation at high power
- High modulation bandwidth
- High power operation
- Single mode operation at high power
- High temperature operation (for mid-distance, low cost systems)

1.1 Optical communication systems

Optical communication systems differ in principle from other communication systems only in the frequency range of the carrier wave. The optical carrier frequency is typically ~100

THz, compared with the microwave carrier frequency of ~ 1-10 GHz. A communication system consists of a transmitter, a communication channel, and a receiver. Optical communication systems can be classified into two broad categories: guided and unguided. In guided lightwave systems, the optical beam emitted by the transmitter remains spatially confined. This is achieved by using optical fibers. In unguided optical communication systems, the optical beam emitted by the transmitter spreads in space. In the case of atmospheric propagation, the signal in the unguided systems can deteriorate considerably by scattering from free particles. So, for unguided communication systems, the requirement for the transmitter is quite different from that in guided communication systems. This thesis does not consider unguided optical communication systems.

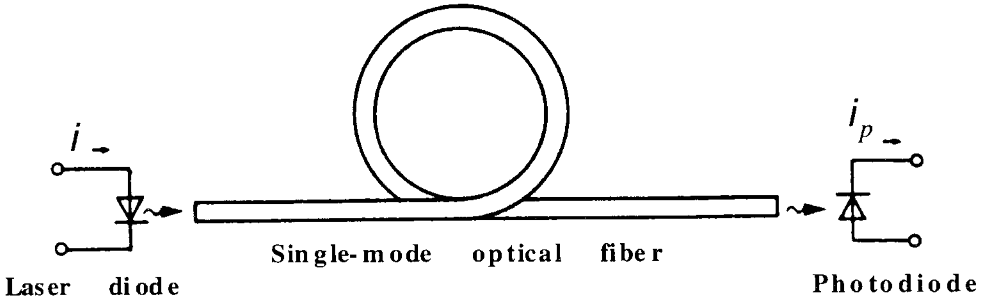

Figure 1.1: A simple intensity-modulated optical fiber communication system.

Fig. 1.1 shows a simple optical fiber communication system, in which the laser diode converts electrical signals into optical signals, which are transmitted by an optical fiber and received by a photodiode. The laser output power is modulated either through direct injection current modulation or through an external modulator. This system is relatively simple in terms of detection schemes.

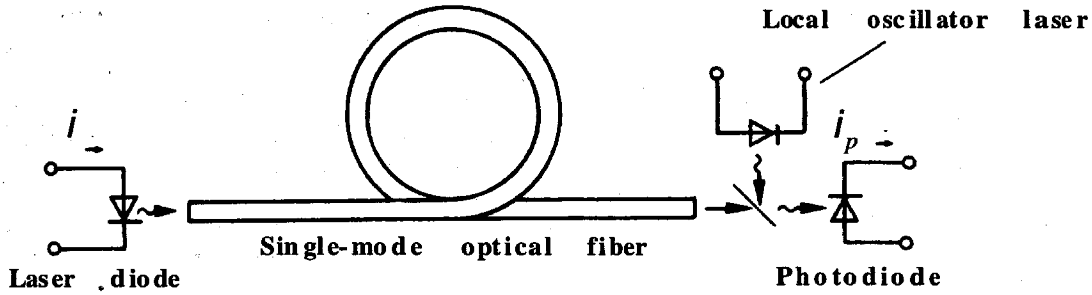

Figure 1.2: A coherent heterodyne optical fiber communication system.

There is a great interest in more sophisticated optical fiber communication systems and especially in coherent optical fiber communication systems. These systems make use of the fact that light is not only characterized by its power but also by its emission frequency or phase. A simple coherent optical fiber system is sketched in Fig. 1.2. The modulated injection current now not only yields a modulation of the optical power, but also of the optical emission frequency. Therefore, the laser diode in Fig. 1.2 will emit a frequency-modulated signal (for digital signals this is denoted as frequency-shift-keying = FSK). At the receiver, the signal will be coherently added to the optical signal of a local oscillator laser. At the photodiode, a beat signal between transmitter laser and local oscillator laser is created and spectrum of the photodiode current peaks at the beat frequency. Therefore, according to the optical frequency modulation of the transmitter, the photodiode current is frequency modulated and may be demodulated by conventional electronic circuits.

1.2 Single longitudinal mode semiconductor lasers

The most widely used SLM lasers are distributed feedback (DFB) lasers, which use a frequency dependent feedback from a corrugation grating (Bragg grating) close to the active layer in the axial direction, to obtain SLM operation above threshold. In such structures an optical wave traveling in the + z -direction is successively reflected by the grating into a wave traveling in the -z-direction and *vise versa.* The opposing traveling waves are strongly coupled with each other due to the existence of the grating. As a result of the coupling between the waves, the optical intensity is not uniform over the whole laser length. Through stimulated emission the optical intensity will induce a nonuniformity in the carrier density distribution and the associated gain and refractive index. The laser characteristics become power dependent through the nonuniform longitudinal distribution of optical power and carrier density.

There have been intensive efforts to improve the material parameters such as linewidth enhancement factor and differential gain for achieving low chirp and high speed lasers [13-16]. Many of these technical achievements are based on joint progress in the material growth technologies and theoretical understanding of quantum well structures. The use of molecular beam epitaxy (MBE) [17] and metal organic chemical vapor deposition (MOCVD) [18-19] to grow ultra thin layers (on the order of ten atomic layers) also paved the way for the development of new types of semiconductor lasers.

To study spectral dynamics and high speed response of semiconductor lasers, most models consider the oversimplified uniform cavity. The complete optical cavity structure is lumped into one parameter, the photon lifetime. One can see from above arguments that it is needed to develop a model, which also considers the longitudinal distributions and their power dependence, for DFB laser transmitters in high speed and long haul optical communication.

1.3 Outline of the thesis

This thesis begins with the investigation of the effects of the longitudinal distributions on the laser characteristics. A comprehensive model for SLM DFB lasers will be developed, where the longitudinal distribution of the power and carrier density will be taken into account in a self-consistent way. Chapter 2 describes the static theory which calculates the power and carrier density distributions in a self-consistent manner. The interaction between the power distribution and carrier density distribution as well as gain and refractive index distributions will be discussed. Chapter 3 introduces the computer algorithms in our calculation of static and dynamic characteristics of DFB lasers. A small-signal dynamic theory is described which includes the longitudinal power and carrier density distributions as well as structural effects.

In Chapter 5, frequency chirp and its measurement in complex devices is analyzed for several two-section DFB lasers with supporting experimental results. A new approach to reduce frequency chirp is described for nonuniform current injection in the DFB lasers.

Lastly, the spectral dynamic and high speed response characteristics of uncooled DFB lasers with wavelength detune are studied theoretically and experimentally.

Reference

[1] E. Desurvire, J.R. Simpson, and P.C. Becker, *Opt. Lett.* 12, 888 (1987)

[2] R.J. Mears, L. Reekie, J.M. Jauncy, and D.N. Payne, *Electron. Lett.* 23, 1026 (1987)

[3] Y. Kimura, K. Suzuki, and M. Nakazawa, *Electron. Lett.* 25, 1656 (1989)

[4] S. Weisser, E.C. Larkin, K. Czotscher, W. Benz, J. Daleiden, I. Esquivias, J. Eleissnser, J.D. Ralston, and B. Romero, *IEEE Phot. Tech. Lett.* 8, 608 (1996)

[5] C. Lin, H. Kogelnik, and L.C. Cohen, *Opt. Lett.* 5, 476 (1980)

[6] H. Izadpanah, C. Lin, J.L. Gimlett, A.J. Anots, D.W. Hall, and D. K. Smith, *Electron. Lett.* 28, 1469 (1992)

[7] A. Yariv, D. Fekete, and D. Pepper, *Opt. Lett.* 4, 52 (1979)

[8] R.A. Fisher, B.R. Suydam, and D. Yevick, *Opt. Lett.* 8, 611 (1983)

[9] S. Watanable, T. Naito, and T. Chikama, *IEEE Phot. Tech. Lett.* 5, 92 (1993)

[10] K. Kishino, S. Aoki, and Y. Suematsu, *IEEE J. Quantum Electron.*, **QE-18**, 343 (1982)

[11] T.L. Koch, and R.C. Alferness, *IEEE J. Lightwave Technol.* **LT-3**, 800 (1985)

[12] N. Henmi, T. Saito, and T. Ishida, *IEEE J. Lightwave Technol.* **LT-10**, 1706 (1994)

[13] Y. Arakawa, and A.Yariv, *IEEE J. Quantum Electron.,* **QE-21**, 1666 (1985)

[14] L.F. Lester, S.S. O'Keefe, W.J. Schaff, and L.F. Eastman, *Electron. Lett.* 28, 383 (1992)

[15] K. Uomi, S. Sasaki, T. Tsuchiya, H. Nakano and N. Chinone, *IEEE Phot. Tech. Lett.* 2, 229 (1990)

[16] H. Yasaka, R. Iga, Y. Noguchi, and Y.Yoshikuni, *IEEE Phot. Tech. Lett.* 4, 825 (1992)

[17] A.Y. Cho, *J. Vac. Sci.* 8, 31 (1971)

[18] R.D. Dupuis, and P.D. Dapkus, *Appl. Phys. Lett.* 31, 466 (1977)

[19] R.D. Dupuis, P.D. Dapkus, N. Holonyak, E.A. Rezek, and R. Chin *Appl. Phys. Lett.* 32, 295 (1978)

Chapter 2

Theoretical Model in Distributed Feedback Lasers

2.1 Introduction

In conventional Fabry-Perot (FP) semiconductor lasers, the feedback is provided by facet reflections whose magnitude remains the same for all longitudinal modes. The only longitudinal mode discrimination in the FP lasers is from gain spectrum. However, since gain spectrum is usually much wider than the longitudinal mode spacing, the mode discrimination is poor. A frequency-dependent feedback [1] is one way to improve the mode selectivity. A distributed feedback laser has either periodic index perturbation (for index-coupled), or gain (loss) perturbation (for gain-coupled) along the lasing axis. The feedback is provided by Bragg scattering, which couples the forward- and backward-propagating waves. Mode selectivity of the DFB lasers results from the Bragg condition.

The Bragg condition states that coherent coupling between the counter-propagating waves occurs only for wavelengths such that the grating period [2]

$$\Lambda = m\lambda/2n_{eff} \tag{2.1}$$

where λ is the free-space wavelength and m is an integer.

Due to the coupling between the counter-propagating waves, the optical intensity in a DFB laser is not uniform, which is known as spatial hole burning (SHB) [3-4]. This nonuniformity in the optical intensity increases with increasingly stronger gratings. Through stimulated emission the optical intensity will induce a nonuniformity in the electron density, which results nonuniformity in gain and refractive index distributions. In this chapter, we will introduce coupled-mode equations and discuss the solving of the coupled-mode equations with F-matrix method. In order to get nonuniform optical intensity, the DFB laser is divided into many small segments and F-matrix method [5] is used to numerically solve the coupled-mode equations. The threshold condition for single longitudinal mode (SLM) DFB laser is developed [6-7]. The longitudinal dependence of the two counter-propagating waves and electron density is solved in a self-consistent way.

2.2 Coupled-mode equations in DFB lasers

2.2.1 Effective index approximation for waveguide modes

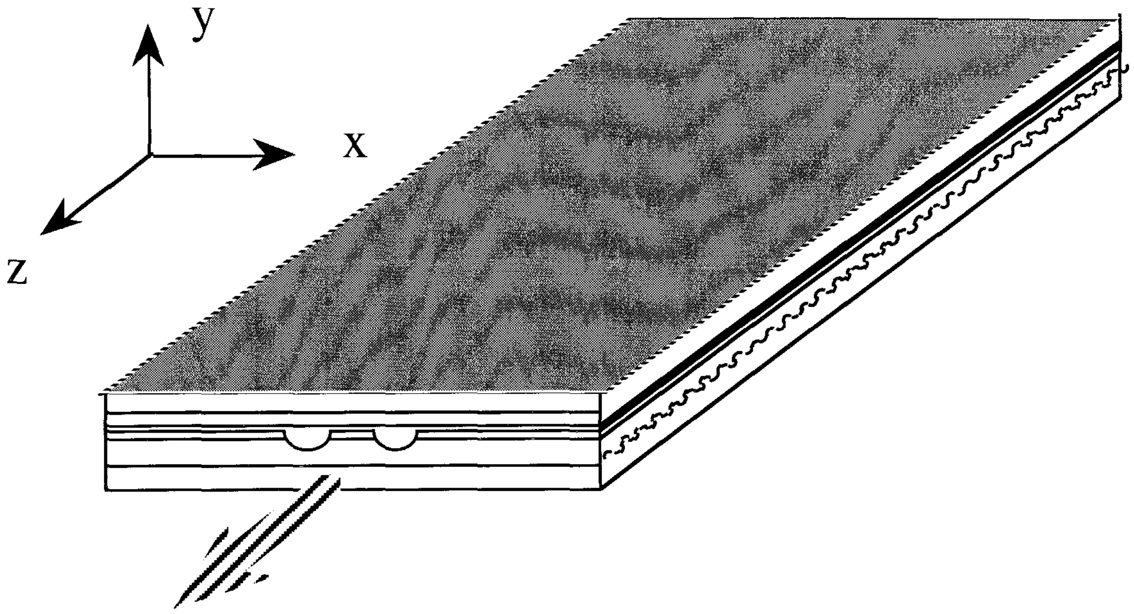

Figure 2.1 Schematic diagram of DCPBH DFB laser.

We start from the time-independent wave equation

$$\nabla^2\mathbf{E}+ \varepsilon(x,y,z)\, k_0^2\mathbf{E} = 0 \tag{2.2}$$

where $k_0=\omega/c$, ω is the mode frequency. ε is a periodic function of z. It is useful to write

$$\varepsilon(x,y,z)=\bar{\varepsilon}\,(x,y)+ \Delta\varepsilon(x,y,z) \tag{2.3}$$

where the dielectric perturbation $\Delta\varepsilon$ is nonzero only over the grating region whose thickness is equal to the corrugation depth. $\bar{\varepsilon}\,(x,y)$ is the average value of ε. The dielectric perturbation can be written as

$$\Delta\varepsilon(x,y,z) = n^2(x,y,z)-\overline{n_0^2}(x,y) -i\frac{\Delta\sigma(x,y,z)}{\omega\,\varepsilon_0} \tag{2.4}$$

where $n^2(x,y,z)$ includes the grating and waveguide, $\overline{n_0^2}(x,y)$ is the index of the waveguide, and $\Delta\sigma(x,y,z)$ is due to gain or loss grating.

In the absence of a grating ($\Delta\varepsilon = 0$) and external pumping, the general solution of (2.2) has the form

$$\mathbf{E}(x,y,z) = \hat{x}\; U(x,y)\; [F\; exp(i\beta z)+R\; exp(-i\beta z)] \tag{2.5}$$

where $\hat{x}$ is the unit vector along the junction plane (for the TE mode) and the field distribution corresponding to a specific waveguide mode is obtained by solving

$$\frac{\partial^2 U(x,y)}{\partial x^2} + \frac{\partial^2 U(x,y)}{\partial y^2} + [\bar{\varepsilon}(x,y)\; k_0^2-\beta^2]U(x,y) = 0 \tag{2.6}$$

for a given device structure, and where β is the mode-propagation constant. For simplicity, we assume that the device supports only the fundamental waveguide mode. To obtain an exact solution of the two-dimensional equation (2.6) is a difficult task. It is essential to make certain simplifying assumptions whose nature and validity vary from device to device. The effective index approximation [8-10] has been frequently used in the problems of semiconductor lasers. Instead of solving the two-dimensional wave equation, the problem is split into two one-dimensional parts whose solutions are relatively easy to obtain. The physical motivation behind the effective index approximation is that the dielectric constant often varies slowly in the lateral x direction compared to its variation in the transverse y direction. The $U(x,y)$ is thus approximated by

$$U(x,y) = \phi(x)\ \Psi(y) \tag{2.7}$$

and (2.6) is rewritten as

$$\frac{1}{\phi(x)}\frac{\partial^2\phi(x)}{\partial x^2}+\frac{1}{\Psi(y)}\frac{\partial^2\Psi(y)}{\partial y^2}+[\bar{\varepsilon}(x,y)\ k_0^2-\beta^2]=0\ . \tag{2.8}$$

In the effective index approximation, we have

$$\frac{1}{\Psi(y)}\frac{\partial^2\Psi(y)}{\partial y^2}+[\bar{\varepsilon}(x,y)\ k_0^2-\beta_{eff}^2(x)]=0 \tag{2.9}$$

$$\frac{1}{\phi(x)}\frac{\partial^2\phi(x)}{\partial x^2}+[\beta_{eff}^2(x)\ -\beta^2]=0 \tag{2.10}$$

For a given laser structure, (2.9) and (2.10) can be used to obtain the transverse and lateral modes, respectively.

$\bar{\varepsilon}\ (x,y)$ includes background (real) refractive index $n_b^2(y)$ which is constant for each layer, and small perturbation $|\delta\bar{\varepsilon}\ (x,y)| \ll n_b^2(y)$ due to the loss and contribution of external pumping.

$$\bar{\varepsilon}\ (x,y) = n_b^2(y) + \delta\bar{\varepsilon}\ (x,y) \tag{2.11}$$

2.2.2 Coupled-mode equations

In presence of the index or gain (loss) grating in single-mode DFB laser, there is some l_0 for which $\beta \approx \frac{\pi l_0}{\Lambda_0} \equiv \beta_0$. Then the electric field is rewritten as

$$\mathbf{E}(x,y,z,t) = \hat{x}\, U(x,y)F(z,t) \tag{2.12}$$

and the transverse electric field is

$$F(z,t) = E^+(z)\exp[-i\beta_0 z + i(\omega_0+\Delta\omega)t] + E^-(z)\exp[+i\beta_0 z + i(\omega_0+\Delta\omega)t] \tag{2.13}$$

where E^+, E^- are the complex field amplitudes of the forward and backward waves, respectively, and ω_0 is the reference frequency. $\beta_0 = 2\pi/\Lambda_0$ for $l_0 = 2$, where Λ_0 is the Bragg wavelength. $\Delta\omega = \omega - \omega_0$, ω is the lasing frequency. The amplitudes E^+, E^- are described by the following coupled-mode equations [2,11,12]:

$$\frac{\partial E^+}{\partial z} = i\kappa E^- - (i\delta + i\Delta\omega/v_g - g + \alpha_{loss})E^+ \tag{2.14}$$

$$-\frac{\partial E^-}{\partial z} = i\kappa E^+ - (i\delta + i\Delta\omega/v_g - g + \alpha_{loss})E^- \tag{2.15}$$

where v_g is the group velocity of light in the active region, κ is the coupling coefficient, g is the optical gain, α_{loss} is the internal loss, and $\delta = \beta - \beta_0$ with β as propagation constant. The coupled-mode equations can be derived from Maxwell's equations using the slowly-varying amplitude approximations. The detailed derivations can be found in [2, 12].

(2.14), (2.15) have not included the spontaneous emission coupled into the lasing mode. This can be solved by adding terms in (2.14), (2.15) to account for spontaneous emission, and the coupled-mode equations with spontaneous emission [7] are

$$\frac{\partial E^+}{\partial z} = i\kappa E^- - (i\delta + i\Delta\omega/v_g - g + \alpha_{loss})E^+ + T^+ \tag{2.16}$$

$$-\frac{\partial E^-}{\partial z} = i\kappa E^+ - (i\delta + i\Delta\omega/v_g - g + \alpha_{loss})E^- + T^- \tag{2.17}$$

$T^\pm$ are the terms due to the spontaneous emission coupled into the lasing mode [7], and

$$T^{\pm} = \frac{J_{sp}}{\left|E^{\pm}\right|^2} E^{\pm} \tag{2.18}$$

where J_{sp} is a constant related to spontaneous emission. $T^{\pm}$ are written here as contributions to the gain and are nonlinear terms.

2.3 F-matrix method

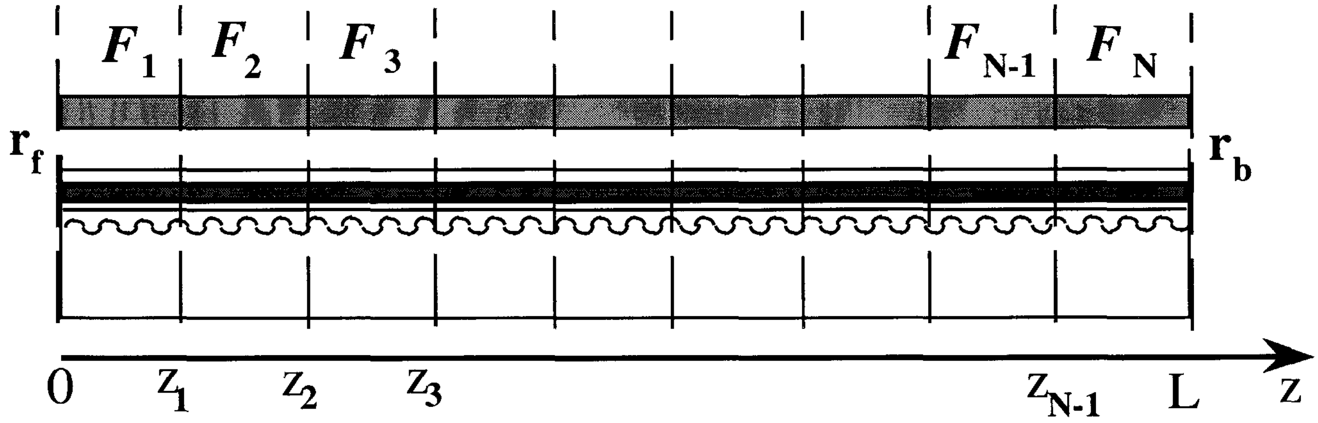

Figure 2.2: F-matrix for DFB laser.

The coupled-mode equations with boundary conditions form an eigenvalue problem with z-dependent coefficients in the differential equations. The electric waves have to be solved numerically. The coupled-mode equations are solved by using the transfer matrix or F-matrix [5] approach, where the DFB laser is divided into many small segments in which the carrier and photon density, optical gain, and effective index are assumed to be constants.

From coupled-mode equations, the electric fields at the output interface of one segment are related to the input fields as

$$\begin{pmatrix} E^{+}(z+\Delta z) \\ E^{-}(z+\Delta z) \end{pmatrix} = \begin{pmatrix} F_{11} & F_{12} \\ F_{21} & F_{22} \end{pmatrix} \begin{pmatrix} E^{+}(z) \\ E^{-}(z) \end{pmatrix} \qquad (2.19)$$

where F is the F-matrix[5] and its elements are

$$F_{11} = \zeta\,[cosh(\gamma\Delta z)+i\frac{D}{\gamma}\,sinh(\gamma\Delta z)] \qquad (2.20)$$

$$F_{12} = i\zeta\,\frac{\kappa}{\gamma}\,sinh(\gamma\Delta z)] \qquad (2.21)$$

$$F_{21} = -i\zeta\,\frac{\kappa}{\gamma}\,sinh(\gamma\Delta z)] \qquad (2.22)$$

$$F_{22} = \zeta\,[cosh(\gamma\Delta z)-i\frac{D}{\gamma}\,sinh(\gamma\Delta z)] \qquad (2.23)$$

where

$$\xi = exp[(g_{sp}^{+}-g_{sp}^{-})\,\Delta z/2] \qquad (2.24)$$

$$D = -(\Delta\omega/v_g+\delta)+i(g-\alpha_{loss}) - i\,(g_{sp}^{+}+g_{sp}^{-}) \qquad (2.25)$$

$$\gamma^2 = [i(\Delta\omega/v_g+\delta)-(g-\alpha_{loss})]^2+\kappa^2 \qquad (2.26)$$

$$g_{sp}^{\pm} = \frac{J_{sp}}{\Delta z}\int_{z}^{z+\Delta z} dz'/\,\left|E^{\pm}(z')\right|^2 \qquad (2.27)$$

The $g_{sp}^{\pm}$ describe the spontaneous emission effects. The F-matrix depends on the carrier density at z via the spontaneous emission, the spatial hole burning, and nonlinear gain suppression.

The propagation equation for the F-matrix is

$$\begin{bmatrix} E^+(z_i) \\ E^-(z_i) \end{bmatrix} = F(z_{i-1})\cdots F(z_1)F(0) \begin{bmatrix} E^+(0) \\ E^-(0) \end{bmatrix} \tag{2.28}$$

which is used to calculate the electric field and photon intensity distribution in a DFB laser.

2.4 Gain, effective index

Conventionally, if the lasing wavelength of a DFB laser is at gain peak, the material gain of the active region is assumed to be linearly dependent on the electron density

$$g_m\,(N) = a\;[N - N_{tr}] \tag{2.29}$$

where a is the material differential gain, and N_{tr} is the transparency density. However, in a DFB laser with wavelength detune, e.g., the Bragg wavelength is designed to be away from the gain peak, the lasing wavelength is not at the gain peak and the material gain as a function of carrier density has to be calculated numerically. By choosing the Bragg wavelength shorter than that of the gain peak, a larger differential gain can be achieved (see detail in Chapter 6). In a wavelength-detuned DFB laser [13], the gain is also dependent on the detune. For carrier density near threshold, the material gain in the DFB laser can be approximated as

$$g_m^{\Delta\lambda}\,(N) = a_{\Delta\lambda}[N - N_{tr}(\Delta\lambda)]\,. \tag{2.30}$$

Here $\Delta\lambda$ is the wavelength detune.

The modal gain is given by [13]

$$g^{\Delta\lambda}(N) = \frac{\Gamma a_{\Delta\lambda}[N-N_{tr}(\Delta\lambda)]}{[\ 1+\varepsilon S\ ]} \tag{2.31}$$

where Γ is the confinement factor and ε is the nonlinear gain suppression coefficient. With considering the SHB in the DFB laser, the photon and carrier densities are not uniform. The gain can be rewritten as

$$g^{\Delta\lambda}(z) = \frac{\Gamma a_{\Delta\lambda}[N(z)-N_{tr}(\Delta\lambda)]}{[\ 1+\varepsilon S(z)\ ]} \tag{2.32}$$

The effective refractive index is a combination of $n^0_{eff}(z)$, which is the value with no injection carriers, and $\Delta n_{eff}\,[N(z)]$, which is the result of the injection carriers.

$$n_{eff}(z) = n^0_{eff}(z) + \Delta n_{eff}\,[N(z)] \tag{2.33}$$

The linear part of the carrier induced index change is often related to the change in the carrier density with the following relation

$$\Delta n_{eff}(N) = -\frac{\alpha\Gamma a\lambda}{4\pi}N \tag{2.34}$$

α is the linewidth enhancement factor for the active layer, and λ is the vacuum wavelength. The effective refractive index is written as

$$n_{eff}(z) = n^0_{eff}(z) - \frac{\alpha\Gamma a\lambda}{4\pi}N(z) \tag{2.35}$$

It will be seen later that, without current modulation, the index dependence on the carrier density results in the shift of the lasing wavelength. With modulation, the index change due to the carrier density variation is the major source for frequency chirp in single mode DFB lasers.

2.5 Carrier and photon density

The carrier recombination will be considered only with respect to spontaneous emission and nonradiative transitions. If the stimulated recombination is not considered, one may set up a simple rate equation for electron density in the active layer:

$$\frac{dN}{dt} = \frac{J}{ed} - R(N) \tag{2.36}$$

with recombination rate being represented by $R(N)$, the injection current density by J. $R(N)$ may be split into the spontaneous emission term $R_{sp}(N)$, non-radiative term $R_{nr}(N)$ and Auger recombination term [14-18]

$$R(N)=R_{sp}(N)+R_{nr}(N)+R_{Auger}(N) \tag{2.37}$$

The spontaneous emission rate is proportional to the product of the number of occupied states in the conduction band ($\sim n$) and the number of vacant electron states in the valence band ($\sim p$). The spontaneous emission term may be written as

$$R_{sp}(N)=Bnp \tag{2.38}$$

where B is a recombination coefficient. To some extent the recombination coefficient B depends on the doping level and decreases with increasing injected carrier density. It is strongly temperature dependent. B has been measured at room temperature and found to be of order of [19-22]

$$B \approx 0.3 \ldots 2.0\times10^{-10} cm^3/s \tag{2.39}$$

for both GaAs and InGaAsP devices. For undoped material we have $n=p=N$ and the spontaneous emission is

$$R_{sp}(N)=BN^2 \tag{2.40}$$

which is often denoted as bimolecular recombination.

The non-radiative term $R_{nr}(N)$ is

$$R_{nr}(N)= A_{nr}N =\frac{N}{\tau} \tag{2.41}$$

τ is the lifetime of monomolecular recombination.

For long-wavelength semiconductor lasers, however, the Auger process is generally the predominated nonradiative mechanism. The Auger recombination process involves four particle (electron and hole) states. In the process, the energy released during the electron-hole recombination is transferred to another electron (or hole), which excites to a high energy state in the band. In low doping material we have $n=p=N$ and the Auger recombination may be approximately written as

$$R_{Auger}(N) = CN^3 \tag{2.42}$$

where the Auger recombination coefficient C is of the order of

$$C \approx 1 \ldots 3\times10^{-29} cm^6/s \tag{2.43}$$

for lightly doped InGaAsP.

In DFB lasers, the carrier and photon density are non-uniform, and the rate equation for carrier density can be written as

$$\frac{dN(z,t)}{dt} = \frac{J(z,t)}{ed} - \frac{N(z,t)}{\tau} - BN(z,t)^2 - CN(z,t)^3 - \frac{a_{\Delta\lambda}[N(z,t)-N_{tr}(\Delta\lambda)]}{[\ 1+\varepsilon S(z,t)\ ]} v_g S(z,t) \tag{2.44}$$

and photon density distribution $S(z)$ is related to the forward and backward waves by

$$S(z) \propto (\ |E^+(z)|^2 + |E^-(z)|^2) \tag{2.45}$$

In (2.44), the stimulated recombination, the last term is also included, and under DC bias, the steady state for carrier density is obtained by setting $dN/dt=0$

$$\frac{J(z)}{ed} - \frac{N(z)}{\tau} - BN(z)^2 - CN(z)^3 - \frac{a_{\Delta\lambda}[N(z)-N_{tr}(\Delta\lambda)]}{[\ 1+\varepsilon S(z)\ ]} v_g S(z) = 0 \tag{2.46}$$

Normally, the photon density distribution is assumed initially. Then, the carrier density and photon density distributions are solved self-consistently by satisfying the lasing condition. The detailed description about solving for the carrier density and photon density distributions is in Chapter 3.

2.6 The lasing condition in DFB lasers

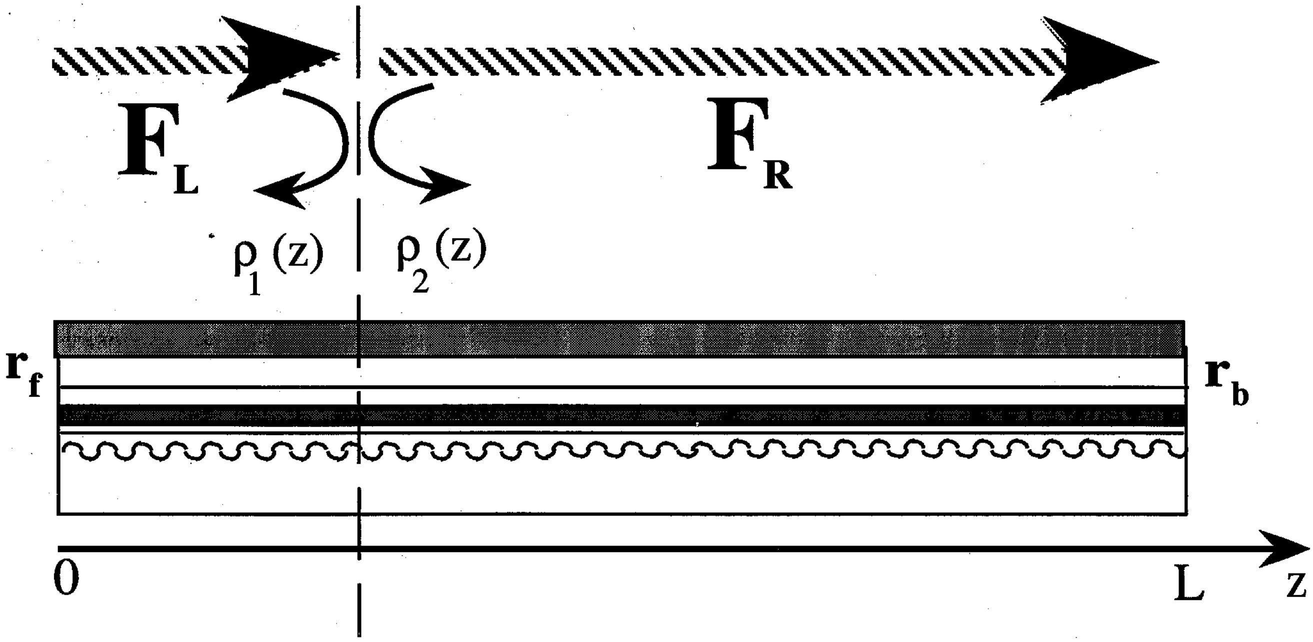

Figure 2.3: General DFB laser structure.

Taking some point z somewhere along the cavity, as shown in Fig. 2.3, the cavity is then divided by two parts, which can be replaced by the effective complex reflectivities, $\widetilde{\rho_1}(z)$ and $\widetilde{\rho_2}(z)$. $\widetilde{\rho_1}(z)$ represents the reflectivity of the left-hand part, and $\widetilde{\rho_2}(z)$ the right-hand part. Those reflectivities depend on the frequency ω and the injected current I. The lasing condition is that the round-trip gain for $\widetilde{\rho_1}(z) \bullet \widetilde{\rho_2}(z)$ should be equal to one:

$$\rho_1(z)\, e^{i\phi_1(z)} \rho_2(z)\, e^{i\phi_2(z)} = 1 \tag{2.47}$$

here $\rho_1(z)$, $\rho_2(z)$, $\phi_1(z)$, $\phi_2(z)$ are the amplitudes and phases of the complex reflection $\widetilde{\rho_1}(z)$, $\widetilde{\rho_2}(z)$.

The $\widetilde{\rho_1}(\mathbf{z})$ and $\widetilde{\rho_2}(\mathbf{z})$ are calculated by means of the propagating matrices $\overrightarrow{F_L}(\omega,I)$, $\overrightarrow{F_R}(\omega,I)$ of the left-hand and right-hand parts of the cavity. The $\widetilde{\rho_1}(\mathbf{z})$,$\widetilde{\rho_2}(\mathbf{z})$ are defined as

$$\widetilde{\rho_1}(z) = \frac{E^-(z)}{E^+(z)} \tag{2.48}$$

and

$$\widetilde{\rho_2}(z) = \frac{E^+(z)}{E^-(z)} \tag{2.49}$$

The boundary conditions are

$$E^-(L)= \widetilde{r_b}\, E^+(L) \tag{2.50}$$

and

$$E^+(0)=\widetilde{r_f}E^-(0). \tag{2.51}$$

Here $\widetilde{r_f}$ and $\widetilde{r_b}$ are the front and back complex facet reflectivities, respectively, and they are given by

$$\widetilde{r_b} = \sqrt{R_b}\; e^{i\phi_b} \tag{2.52}$$

and

$$\widetilde{r_f} = \sqrt{R_f}\; e^{i\phi_f} \tag{2.53}$$

R_f and R_b are front and back facet reflectivities for optical power. ϕ_f and ϕ_b are the phases of the grating at the facets.

The electric fields are derived by forward propagation

$$\begin{aligned}\begin{bmatrix} E_L^+(z) \\ E_L^-(z) \end{bmatrix} &= F(z\text{-}\Delta z)\bullet\bullet\bullet F(\Delta z)F(0)\begin{bmatrix} \tilde{r}_f \\ 1 \end{bmatrix} \\ &= \overrightarrow{F_L}\begin{bmatrix} \tilde{r}_f \\ 1 \end{bmatrix}\end{aligned} \tag{2.54}$$

and backward propagation

$$\begin{aligned}\begin{bmatrix} E_R^+(z) \\ E_R^-(z) \end{bmatrix} &= F(z+\Delta z)\bullet\bullet\bullet F(L\text{-}\Delta z)F(L)\begin{bmatrix} 1 \\ \tilde{r}_b \end{bmatrix} \\ &= \overrightarrow{F_R}\begin{bmatrix} 1 \\ \tilde{r}_b \end{bmatrix}\end{aligned} \tag{2.55}$$

We can get expressions for $\tilde{\rho}_1(\mathbf{z})$,$\tilde{\rho}_2(\mathbf{z})$ [6,7,12] as

$$\tilde{\rho}_1(z) = \frac{\tilde{r}_f(\overrightarrow{F_L})_{11}+(\overrightarrow{F_L})_{12}}{\tilde{r}_f(\overrightarrow{F_L})_{21}+(\overrightarrow{F_L})_{22}} \tag{2.56}$$

$$\tilde{\rho}_2(z) = -\frac{\tilde{r}_b(\overrightarrow{F_R})_{11}-(\overrightarrow{F_R})_{21}}{\tilde{r}_b(\overrightarrow{F_R})_{12}-(\overrightarrow{F_R})_{22}} \tag{2.57}$$

The lasing condition has to be solved numerically to determine the lasing wavelength and the threshold current. Above threshold, the lasing condition is used to calculate the output optical power for a given injection current.

The power level in the laser is set by the output power P_{out}^f from the front facet with

$$P_{out}^f=(1\text{-}|\tilde{r}_f|^2)\ |E^-(0)|^2 \tag{2.58}$$

and the output power P_{out}^b from the back facet is then

$$P_{out}^b= (1\text{-}|\tilde{r}_b|^2)\ |E^+(L)|^2 \tag{2.59}$$

where the fields $E^{\pm}$ have been normalized in $mW^{1/2}$.

Reference

[1] H. Kogelnik, and C.V. Shank, *Appl. Phys. Lett.* 18, 152 (1971)

[2] D. Marcuse, *Theory of Dielectric Optical Waveguide* (Academic Press, 1991), ch.3

[3] J. I. Kinoshita, and K. Matsumoto, *IEEE J. Quantum Electron.*, **QE-24**, 2160 (1988)

[4] H. Soda, Y. Kotaki, H. Sudo, H. Ishikawa, S. Yamakoshi, and H. Imai, *IEEE J. Quantum Electron.*, **QE-23**, 804 (1987)

[5] M. Yamada, and K. Sakuda, *Appl. Opt.* 26, 3474 (1987)

[6] J.E.A. Whiteaway, G.H. Thompson, A.J. Collar, and C. J. Armistead, *IEEE J. Quantum Electron.*, **QE-25**, 1261 (1989)

[7] P. Vankwikelberge, G. Morthier, and R. Baets, *IEEE J. Quantum Electron.*, **QE-26**, 1728 (1990)

[8] R.M. Knox, and P.P. Toulios, *Proc. MRI Symposium on Submillimeter Waves, (ed., J. Fox, Brooklyn, N.Y., Polytechnic Press, 1970)*

[9] W. Streifer and E. Kaon, *Appl. Opt.* 18, 3724 (1979)

[10] J. Buus, *IEEE J. Quantum Electron.*, **QE-18**, 1083 (1982)

[11] A. Yariv, *Optical Electronics, 4th Editon* (Holt, Rinehart and Winton, New York, 1991), ch.13

[12] T. Schrans, *Ph.D. Thesis, California Institute of Technology*, Pasadena, Calif., 1994

[13] H. Nishimoto, M. Yamaguchi, I. Mito, and K. Kobayashi, *IEEE J. Lightwave Technol.* **LT-5**, 1399 (1987)

[14] A.R. Beattie, and P.T. Landsberg, *Proc. R. Soc. London Ser. A.* **249**, 16 (1959)

[15] Y. Horikoshi, and Y. Furukawa, *Jpn. J. Appl. Phys.* **18**, 809 (1979)

[16] G.H. Thompson, and G.D. Henshall, *Electron. Lett.* 16, 42 (1980)

[17] N.K. Dutta, and R.J. Nelson, *Appl. Phys. Lett.* 38, 407(1981)

[18] A. Sugimura, *IEEE J. Quantum Electron.,* **QE-17**, 627 (1981)

[19] R. Slshansky, C.B. Su, J. Manning, and W. Powazinik, *IEEE J. Quantum Electron.* **QE-20**, 838 (1984)

[20] A. P. Mozer, S. Hausser, and M.H. Pikuhn, *IEEE J. Quantum Electron.* **QE-21**, 719 (1985)

[21] H.C. Casey, Jr., and F. Stern, *J. Appl. Phys.* **47**, 631 (1976)

[22] R.J. Nelson, and R.G. Sobers, *J. Appl. Phys.* **49**, 6103 (1978)

Chapter 3

Numerical Simulation of Distributed Feedback Lasers

3.1 Introduction

A computer model for solving the photon and carrier density in DFB lasers is developed in this chapter. The longitudinal dependence of the two counter-propagating waves and electron density is included in a self-consistent way through the dependence of the electron density on the optical intensity and the dependence of the gain and the refractive index on the electron density. The model can be applied to any combination of active and passive sections including distributed feedback from index or loss gratings and reflections from facets or the interfaces between sections. Each section can have z-dependent index and loss coefficients, effective refractive index representing waveguide structure, and current injection. The material gain and the refractive index are assumed to be linear functions of carrier density as described in (2.31) and (2.35).

The algorithms for solving the lasing condition and above threshold [1-12] are presented in this chapter. Characteristics of two semiconductor lasers are discussed. For DFB lasers under large signal modulation, a dynamic model based on the time-dependent coupled-mode equation is developed. The model can be used to calculate the frequency chirp and pulse shape from DFB lasers under large signal modulation.

3.2 Threshold simulation of DFB lasers

With lasing condition (2.47) and the expressions of complex reflectivities for left- and right-hand parts, we can solve the threshold problem for DFB lasers. The laser is divided into many small segments in which the carrier density and refractive index are assumed to be constant. The current complex reflectivities can be calculated by using the F-matrix [13] method. The procedure is shown in Fig. 3.1. For given device and material parameters, the carrier density distribution can be calculated below threshold if the injection current profile is given. Then the round-trip gain is found at a given frequency ω, and we scan the frequency around the Bragg frequency ω_{Bragg} to find the longitudinal modes for which the phase of the round-trip gain is equal to zero. The mode with maximum round-trip gain is to lase, so we adjust the current to make the round-trip gain equal to one. After the round-trip gain is equal to one, we get the threshold current and lasing wavelength. Each time the current is changed, the modes are readjusted to have a round-trip gain phase of zero. This iteration goes until the current with a maximum modal round-trip gain of one is found.

Algorithm to Solve Lasing Condition

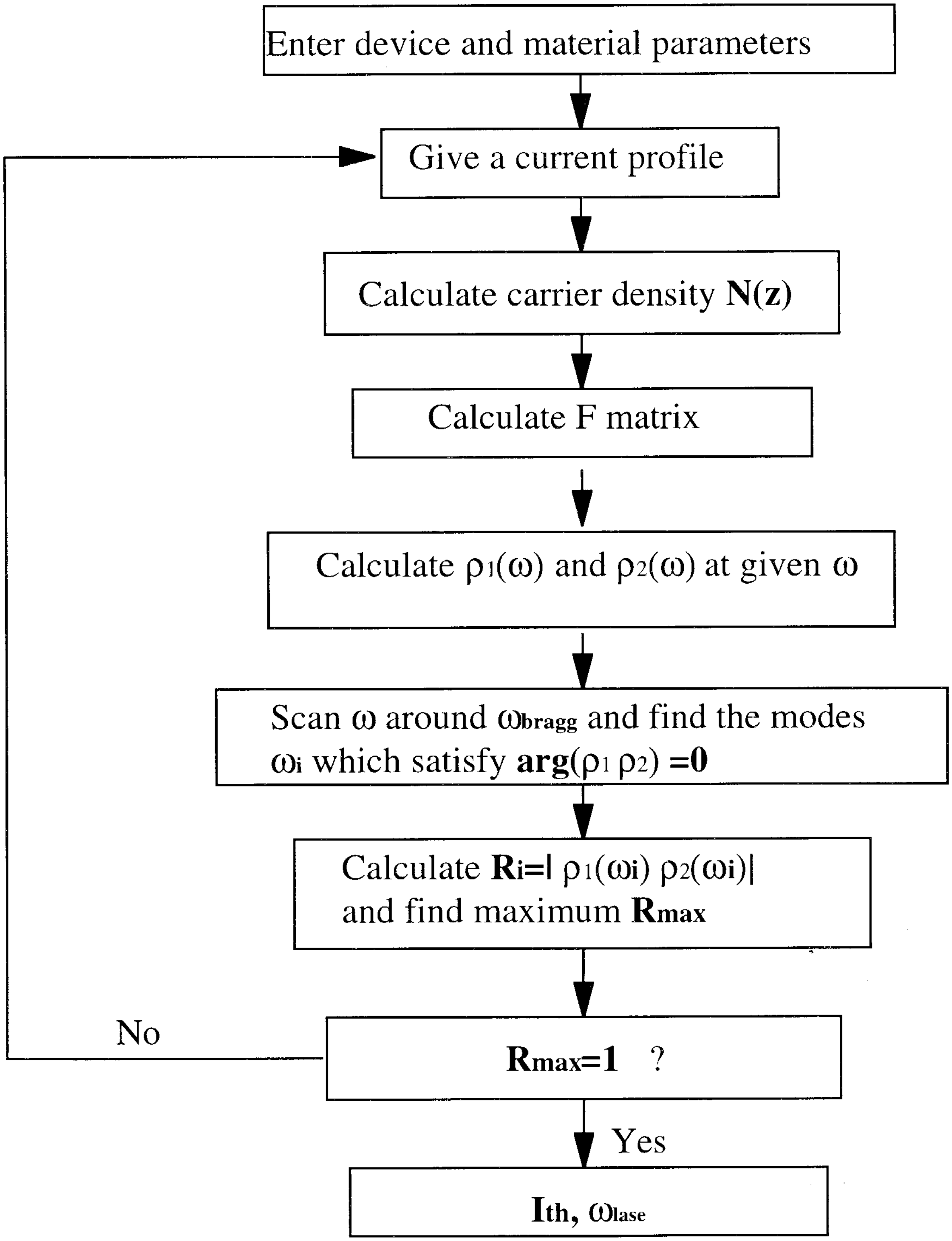

Figure 3.1: Algorithm to solve lasing condition.

3.3 Above-threshold simulation

Above threshold the electron density is determined by the current injection, spontaneous emission and stimulated emission as expressed in (2.46). The stimulated emission depends on the photon density. The photon density and electric fields depend on the electron distribution through the effective index and modal gain. The field distribution will therefore depend on the photon density and has to be solved self-consistently. The algorithm for above threshold problems is shown in Fig. 3.2. The injection current is chosen as the independent variable and remains fixed to determine the output optical power and photon density distribution. With keeping the current profile fixed, the photon density and electric field distribution are calculated self-consistently to satisfy the lasing condition (2.47). If the calculated photon distribution differs from the assumed photon distribution, a new guess for the photon distribution is made. This new distribution can be either the newly calculated photon distribution or the average of the calculated and the previously assumed photon distribution. Only when the calculated photon distribution differs from the assumed one by less than a predetermined error is the photon distribution found. The rate equation (2.46) is used to find the electron density. During this iteration, only one mode is considered, and a final check has to be performed on other longitudinal modes once the photon distribution converges. If a longitudinal mode is found with a round-trip gain larger than 1, the iteration starts over on this new mode. If the new mode turns out to be the maximum round-trip gain mode, it is assumed that a mode switch has occurred.

Algorithm for Self-Consistency above Threshold

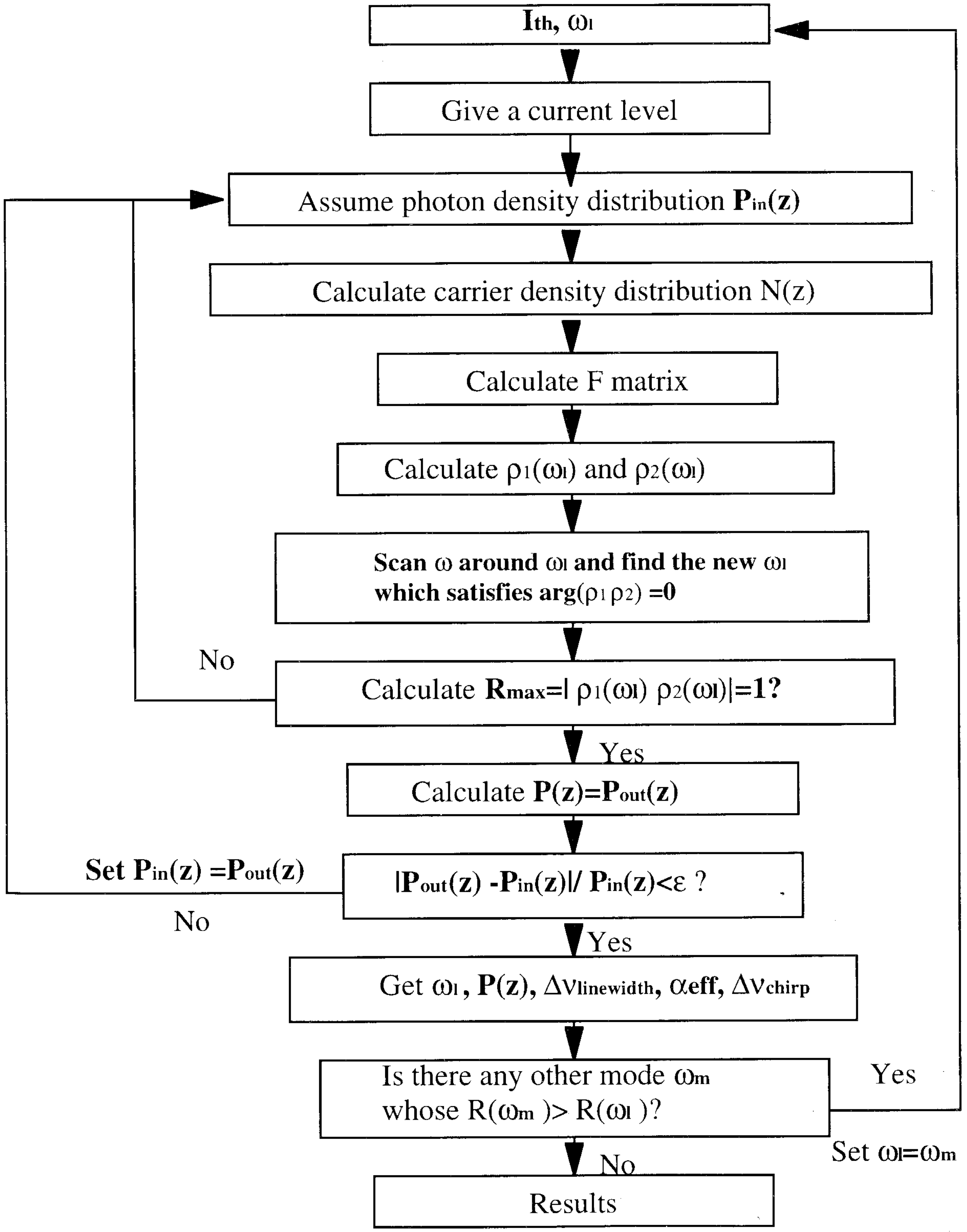

Figure 3.2: Algorithm for self-consistency above threshold.

A quarter wave shifted DFB laser has been calculated above threshold. The photon density, electron density and effective index distribution are shown in Fig. 3.3. The laser is 300μm long and with coupling constant $\kappa L=1$. The phases of facet reflectivities are assumed to be zero, and it can be seen that the spatial hole burning is strong at the center of the laser for the quarter wave shifted DFB laser (Fig. 3.3). Due to the spatial hole burning effect, the carrier density and effective index distributions are affected by nonuniform photon density distribution. Another commonly used DFB structure has asymmetric facet reflectivities. In our example, we use a DFB laser with $R_f=0.1$ and $R_b=0.7$. The DFB lasers with equal reflectivity at both ends generally have two modes lasing. The photon density, electron density and effective index distributions of the asymmetric DFB laser have been calculated and shown in Fig. 3.4. The asymmetric DFB lasers are used to generate one lasing mode by suppressing one of the two potential lasing modes. For high temperature operation of single longitudinal mode (SLM) DFB lasers, the asymmetrical structure has been frequently used to suppress the Fabry-Perot modes in the lasers. The front facet is usually anti-reflection (AR) coated with $R_f<5\%$ and the back facet high-reflection (HR) coated with $R_f\sim70\%$. In Fig. 3.5, we show the calculated photon distributions of three λ/4-shifted DFB lasers with different coupling constants. The coupling constant of a DFB laser has a strong effect on the spatial hole burning. The DFB laser with larger coupling constant has bigger nonuniformities in its photon and electron distributions. For $\lambda/4$-shifted DFB laser with high κL values, it loses its SLM operation when the output power reaches a certain power level. So, low coupling ($\kappa L \sim 1$) DFB lasers are good candidates for high power SLM operations.

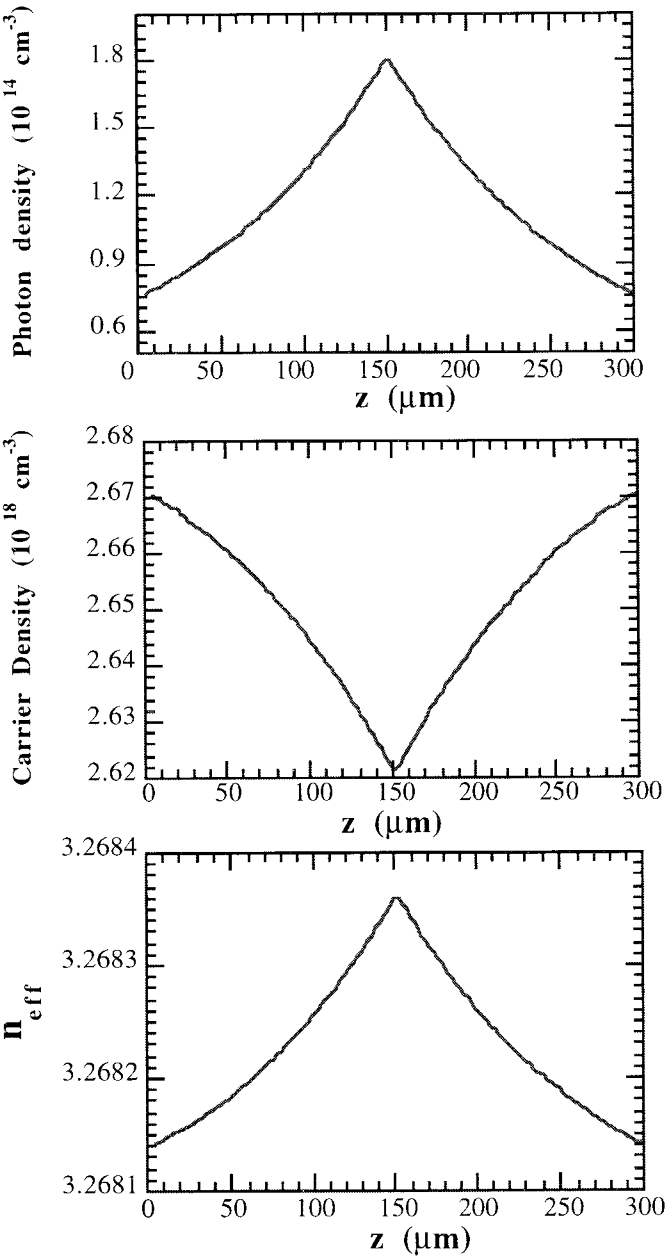

Figure 3.3: The photon density, electron density and effective index distributions in a quarter wave shifted DFB laser above threshold. (R_f=R_b=0.3)

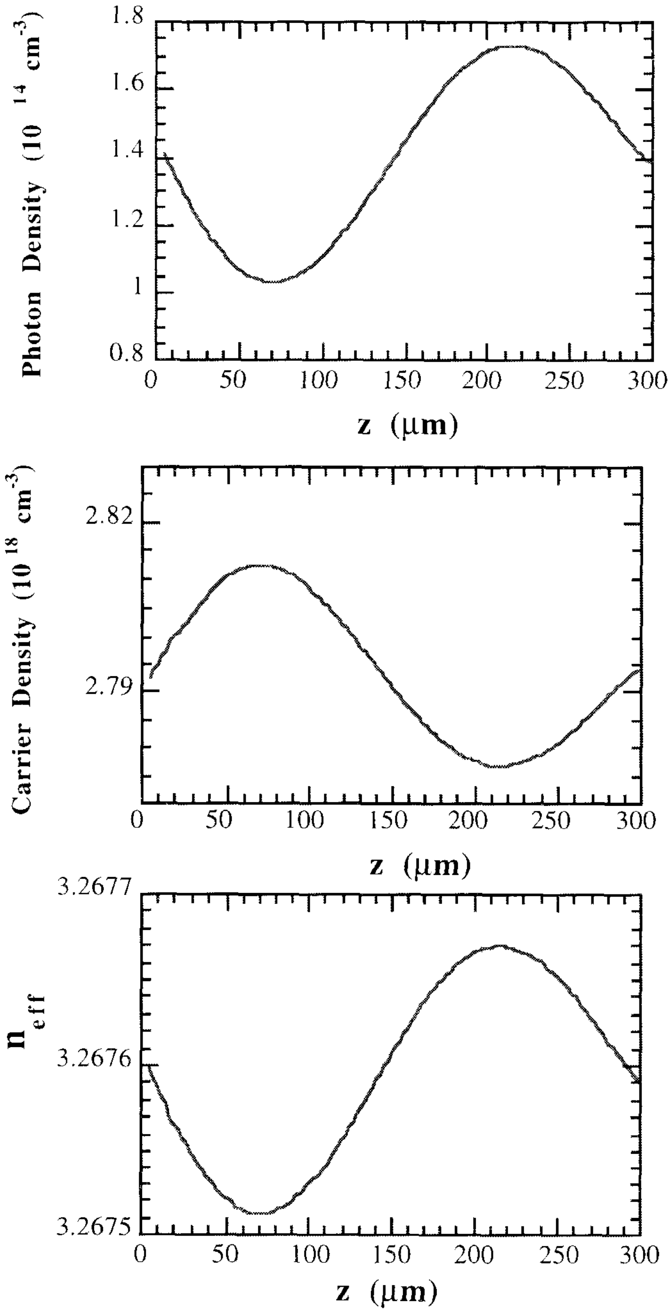

Figure 3.4: The photon density, electron density and effective index distributions in a DFB laser above threshold. (R_f=0.1, R_b=0.7)

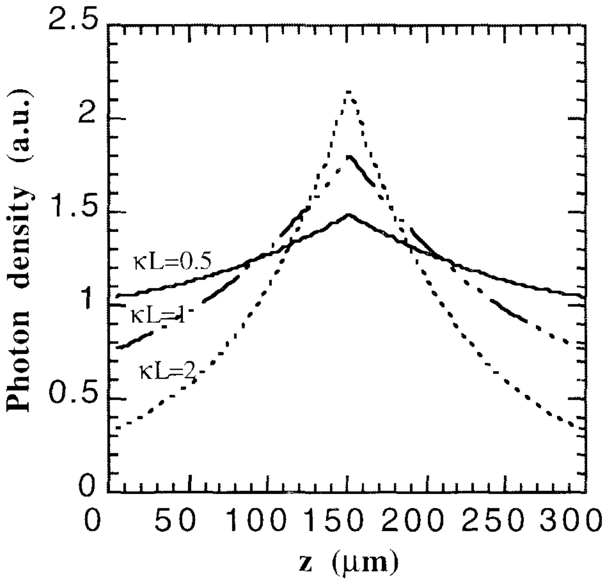

Figure 3.5: The photon density distributions in quarter wave shifted DFB lasers with different coupling coefficients above threshold. (R_f=R_b=0.3)

3.4 Large signal modeling

For single-mode DFB laser, the transverse electric field can be represented by [1,14]

$$F(z,t) = E^+(z,t)\, exp[-i\beta_0 z+i(\omega_0+\Delta\omega)t] + E^-(z,t)\, exp[+i\beta_0 z+i(\omega_0+\Delta\omega)t] \tag{3.1}$$

where E^+, E^- are the complex field amplitudes of the forward- and backward-waves, respectively, and ω_0 is the reference frequency. $\beta_0 = 2\pi/\Lambda_0$, where Λ_0 is the Bragg wavelength. $\Delta\omega=\omega - \omega_0$, ω is the lasing frequency. For a DFB laser under large signal modulation, the amplitudes E^+, E^- are described by the following coupled traveling rate equations [1]:

$$\frac{1}{v_g}\frac{\partial E^+(z,t)}{\partial t} + \frac{\partial E^+(z,t)}{\partial z} = i\kappa E^-(z,t) - (i\delta + i\Delta\omega/v_g - g+\alpha_{loss})E^+(z,t) + T^+ \tag{3.2}$$

$$\frac{1}{v_g}\frac{\partial E^-(z,t)}{\partial t} - \frac{\partial E^-(z,t)}{\partial z} = i\kappa E^+(z,t) - (i\delta + i\Delta\omega/v_g - g+\alpha_{loss})E^-(z,t) + T^- \tag{3.3}$$

The variation in amplitudes is accounted by assuming that in any local sections the forward and backward fields grow or decay at the same rate. Hence, in each segment of the laser,

$$\mu(z,t) = \frac{1}{v_g}\frac{\partial E^-(z,t)}{E^-(z,t)\,\partial t} = \frac{1}{v_g}\frac{\partial E^+(z,t)}{E^+(z,t)\,\partial t} \tag{3.4}$$

where μ is real and assumed to be uniform over any segment but varies from segment to segment. By introducing a new dynamic gain distribution

$$G(z,t)=g(z,t)-\mu(z,t) \quad , \tag{3.5}$$

we can give new quasi-steady coupled-mode equations

$$\frac{\partial E^{+}(z,t)}{\partial z} = i\kappa E^{-}(z,t) - (i\delta + i\Delta\omega/v_g - G + \alpha_{loss})E^{+}(z,t) + T^{+} \tag{3.6}$$

$$-\frac{\partial E^{-}(z,t)}{\partial z} = i\kappa E^{+}(z,t) - (i\delta + i\Delta\omega/v_g - G + \alpha_{loss})E^{-}(z,t) + T^{-} \tag{3.7}$$

Photon density $S(z)$ is proportional to $|E^{+}(z)|^2+|E^{-}(z)|^2$ so that one can also write

$$\mu(z,t) = \frac{1}{2v_g S(z,t)} \frac{\partial S(z,t)}{\partial t} \tag{3.8}$$

Given that μ is known, then the coupling-mode equations (3.6) and (3.7) can be solved as in the above threshold simulation. The operations in the large mode modeling are outlined as the following:

1) Switching at a given injection current above threshold, we start to solve the photon $S(z,t=0)$ and field $E^{\pm}(z,t=0)$, carrier density $S(z,t=0)$ distributions above threshold as we described in Section 2.3. The $\mu=0$ at $t=0$.

2) Calculating the parameters: $G(z,t=0)$ from (2.31), refractive index $n_{eff}(z,t=0)$ from (2.35).

3) Finding the lasing mode ω_0 at $t=0$.

4) At $t>0$, we solve field and photon distributions from (2.54), (2.44). We get μ by

$$\mu(z,t) = \frac{1}{2v_g} \frac{S(z,t)-S(z,t-\Delta t)}{\Delta t\ [(S(z,t)+S(z,t-\Delta t)]/2} \tag{3.9}$$

Here $S(z,t)$ is the calculated photon density at present and $S(z,t-\Delta t)$ is the photon density at previous time $t-\Delta t$. We take this predicted value back to step 2) and repeat this process until the errors between the two iterations are less than a preselected limit.

5) For $t+\Delta t>0$, we get $N(t+\Delta t)$ from calculating dN/dt for the carrier density rate equation (2.44) at t

$$N(t+\Delta t) = N(t) + \frac{dN}{dt}\bigg|_t \tag{3.10}$$

then go back to step 2) until the desired time length is reached.

The model here is used to analyze λ/4 phase-shifted DFB laser with AR coating at both facets, e.g., $R_f=R_b=0.05$. At conditions of large signal modulation, the laser is initially biased just above the threshold and modulated with a pulse function. The injection current as a function of time is shown in Fig. 3.6. The dynamic response of the DFB laser can be obtained from the model (Fig. 3.6). The transient response shows damped oscillations as expected. Fig. 3.6 also shows the dynamic response of a laser with larger nonlinear gain coefficient $\varepsilon=10^{-16}\mathrm{cm}^3$, of which the oscillations are significantly reduced to almost a single pulse. The frequency chirp of the DFB laser is shown in Fig. 3.7a with $\varepsilon=10^{-17}\mathrm{cm}^3$ and $\varepsilon=10^{-16}\mathrm{cm}^3$. The frequency change is caused by variations of the refractive index that is related to the change of the carrier density as given (2.34). Due to the strong SHB in λ/4 phase-shifted DFB lasers, the nonuniformity of the refractive index is serious, which contributes extra chirp in addition to the chirp caused by uniform change of the refractive index. We write the frequency chirp Δν (in Fig. 3.7) as $\Delta\lambda=-\Delta\nu\,\lambda^2/c$. As we will show in Chapter 5, a simple formula based on conventional rate equation can be used to describe the frequency chirp and it is given as

$$\Delta \nu(t) \approx \frac{\alpha}{4\pi}\left(\frac{\partial \ln S(t)}{\partial t} + \frac{\varepsilon S(t)}{\tau_{ph}}\right) \tag{3.11}$$

The first term represents the transient chirp, which is proportional to changing rate of output power. The second term represents the adiabatic chirp, which is proportional to the power level and nonlinear gain coefficient. From Fig. 3.7, it is obvious to see that the transient chirp is a result of the modulated optical power. For large ε, the adiabatic chirp becomes important. In Fig. 3.7a, the laser with larger ε has larger chirp, which comes mostly from adiabatic chirp. From (3.11), linewidth enhancement factor is found to be a determining factor for the chirp. In Fig. 3.7b, we calculated the chirp of DFB lasers with α=2.5 and 5, respectively. The laser with α= 5 has larger chirp as predicted in (3.11). For multisection DFB lasers, (3.11) is not valid to describe the chirp and an expression for frequency chirp, which is based on rate equations with considering SHB, has to be used. We will derive the expression in Chapters 4 and 5.

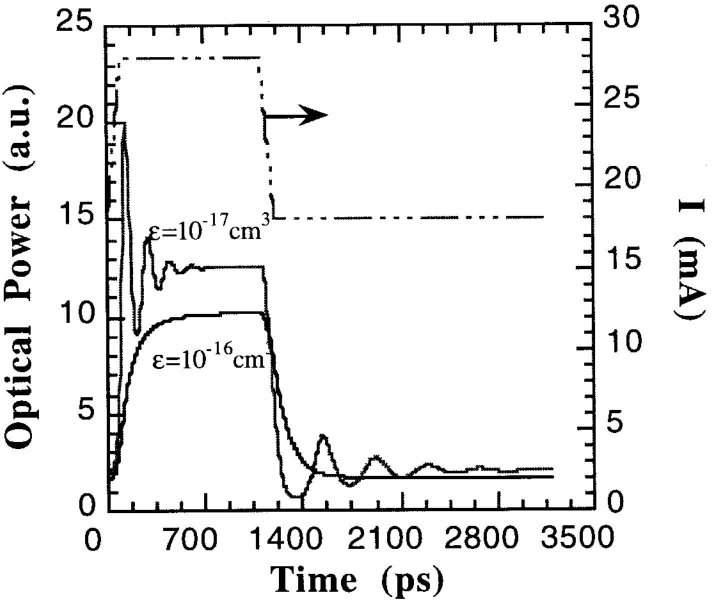

Figure 3.6: Optical response of λ/4 phase-shifted DFB laser with pulse current injection. The nonlinear gain suppression coefficient is chosen to be $\varepsilon=10^{-17}\text{cm}^3$, and 10^{-16}cm^3.

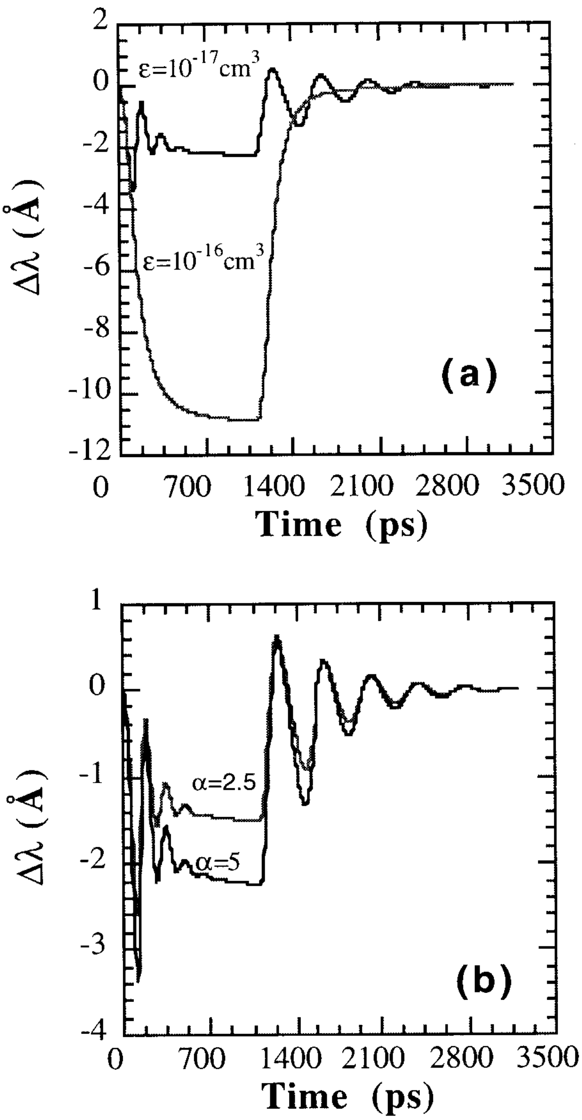

Figure 3.7: Frequency chirp of λ/4 phase-shifted DFB laser modulated with pulse function for: (a) $\varepsilon=10^{-17}cm^3$, and $10^{-16}cm^3$, (b) α=2.5, and 5.

Reference

[1] P. Vankwikelberge, G. Morthier, and R. Baets, *IEEE J. Quantum Electron.*, **QE-26**, 1728 (1990)

[2] J.E.A. Whiteaway, G.H. Thompson, A.J. Collar, and C. J. Armistead, *IEEE J. Quantum Electron.*, **QE-25**, 1261 (1989)

[3] K.O. Hill, and A. Wantanbe, Appl. Opt. 14, 950 (1975)

[4] H. Soda, Y. Kotaki, H. Sudo, H. Ishikawa, S. Yamakoshi, and H. Imai, *IEEE J. Quantum Electron.*, **QE-23**, 804 (1987)

[5] Y. Nakano, T. Okmatani, and T. Tada, *11th IEEE International Semiconductor Laser Conf.* H2 (1982)

[6] G.P. Agrawal, and A.H. Bobeck, *IEEE J. Quantum Electron.*, **QE-24**, 2407 (1988)

[7] M. Okai, S. Tsuji, and N. Chinone, *IEEE J. Quantum Electron.*, **QE-25**, 1314 (1989)

[8] M. Usami, and S. Akiba, *IEEE J. Quantum Electron.*, **QE-25**, 1245 (1989)

[9] K. Kkuchi, and H. Tomofuji, *IEEE J. Quantum Electron.*, **QE-26**, 1717 (1990)

[10] M.G. Davis, and R.F. O'Dowd, *IEEE Phot. Tech. Lett.* **3**, 603 (1991)

[11] I. Orfanos, T. Sphicopoulos, A. Tsigopoulos, and C. Caroubalos, *IEEE J. Quantum Electron.*, **QE-27**, 946 (1991)

[12] T. Yamanaka, S. Seki, and K. Yokoyama, *IEEE Phot. Tech. Lett.* **3**, 610 (1991)

[13] M. Yamada, and K. Sakuda, *Appl. Opt.* 26, 3474 (1987)

[14] L.M. Zhang and J.E. Carroll, *IEEE J. Quantum Electron.*, **QE-28**, 604 (1992)

Chapter 4

Small Signal and Spectral Characteristics of Distributed Feedback Lasers

4.1 Introduction

Small signal analysis in Fabry-Perot lasers is based on the conventional rate equations [1-2]. In the lasers, the photon and carrier densities are assumed to be uniform. The assumption holds well as long as the facet reflectivities are greater than 0.2 [3]. However, In DFB lasers, the longitudinal spatial hole burning (LSHB) has been found to be an influence factor on linewidth, frequency chirp, and high speed performance. A Green's function method has been used to solve the coupled-mode equations in DFB lasers when the LSHB is also considered.

Pure AM modulation or FM modulation of single section semiconductor lasers is very difficult due to the link of the phase of the lasing mode to the intensity by the α factor. It is found that two-section DFB lasers can be used to achieved chirpless AM[4] modulation and very high efficiency FM modulation [5].

The early theory [6-7] for two section semiconductor lasers was based on the rate equations for a closed resonator [8], in which the carrier density and the optical photon density distributions are assumed to be uniform in each section. Kuneztsov [9] then introduced the effective length in DFB lasers to calculate the wavelength tuning and frequency chirp in two-section DFB lasers. In his theory, the optical power distribution is assumed to be uniform in the lasers. Tromborg [10] proposed the Green's function method to solve the electrical field distribution in DFB lasers with considering the LSHB and derived the rate equations for optical power and instantaneous lasing frequency.

4.2 Solving the coupled-mode equations by Green's Function

4.2.1 Green's function for coupled-mode equations

In single-mode DFB laser, the transverse electric field can be represented by [11]

$$E(z) = E^{+}(z)\, exp[-i\beta z] + E^{-}(z)\, exp[+i\beta z] \qquad (4.1)$$

The coupled mode equations (2.14) and (2.15) can be written in vectorial form as [12]

$$\frac{d\mathbf{Z}}{dz} = \mathbf{M}(z)\ \mathbf{Z}(z) + \mathbf{P}(z) \tag{4.2}$$

with

$$\mathbf{Z}(z) = \begin{bmatrix} E^{+}(z) \\ E^{-}(z) \end{bmatrix} \tag{4.3}$$

$$\mathbf{P}(z) = \begin{bmatrix} f^{+} \\ f^{-} \end{bmatrix} \tag{4.4}$$

$\boldsymbol{P}$ is the noise source due to spontaneous emission. $\boldsymbol{Z}_R(z)$ and $\boldsymbol{Z}_L(z)$ are assumed to be two solutions of the coupled mode equations for $\boldsymbol{P}=0$ and are satisfying the boundary conditions on the left ($\mathbf{Z}_L(z)$) or on the right ($\mathbf{Z}_R(z)$). Green's function is defined as the solution to

$$\frac{d\mathbf{G}}{dz} = \mathbf{M}(z)\mathbf{G}(z,z') + \begin{bmatrix} \delta(z-z') \\ -\delta(z-z') \end{bmatrix} \tag{4.5}$$

satisfying all boundary conditions. Solving the equation gives [12]

$$\mathbf{G}(z,z') = \begin{cases} \mathbf{Z}_L(z)\mathbf{Z}_R^{\mathbf{T}}(z') & z<z' \\ \mathbf{Z}_R(z)\mathbf{Z}_L^{\mathbf{T}}(z') & z>z' \end{cases} \tag{4.6}$$

The Green's function solution to (4.2) is given by

$$\mathbf{Z}(z) = \frac{-2i\beta}{W}\int_0^1 \mathbf{G}(z,z')\mathbf{P}(z')dz' \tag{4.7}$$

with the Wronskian W which is defined as

$$W = Z_L(z)\frac{d}{dz}Z_R(z) - Z_R(z)\frac{d}{dz}Z_L(z)$$

$$= -2i\beta[E_R^{+}(z)E_L^{-}(z) - E_R^{-}(z)E_L^{+}(z)\ ] \tag{4.8}$$

It can be shown that W is z independent from (4.7)

$$\frac{dW}{dz} = (M_{11}+M_{22})W \equiv 0 \tag{4.9}$$

We can define frequency domain electrical field $E(\omega, z)$ by

$$E(\omega,z) = \int_{-\infty}^{\infty} E(z,t)\ e^{i\omega t}dt \tag{4.10}$$

The field $E(z, t)$ is given as

$$E(z,t) = E^{+}(z,t)\ exp[-i\beta z+i(\omega_0+\Delta\omega)t] + E^{-}(z,t)\ exp[+i\beta z+i(\omega_0+\Delta\omega)t] \tag{4.11}$$

The solution to (4.1) is given by

$$W[\beta(z)]E(\omega,z) = \int_{0}^{l} G(z,z')f_{\omega}(z')dz' \tag{4.12}$$

Here Green's function is rewritten from (4.6) as

$$G(z,z') = Z_L(z)\ Z_R(z')\ \theta(z-z') - Z_R(z)\ Z_L(z')\ \theta(z'-z) \tag{4.13}$$

$\Theta(z)$ is the Heaviside step function and W is given by (4.8). f_{ω} is noise source in frequency domain.

From (4.12) and in the limit of a vanishing force ($f_{\omega}=0$), there can only be a nonzero solution, when $W=0$. For the stationary case with dc current injection, the lasing modes are the states for which

$$W[\beta(z)] = 0 \tag{4.14}$$

is fulfilled with the rate equation for the carrier density (2.46). The equation (4.14) is equivalent to the lasing condition (2.47). From (4.8), Z_R is proportional to Z_L, and from (4.12), $E(\omega,z)$ is proportional to Z_L or Z_R.

4.2.2 Green's function solution for electric field

Following Henry [13], we define a mode amplitude A_ω by

$$E(\omega,z) = A_\omega Z_L\,(z) \tag{4.15}$$

and the corresponding envelope function $A(t)$ by

$$A\,(t) = \int_0^\infty A_\omega e^{i(\omega-\omega_0)t} d\omega \tag{4.16}$$

When the driving force F≠0 or with modulation, the Wronskian is not exactly zero, and $\beta(z)$ fluctuates around its stationary value. In order to derive a rate equation for the envelope function $A(t)$, we expand the Wronskian $W[\beta(z)]$ around the stationary solution $\beta_0(z)$. The $\beta(z)$ depends on frequency ω, carrier density, and photon density. Hence,

$$\Delta\beta(z) = \beta(z) - \beta_0(z) = \frac{\partial\beta}{\partial\omega}(\omega-\omega_0) + \frac{\partial\beta}{\partial N}\Delta N + \frac{\partial\beta}{\partial N}\Delta S \tag{4.17}$$

where $\Delta N = N - N_0$, $\Delta S = S - S_0$.

The first-order expansion of the Wronskian can be written as

$$W[\beta(z)]=W[\beta_0(z)]+\int_0^l \frac{\partial W}{\partial \beta(z')}\Delta\beta(z')dz' \tag{4.18}$$

By (4.12) and (4.15), the mode amplitude satisfies

$$W[\beta(z)]A_\omega = \int_0^l Z_R(z')f_\omega(z')dz' \tag{4.19}$$

With (4.19) and making an inverse Fourier transform, we get the rate equation for $A(t)$

$$\frac{d}{dt}A(t) = A(t)\ [\int_0^l C_N(z)\Delta N(z,t)\ dz\ +\ \int_0^l C_S(z)\Delta S(z,t)\ dz\ ] + F_A(t) \tag{4.20}$$

The rate equations for the optical power and the phase of the optical field can be derived from (4.20) if we write

$$A(t) = \sqrt{P(t)}\ e^{i\phi(t)t} \tag{4.21}$$

and the rate equations are [10, 12]

$$\frac{d}{dt}P(t) = 2P(t)\ [\int_0^l Re\{C_N(z)\}\Delta N(z,t)\ dz + \int_0^l Re\{C_S(z)\}\Delta S(z,t)\ dz\ ] + R\ + F_P(t) \tag{4.22}$$

$$\frac{d}{dt}\phi(t) = [\int_0^l Im\{C_N(z)\}\Delta N(z,t)\ dz + \int_0^l Im\{C_S(z)\}\Delta S(z,t)\ dz\ ]\ + F_\phi(t) \tag{4.23}$$

Here the weight functions $C_N(z)$ and $C_S(z)$ are defined by

$$C_X\ = -j\ E^+(z)\ E^-(z)\frac{\partial\beta}{\partial X}(z)\ /\{\int_0^l E^+(z')\ E^-(z')\frac{\partial\beta}{\partial\omega}(z')\ dz'\} \qquad (X=N,\ S) \tag{4.24}$$

The noise source is given by

$$F_A(t) = \frac{i}{2\pi\frac{\partial W}{\partial \omega}} \int_0^l Z_L(z)[\int_0^\infty f_\omega(z)\ e^{i(\omega-\omega_0)t} d\omega]\ dz \tag{4.25}$$

4.2.3 Small signal rate equations

For small signal modulation at frequency $f_m = \omega_m/2\pi$, the dynamic variables current density $J(z,t)$, carrier density $N(z,t)$, and photon density $S(z,t)$ can be written as the sum of their stationary distributions and the variations due to RF modulation

$$J(z,t) = J_0(z) + J_1 e^{i\omega_m t} \tag{4.26a}$$

$$S(z,t) = S_0(z) + S_0(z)\,\delta S(\omega_m) e^{i\omega_m t} \tag{4.26b}$$

$$P(t) = P_0 + P_0 \delta S(\omega_m) e^{i\omega_m t} \tag{4.26c}$$

$$N(z,t) = N_0(z) + N_1(z) e^{i\omega_m t} \tag{4.26d}$$

Here $J_0(z)$, $N_0(z)$, and $S_0(z)$ are the stationary distributions in DFB lasers.

The small signal rate equations can be gotten from (2.44) and (4.22)

$$\frac{d}{dt}[\delta S(\omega_m) e^{i\omega_m t}] = -\Gamma_s\ \delta S(\omega_m) e^{i\omega_m t} + [\int_0^l Re\{C_N(z)\}\,\delta N(z,t)\ dz\ + F_P(t)/P_0 \tag{4.27}$$

$$\frac{d\delta N(z,t)}{dt} = \frac{\delta J(z,t)}{ed} - \Gamma_N(z)\ \delta N(z,t)\ - \frac{a\,[N_0(z)-N_{tr}]}{[\ 1+\varepsilon S_0(z)\ ]} v_g \delta S(z,t) \tag{4.28}$$

where

$$\Gamma_S(z) = R / S_0(z) - \int_0^l Re\{C_S(z)\} S_0(z)\, dz \tag{4.29}$$

$$\Gamma_N(z) = \frac{1}{\tau_s(z)} + v_g \frac{\Gamma_C\ dG/dN\ S_0(z)}{1+\varepsilon S_0(z)} \tag{4.30}$$

Here τ_s (z) is defined as

$$\frac{1}{\tau_s(z)} = \frac{1}{\tau} - 2BN(z) - 3CN(z)^2 \tag{4.31}$$

and R is the spontaneous emission rate.

4.3 Amplitude modulation

4.3.1 Expression for AM modulation in DFB lasers

The frequency response of DFB lasers can be obtained from (4.26), (4.27), and (4.28)

$$\delta S(\omega_m) = \frac{\int_0^l dz\ C_N(z)\ J_1/[e(i\omega_m + \Gamma_N(z)]}{D(\omega_m)}\ , \tag{4.32}$$

where

$$D(\omega_m) = \int_0^l \frac{(\omega_R(z)+\omega_m - i\Gamma_R(z))(\omega_R(z)-\omega_m+i\Gamma_R(z))}{i\omega_m + \Gamma_N(z)} dz, \tag{4.33}$$

and the local resonance frequency $\omega_R(z)$, and the damping rate $\Gamma_R(z)$ are

$$\omega_R^2(z) = 2l\ C_N(z) v_g g(z) S_0(z) - [\Gamma_N - \Gamma_S]^2/4, \tag{4.34}$$

and

$$\Gamma_R(z) = [\Gamma_N(z) + \Gamma_S(z)]/2, \tag{4.35}$$

where $g(z)$ is the local optical gain, and Γ_c is the optical confinement factor for the lasing mode. The resonance response of DFB lasers occurs when $D(\omega_m)$ is minimized. To find the resonance frequency ω_R and the damping rate Γ_R of DFB lasers, the numerical calculation of (4.32) (with (4.34) and (4.35)) has to be carried out. Because $\omega_R(z)$ and $\Gamma_R(z)$ are functions of photon density, $S_0(z)$, and electric fields E^+, E^-, ω_R and Γ_R of DFB lasers depend on the photon density distributions.

4.3.2 Resonance frequency in single section DFB lasers

In the low output power limit, the damping rate is much smaller than the resonance frequency and the small signal response (4.32) can be simplified as [14]

$$\left(\frac{\delta S(\omega_m)}{\delta S(0)}\right)^2 \approx \frac{\overline{\omega}_R^4}{(\overline{\omega}_R^2-\omega_m^2)^2+4\overline{\Gamma}_R^2\omega_m^2} \tag{4.36}$$

and

$$\overline{\omega}_R^2 \approx \int_0^l 2\, C_N(z) v_g g(z) S_0(z)\, dz \tag{4.37}$$

In single section DFB lasers, the photon density distributions do not change dramatically as long as optical output powers are not very large. The resonance frequency can be approximated as

$$\overline{\omega}_R^2 \approx \eta\, a v_g^2 \overline{g}\, \overline{S_0} \tag{4.38}$$

and we define η as

$$\eta = \frac{2}{av_g} \frac{\int_0^l C_N(z)g(z)S_0(z)dz}{\bar{g}\ \overline{S_0}}. \tag{4.39}$$

Here $\overline{S_0}$ is the average photon density, $\bar{g}$ is the average optical gain, a is the differential gain. $\eta = 1$ for lasers with uniform photon densities. For DFB lasers, $\eta \neq 1$ and has to be numerically calculated. η has been calculated for several typical DFB lasers and is shown as a function of optical power in Fig. 4.1. It can be seen that η depends on optical power. Therefore, the resonance frequencies of DFB lasers are expected to slightly depart from the linear function of $\sqrt{S_0}$ at low optical power.

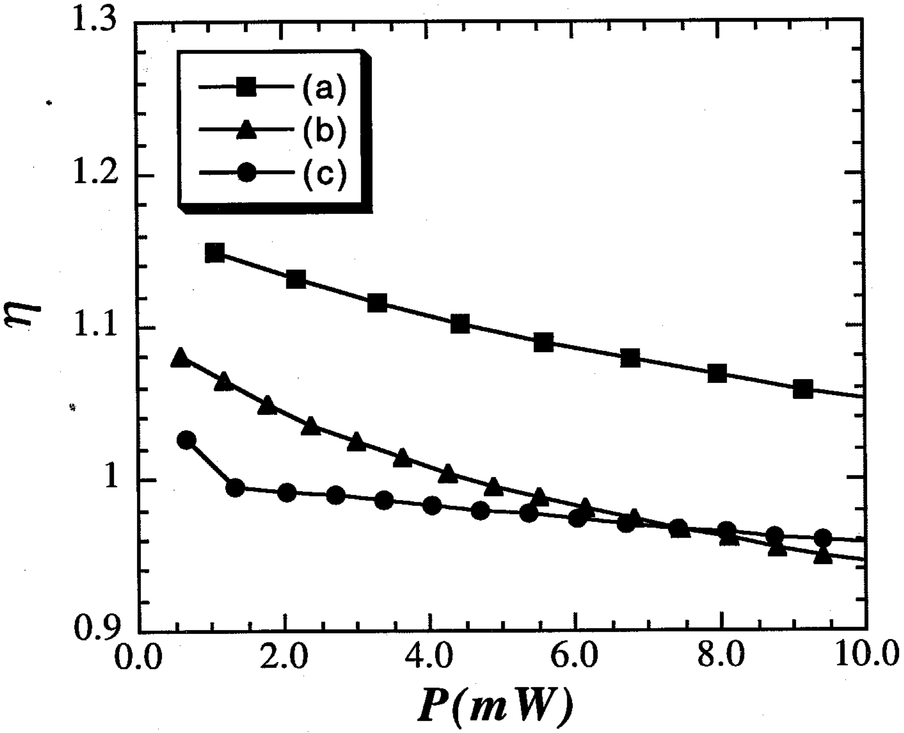

Figure 4.1: The calculated η parameter for DFB lasers:

(a) AR/HR coated DFB laser with $\kappa L=2$, $R_f=0.05$, $R_b=0.95$

(b) As-cleaved DFB laser with $\kappa L=2$, $R_f=0.33$, $R_b=0.33$

(c) 1/4 λ shifted DFB laser with $\kappa L=2$, $R_f=0.33$, $R_b=0.33$

4.3.3 High speed response in a two-section DFB laser

A two-electrode 1.3 μm InGaAsP/InP DFB laser is fabricated for our experiment to study the effects of nonuniform photon distribution on the high speed response of DFB lasers. The laser has two sections, 400μm and 100μm long, with an electric isolation of 1.4 kΩ. The front facet is AR coated and the rear facet is left as-cleaved. The DFB laser oscillates at a single wavelength of λ=1.32μm with at least 35 dB of side-mode-suppression-ratio (SMSR) under CW operation, and it has the coupling coefficient $\kappa L=3$. The two sections are pumped with DC current, with the longer one also AC modulated. The $\delta J(z,t)$ can be written as

$$\delta J(z,t)=\{ \begin{array}{ll} J_1 e^{i\omega_m t} & for\ 0<z<L_1 \\ 0 & for\ L_1<z<L_1+L_2 \end{array} \tag{4.40}$$

The expression of the frequency response of the two-section DFB laser can be written as

$$\delta S(\omega_m) = \frac{\int_0^{L_1} dz\, C_N(z)\, J_1/[e(i\omega_m+\Gamma_N(z))]}{D(\omega_m)}. \tag{4.41}$$

The only difference between (4.32) and (4.41) is that the integration length in the numerator has been changed. They both represent the same frequency response.

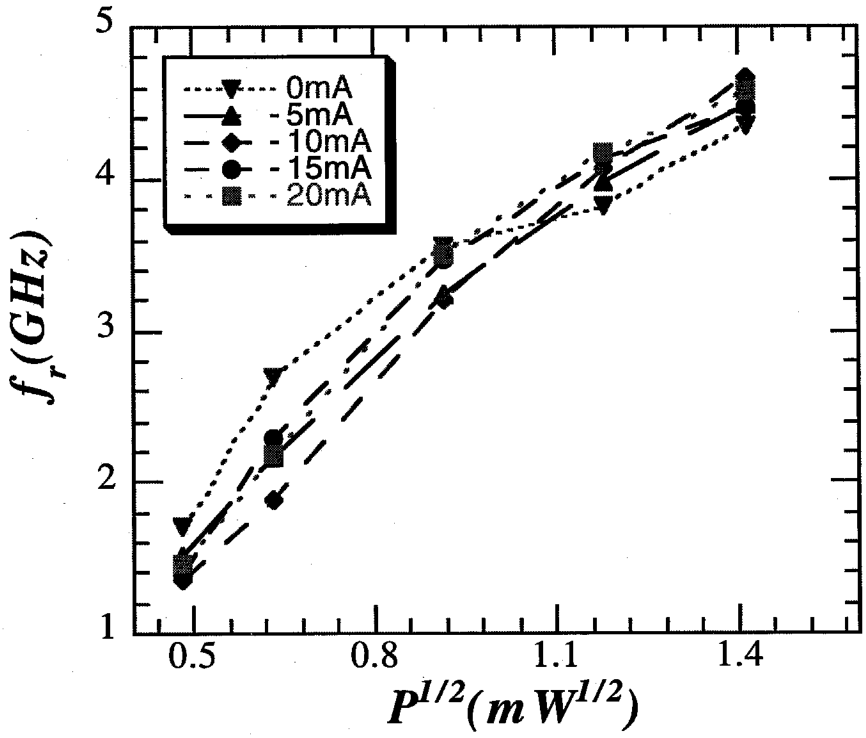

Figure 4.2: The resonance frequency of a two-section DFB laser versus square root of the optical power for various I_2, the injection current into section two.

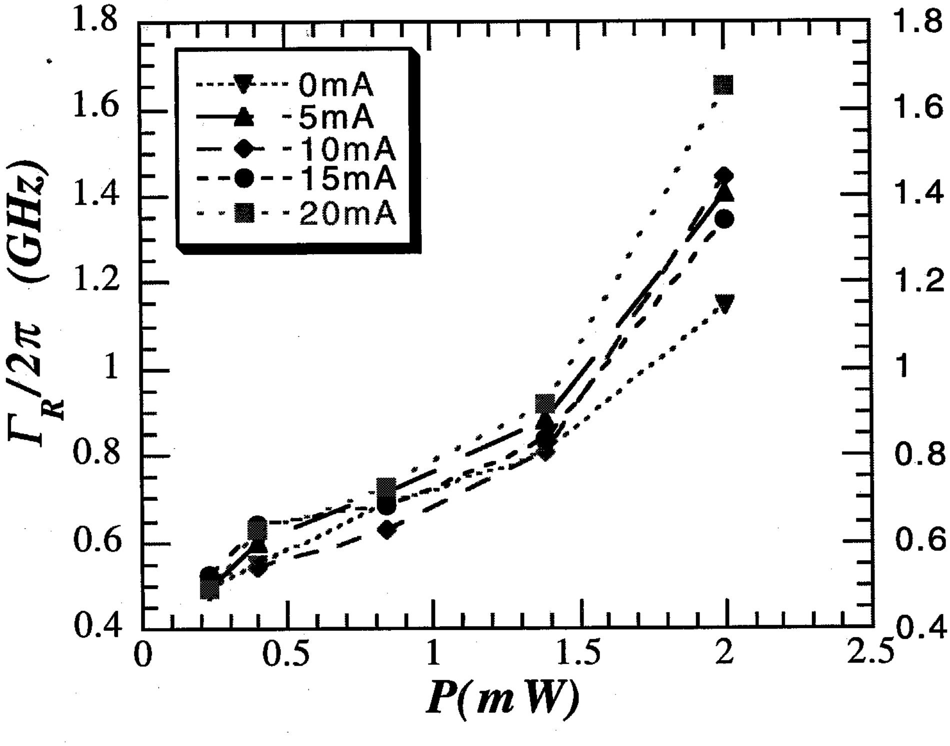

Figure 4.3: The damping rate of the DFB laser versus the optical power for various I_2.

The high frequency modulation of the DFB laser is carried out by a standard experimental arrangement, including an S-parameter test set and a network analyzer. The resonance frequency and damping rate are obtained from the data filling [15] according to (4.38). Fig. 4.2 and Fig. 4.3 show the measured resonance frequency and damping rate as functions of optical power. The measurement is conducted for the output optical power $P = 0.23,\ 0.4,\ 0.84,\ 1.3,$ *and* $2\ mW$ for various injection currents. At each optical power level, the current into section one, I_1, is adjusted to maintain the same output power while I_2 is chosen to be 0 mA, 5 mA, 10 mA, 15 mA and 20 mA. Fig. 4.2 shows the resonance frequencies for different injection currents, which differ as much as 0.7 GHz. The difference between resonance frequencies at several optical power levels is the result of the dependence of the resonance frequencies on the distributions of the photon density and the traveling electric fields in the DFB laser, as given in (4.32)-(4.35). We calculate η in (4.39) to analyze the effect of the nonuniform photon density on the resonance frequencies of the DFB laser. The relatively large value of f_r at low P, when $I_2 = 0\ mA$, is predicted by the calculated η. The photon density is much larger in the long section than in the short section for $I_2 = 0\ mA$, and according to (4.39), we found that $\eta \approx 1.2$. At high P, the spatial hole burning effect is serious in the long section, and $\eta \approx 0.85$ is found. The gradually reducing η explains why, as we increase optical power, the rate of increase of the resonance frequency is slowed at high P when no current is in the short section (Fig. 4.2). For $I_2 = 20\ mA$, the photon density is much larger in the short section than that in the long section, and the calculated $C_N(z)$ shows that it is very small in the short section at low P. From (4.39), we found that $\eta \approx 0.9$. The small $C_N(z)$ contributes the relatively small f_r at low P (Fig. 4.2) for $I_2 = 20\ mA$. At high P, $C_N(z)$ is more uniform along the lasing axis and $\eta \approx 1.1$, which results in a relative large f_r when $I_2 = 20\ mA$ (Fig. 4.2).

The damping rate, Γ_R, is obtained from the frequency response of the two-section DFB laser (Fig. 4.3). Like the resonance frequency f_r, Γ_R is dependent on the photon density distribution in the laser. The variation of Γ_R becomes larger at high optical power. It is believed that at high optical power, the damping rate is dominated by the contribution of gain suppression, the second term in (4.29). The contribution of gain suppression to the damping rate as seen in (4.29), is the integration of photon density $S_0(z)$ with function $C_N(z)$. That results in the larger difference of Γ_R at high optical power shown in Fig. 4.3. In DFB lasers, the damping rate is influenced more strongly by the photon density distribution than is the resonance frequency, since Γ_R increases linearly with $\overline{S_0}$ while f_r increases linearly with $\sqrt{\overline{S_0}}$.

4.4 Linewidth, effective linewidth enhancement factor

The statistical properties of the complex noise functions are given [10,14]

$$<F_A(t)F_A(t')> = R\ \delta(t-t') \tag{4.42}$$

$$<F_P(t)F_P(t')> = 2\ RP_0\ \delta(t-t') \tag{4.43}$$

$$<F_\phi(t)F_\phi(t')> = \frac{R}{2P_0}\ \delta(t-t') \tag{4.44}$$

If the frequency noise (normally ~ GHz) is much broader than the linewidth, the white noise approximation is used [16]

$$\begin{aligned} \Delta\nu &= \frac{1}{2\pi}\int_{-\infty}^{+\infty} <\delta\dot{\phi}(t)\,\delta\dot{\phi}(t+\tau)>\ d\tau \\ &= <|\delta\omega(0)|^2> \end{aligned} \tag{4.45}$$

where

$$\delta\omega(0) = F_\phi(0) - \alpha_{eff}\frac{F_P(0)}{2P_0} + \int_0^l K(z')\ F_N(z',0)\ dz' \tag{4.46}$$

$$K(z) = \tau_R(z)\ [Im\{C_N(z)\} - \alpha_{eff} Re\{C_N(z)\}] \tag{4.47}$$

The noise spectra $F_\phi(0)$, $F_S(0)$, and $F_N(0)$ can be assumed white noise [12] and the linewidth is obtained as

$$\Delta\nu = \Delta\nu_{sp} + \Delta\nu_{NN} + \Delta\nu_{NS} \tag{4.48}$$

The linewidth consists of three parts, the spontaneous emission linewidth $\Delta\nu_{sp}$, the electron noise component $\Delta\nu_{NN}$ and the stimulated emission component $\Delta\nu_{NS}$. They are given by

$$\Delta\nu_{sp}=\frac{R}{4\pi I_0}(1+\alpha_{eff}^2) \tag{4.49}$$

$$\Delta\nu_{NN}=\frac{1}{\pi}\int_0^l K^2(z')\ D_{NN}(z')dz' \tag{4.50}$$

$$\Delta\nu_{NS}=-\frac{2\alpha_{eff}}{\pi}\int_0^l K(z')\ D_{NS}(z')dz' \tag{4.51}$$

Here D_{NN} and D_{NS} are the diffusion parameters and are given in [10].

We introduce the effective linewidth enhancement factor [10]

$$\alpha_{eff}=\frac{Im\left(\int_0^l (C_N(z)\tau_R(z)\frac{\partial R_{st}}{\partial S}(z)\ S_0(z)-C_S(z)S_0(z))\ dz\ \right)}{Re\left(\int_0^l (C_N(z)\tau_R(z)\frac{\partial R_{st}}{\partial S}(z)\ S_0(z)-C_S(z)S_0(z))\ dz\ \right)} \tag{4.52}$$

Here R is the spontaneous emission rate, I_0 the total photon number in the cavity, τ_R, the carrier lifetime, and R_{st}, the local stimulated emission rate. α_{eff} reduces approximately to material α if the photon density distribution is uniform. The spontaneous emission linewidth (4.49) is the modified Schawlow-Townes formula with α_{eff} replacing material α, and it is the dominant part in (4.48). In most of cases, $\Delta\nu_{NN}$ and $\Delta\nu_{NS}$ are much smaller than $\Delta\nu_{sp}$ and we neglect $\Delta\nu_{NN}$ and $\Delta\nu_{NS}$ in our calculation of linewidth. Fig. 4.4 shows a measured linewidth of a single section DFB laser. The measured linewidth has nearly a linear relation with P^{-1} for moderate optical power. This is predicted in the expression (4.49) and conventional linewidth expression. There are several possible mechanisms for the rebroadening of linewidth at high powers, such as pumping noise and stimulated emission noise ($\Delta\nu_{NN}$, and $\Delta\nu_{NS}$), which become dominant once the spontaneous emission noise $\Delta\nu_{sp}$ is small enough at high powers. At low frequency, $\Delta\nu_{NN}$ and $\Delta\nu_{NS}$ can have a *1/f* component, which is dominant [17-20]. The reduced side-mode-suppression-ratio (SMSR) at high powers in DFB lasers is also a candidate for linewidth rebroadening [21].

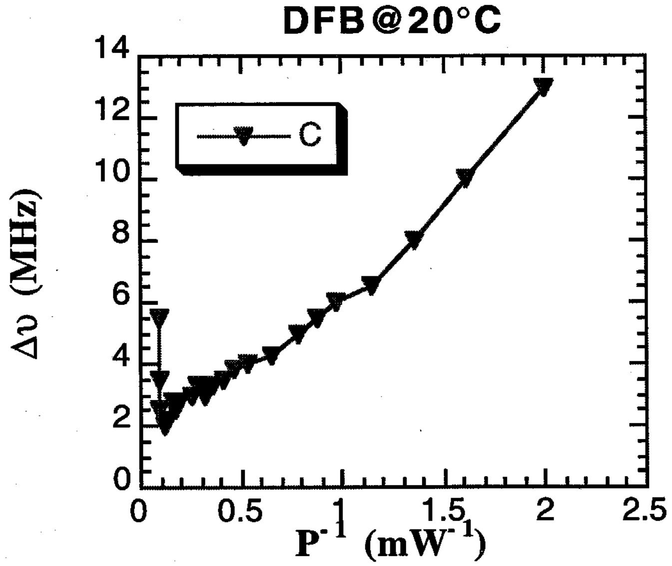

Figure 4.4: A measured linewidth as function of P^{-1} in DFB laser.

A two-electrode 1.55μm InGaAsP/InP DFB laser has been used to measure effects of LSHB on linewidth. The laser has cleaved facets and the two sections are 106μm and 138μm long with an electric isolation 5kΩ between them. The DFB laser lases at a single wavelength of λ=1.55μm with at least 35 dB of SMSR. It has a threshold of 40 mA when uniformly pumped. We get κL=1 from the measured stopband width.

A time delay self-heterodyne detection scheme is used in our measurement of laser linewidth. The laser is isolated with a 70 dB isolator. The laser beam is modulated with an acoustooptic (A-O) modulator at 85MHz. The fundamental beam from the A-O modulator is focused into two kilometers of single mode optical fiber. It is joined by the first order beam at a fiber coupler. One output of the coupler is received by an Ortel 2610 detector. The output of the detector is amplified and then sent to a spectrum analyzer where the linewidth is measured. The other output of the coupler is sent to a power monitor for line adjustment..

The linewidth at different current injection has been measured. Linewidth at various current ratios is shown in Fig. 4.5 for total current I_t of 50mA, 60mA and 70mA. It can be seen that there are certain current ratios at which the linewidth is very small. For I_t*=50mA, 60mA*, two minima are smaller than the linewidth of uniform injection ($I_1/I_2=0.77$). The minima will shift if the total current increases. The linewidth is found to be very large for either small or big current ratios ($I_1/I_2<0.2$ *or* $I_1/I_2>2.5$).

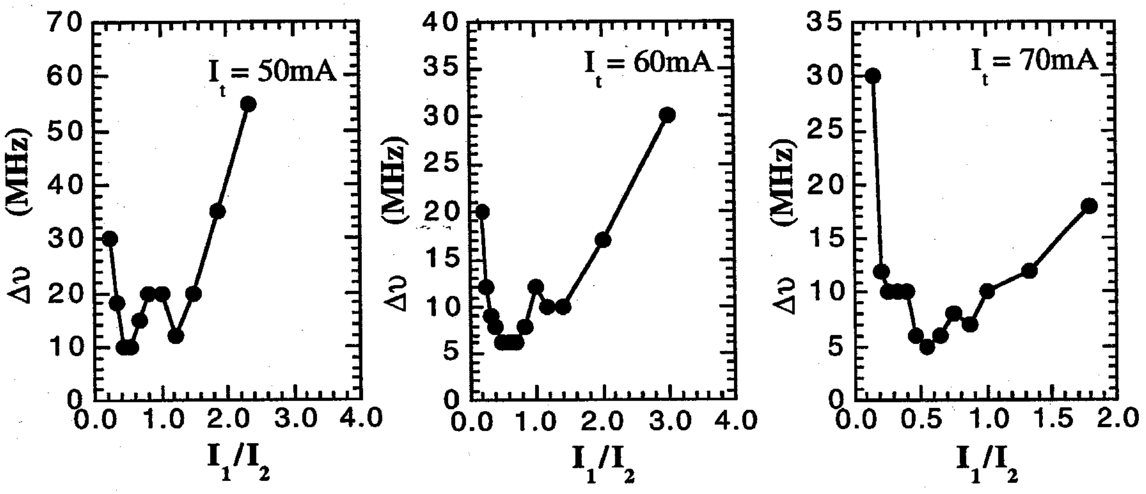

Figure 4.5: The measured linewidth of two-section DFB laser at different current ratio. The total injection current is

(a) $I_t = 50\,mA$ (b) $I_t = 60\,mA$ (c) $I_t = 70\,mA$.

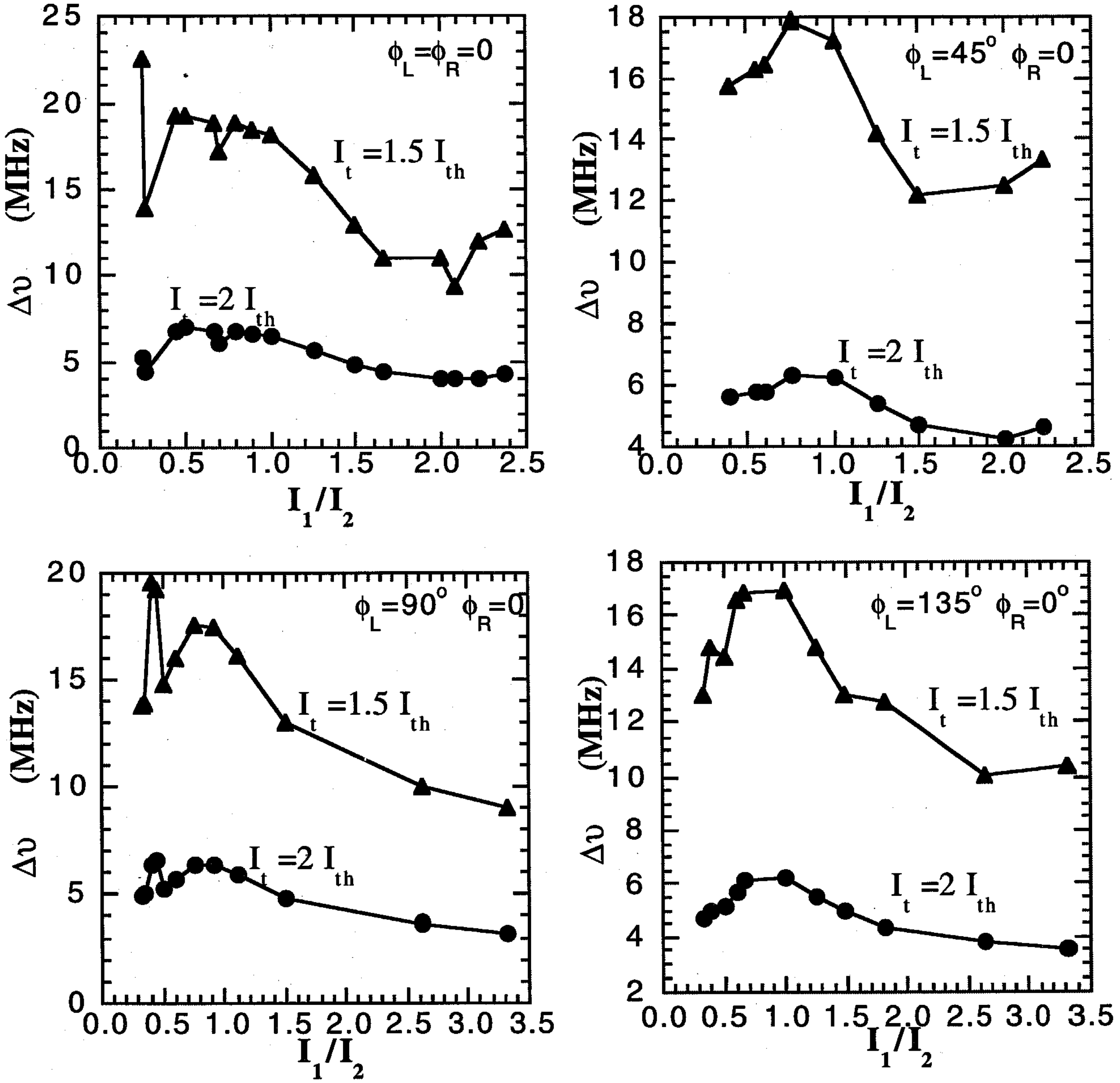

Figure 4.6: The calculated linewidth of the two-section DFB laser at different current ratio of the two electrodes for various assumed values for facet phases.

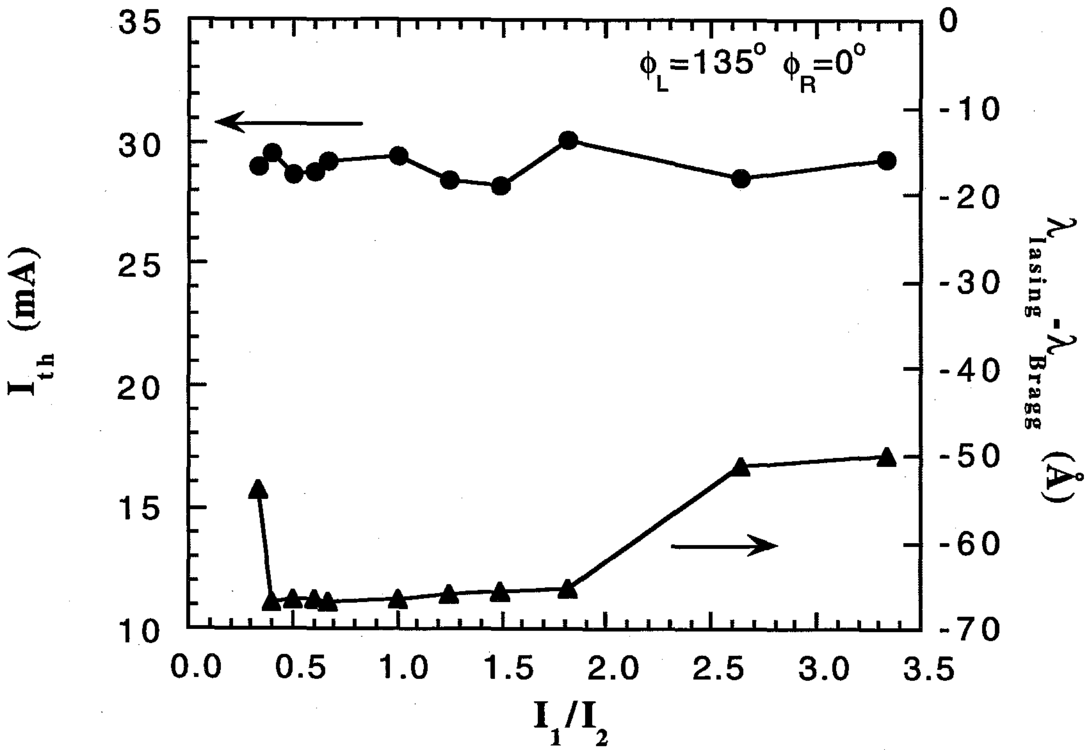

Figure 4.7: The calculated threshold and lasing wavelength of the DFB laser for facet phases $\phi_L=135°$, $\phi_R=0°$.

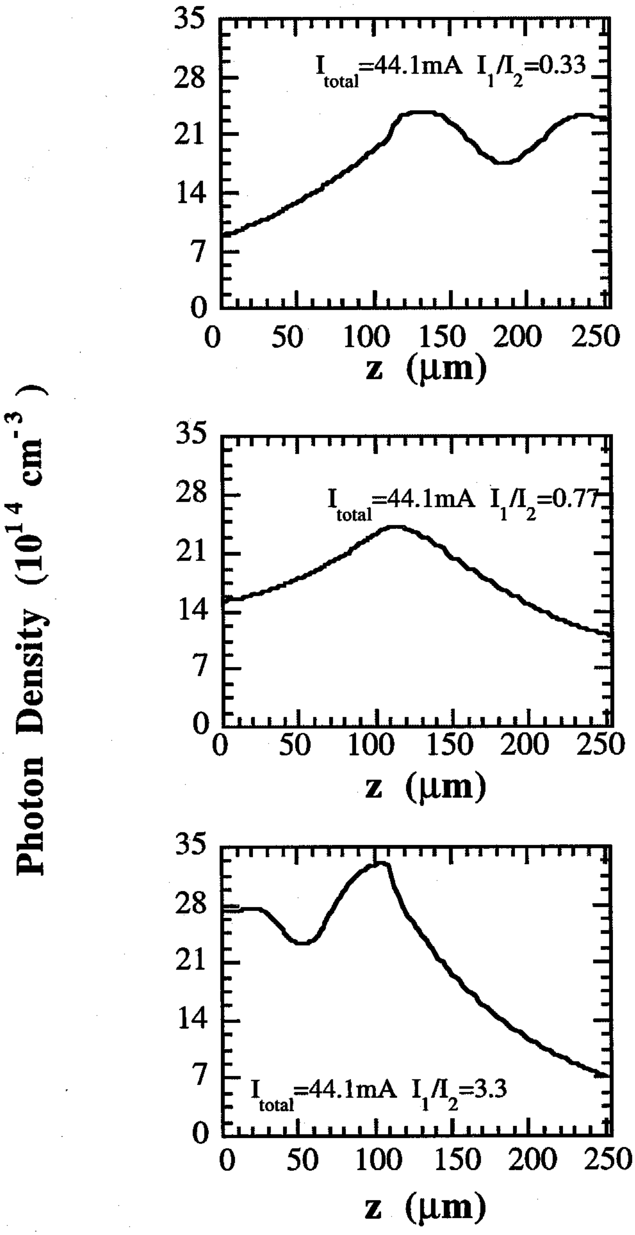

Figure 4.8: The longitudinal photon distribution in the DFB laser for facet phases $\phi_L=135°$, $\phi_R=0°$. The current ratio is assumed to be $I_1/I_2=0.33$, *0.77, and 3.3.*

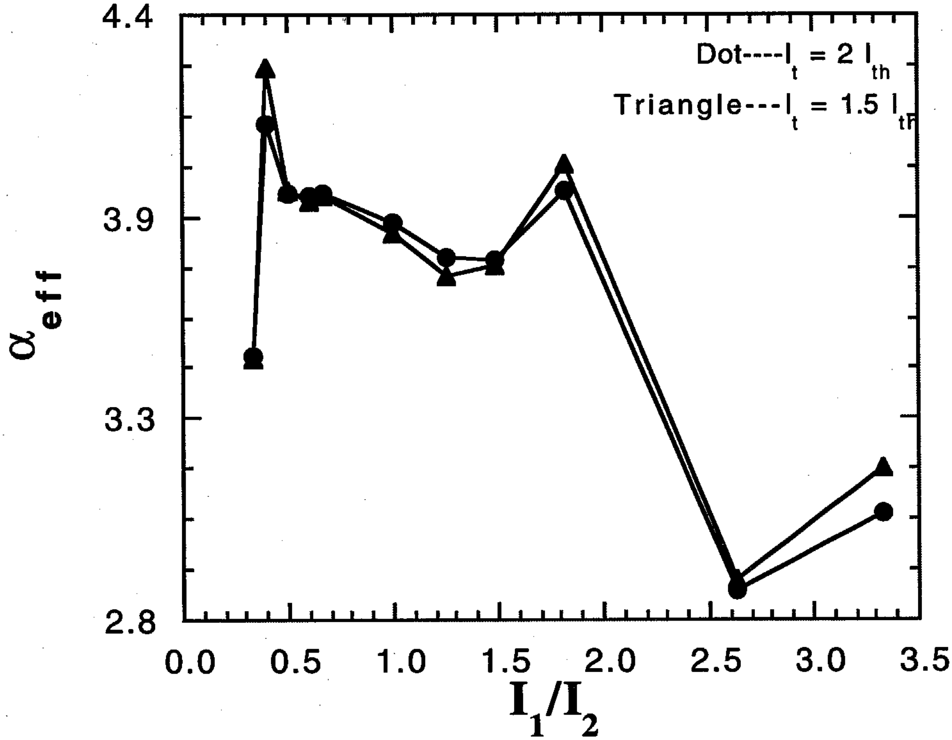

Figure 4.9: The calculated effective linewidth enhancement factor of the DFB laser for facet phases $\phi_L=135°$, $\phi_R=0°$.

To understand the experiment results, the above threshold DFB model (Chapter 3) which includes LSHB is used to calculate the linewidth of the DFB laser. We neglect the linewidth broadening contributed by the noise from carrier diffusion. Because the facet phases are difficult to determine from the experiment, several values of them have been assumed in our calculation of the linewidth (Fig. 4.6). In the calculation, the width between two electrodes is chosen as 10μm, the carrier lifetime 2ns, the differential gain 3×10^{-16} cm ^{2}, the waveguide confinement factor 0.2, and the loss from absorption and scattering 40 cm^{-1}. The linewidth is obtained at $I_t = 1.5\ I_{th}$ and $I_t = 2\ I_{th}$, where I_{th} is the threshold current with uniform current injection. It is found that the linewidth is small for either $I_1/I_2 = 0.2\text{-}0.3$ or $I_1/I_2 = 2.5\text{-}3.5$. At those ratios, the small linewidth has also been measured. The DFB laser is found to be multimode for either $I_1/I_2 < 0.2$ or $I_1/I_2 > 3.5$. This may explain the extremely large linewidth we obtained in the measurement. The calculated linewidth is sensitive to the facet phases. It seems that the linewidth in Fig. 4.6 is the result closest to the measurement.

The threshold current and lasing wavelength are simulated in Fig. 4.7. The threshold current doesn't change very much with the current ratio. It is found that mode switching occurs for those current ratios at which the linewidth is very large.

To examine that the SHB is important in linewidth broadening, the photon distribution is shown in Fig. 4.8 for $I_1/I_2 = 0.33,\ 0.77,\ and\ 3.3$. The linewidth at $I_1/I_2 = 0.33\ and\ 3.3$ corresponds to the minima in Fig. 4.6 ($\phi_L = 135°$, $\phi_R = 0°$). Fig. 4.8

shows that LSHB is serious under uniform injection ($I_1/I_2=0.77$). From (4.49), the influence of SHB on the linewidth comes from its influence on α_{eff} and R, which are dependent on the photon distribution. The total photon number I_o is proportional to the output power and the function of the injection current. The effective linewidth enhancement factor α_{eff} is shown in Fig. 4.9. The α_{eff} is very much affected by LSHB and can change greatly. It is large when the LSHB is serious (Fig. 4.8). Large α_{eff} will result in large linewidth even if the material α is small. The α_{eff} is also found to be nearly independent on the total injected current.

4.5 Conclusion

In this chapter a small signal model for SLM DFB lasers including LSHB is presented. The solution of the coupled-mode equations has been solved by the Green's function method. The rate equations for the photon density and the phase of the optical field in DFB lasers have been derived. The model can be used above threshold in a self-consistent way if the photon and carrier density distributions are calculated by including LSHB.

The effects of nonuniform photon density distribution on the high frequency response of DFB lasers are studied. The resonance frequency and damping rate of a two-section DFB laser is measured as the functions of optical power for various current injections. At the same optical power level, the resonance frequency and damping rate are different for different photon density distributions. We have also measured the linewidth of a 1.55 μm two-section DFB laser. It is found that by adjusting the current ratio between two electrodes, the linewidth can be minimized. Our theoretical analysis of the linewidth of the laser gives similar results to the experiment. It shows that LSHB does play an important role in the broadening of the linewidth.

Reference

[1] H. Statz, and G. deMars, *Quantum Electronics* (Ed. by C. H. Towns, Columbia University Press, New York, 1960), p. 530

[2] K. M. Lau, and A. Yariv, *IEEE J. Quantum Electron.*, **QE-21**, 121 (1985)

[3] J. B. Moreno, *J. Appl. Phys.* 48, 4152 (1977)

[4] J. Feng, T. R. Chen, and A. Yariv, (to be published)

[5] M. Kuznetsov, A. E. Willner, and I. P. Kaminov, *Appl. Phys. Lett.* 55, 1826 (1989)

[6] R.J. Lang, and A. Yariv, *IEEE J. Quantum Electron.*, **QE-21**, 1683 (1985)

[7] R.J. Lang, and A. Yariv, *IEEE J. Quantum Electron.*, **QE-22**, 436 (1986)

[8] A.Yariv, *Quantum Electronics*, 3rd ed., ch. 11 (1989)

[9] M. Kuznetsov, *IEEE J. Quantum Electron.*, **QE-24**, 1837 (1988)

[10] B. Tromborg, H. Oslesen, and X. Pan, *IEEE J. Quantum Electron.*, **QE-27**, 178 (1991)

[11] P. Vankwikelberge, G. Morthier, and R. Baets, *IEEE J. Quantum Electron.*, **QE-26**, 1728 (1990)

[12] T. Schrans, *Ph.D. Thesis, California Institute of Technology*, Pasadena, Calif., 1994

[13] C.H. Henry, *IEEE J. Lightwave Technol.* **LT-4**, 288 (1986)

[14] J. Feng, T. R. Chen, and A. Yariv, *Appl. Phys. Lett.* 67, 3706 (1995)

[15] P.A. Morton, T. Tanbunek, R.A. Logan, A.M. Sergent, P.F. Sciortino, and D.L. Coblentz, *IEEE Phot. Tech. Lett.* 4, 133 (1992)

[16] A.Yariv, *Quantum Electronics*, 3rd ed., ch. 21 (1989)

[17] K. Kikuchi, *Electron. Lett.* 24, 1001 (1988)

[18] K. Kikuchi, *IEEE J. Quantum Electron.,* **QE-25**, 684 (1989)

[19] M. Okai, T. Tsuchiya, K. Uomi, N. Chinone, and T. Harada, *IEEE Phot. Tech. Lett.* 3, 427 (1991)

[20] M. Okai, T. Tsuchiya, K. Uomi, N. Chinone, and T. Harada, *IEEE Phot. Tech. Lett.* 4, 526 (1992)

[21] X. Pan, H. Oslesen, and B. Tromborg, *Electron. Lett.* 26, 1074 (1990)

Chapter 5

Small Frequency Chirp Distributed Feedback Lasers

5.1 Introduction

Until most recently, the understanding of frequency chirp in single mode semiconductor lasers has been very limited. It is widely known that undesirable spectral broadening of single mode DFB lasers often exists when the lasers are under amplitude current modulation (AM) [1-5]. It is believed that the frequency chirp is due to the index variation caused by injection current modulation [6-7], and the axial variation in carrier density attendant upon the longitudinal photon density variation (spatial hole burning) [8-9]. A simple relation between optical output power and optical frequency was derived, in which a linewidth enhancement factor (α parameter) links the frequency chirp and the instantaneous optical power when the lasers directly modulated [6]. Means for reducing the frequency chirp have included the use of laser with a smaller linewidth enhancement factor of the active material [10] and methods which reduce the longitudinal spatial hole burning (LSHB) [11-12]. The second approach involves fabrication of either complex laser structures which introduce gain coupling or quarter-wavelength-shift three-section DFB lasers. With those methods, DFB lasers have chirps about 1Å (which corresponding to 12.5 GHz chirp for 1.55 μm DFB lasers). In high bit rate data transmission in optical fiber over long distance, low chirp DFB lasers are urgently needed.

We discover that ultra small chirp ("zero chirp") could be realized in two-section DFB lasers [13]. The reduction of the chirp is due to the effects of carrier density fluctuations in the two sections on the chirp partially compensating each other [14]. The axial carrier density is not uniform in DFB lasers due to the LSHB. In DFB lasers the contribution of local carrier density variation to the frequency chirp is described by an axially varying function ($C_N(z)$ function) which depends on the distribution of the traveling fields in the lasers, rather than by the α parameter in conventional theory for uniform photon density lasers. The difference between DFB lasers and uniform photon density lasers makes it possible to fabricate a "zero chirp" DFB laser with a multisection structure.

In this chapter, we will show that changing the distribution of the photon density along the laser cavity can affect the sign and magnitude of the frequency chirp [15]. By changing the injection currents into the two sections independently, we have a major reduction in frequency chirp in 1.3μm lasers and the production of either positively (chirp increases with time) or negatively (chirp decreases with time) chirped signals. We will also report on the measurement of the frequency chirp of a two-section DFB laser under large signal modulation. The unique advantage for using two-section DFB lasers is that the frequency chirp can be reduced even when LSHB is not completely suppressed.

5.2 Simple relation between intensity modulation and frequency chirp

In this section we derive a simple relation between the intensity modulation and frequency chirp in single longitudinal mode semiconductor lasers assuming a uniform photon distribution. We consider the conventional rate equation for the average photon density in an SLM semiconductor laser

$$\frac{\partial S}{\partial t} = (\Gamma v_g g(N) - \frac{1}{\tau_{sp}})S + \frac{\Gamma\beta_{sp}N}{\tau_{sp}} \tag{5.1}$$

where Γ is the mode confinement factor, $g(N)$, the optical gain, τ_{ph}, the cavity photon lifetime, τ_{sp}, the spontaneous lifetime, and β_{sp}, the fraction of spontaneous emission into the lasing mode.

We need the frequency shift from some operating point g_0, S_0, and lasing frequency v_0. Without invoking any small signal approximation, we let $g(t)=g_0+\Delta g(t)$ and $S(t)=S_0+\Delta S(t)$. We adopt the approximation $g(N)\approx a(N-N_t)$. (5.1) is rewritten as

$$v_g\Gamma\Delta g(t) = \left[\frac{\partial S}{\partial t} + \frac{\Delta S(t)}{S_0}\,\frac{\Gamma\beta_{sp}N_{bias}}{\tau_{sp}}\right] / \left[S + \frac{\beta_{sp}}{av_g\tau_{sp}}\right] \tag{5.2}$$

(5.2) is then reformulated in terms of the complex effective refractive index, $n_{eff} = n'_{eff} + i\, n''_{eff}$, with positive n''_{eff} representing gain

$$\Delta g(t) = 4\pi\, \Delta n''_{eff} / \lambda \tag{5.3}$$

and we also employ the linewidth enhancement factor which is

$$\alpha = - \frac{\partial n'_{eff}}{\partial N} / \frac{\partial n''_{eff}}{\partial N} \tag{5.4}$$

The α factor here is assumed to be not strongly carrier density dependent. Then we can say that $\Delta n'_{eff} = \alpha\ \Delta n''_{eff}$.

The laser frequency chirp $\Delta\nu$ associated with $\Delta n'_{eff}$ is taken to first order as

$$\frac{\Delta \nu}{\nu} = - \frac{\Delta n'_{eff}}{n'_{eff}} \tag{5.5}$$

With (5.2), we then obtain

$$\Delta \nu(t) = \frac{\alpha}{4\pi} \left(\frac{\partial \ln S(t)}{\partial t} + \frac{\Delta S(t)}{S(t) S_0} \frac{\Gamma \beta_{sp} N_{bias}}{\tau_{sp}} \right) / \left(1 + \frac{\beta_{sp}}{S(t)\, a v_g \tau_{sp}} \right) \tag{5.6}$$

For system application it is easily verified by inserting numbers in (5.6) that, apart from very low optical powers, we obtain [7]

$$\Delta \nu(t) \approx \frac{\alpha}{4\pi} \frac{\partial \ln S(t)}{\partial t} \tag{5.7}$$

With considering the gain suppression, the gain is given as

$$g(N, S) \approx a\, (N - N_t)\, (1 - \varepsilon\, S) \tag{5.8}$$

Then (5.1) is rewritten with (5.8) and we can rederive the expression for frequency chirp as [6]

$$\Delta \nu(t) \approx \frac{\alpha}{4\pi}\left(\frac{\partial \, ln \, S(t)}{\partial t} + \frac{\varepsilon S(t)}{\tau_{ph}}\right) \tag{5.9}$$

This is a very useful relation. For a given intensity modulation, it predicts the related frequency chirp. However, the analysis is oversimplified, since a uniform photon density is assumed. In DFB lasers, due to the nonuniformity of photon density and carrier density (spatial hole burning), (5.9) does not accurately describe the frequency chirp. The rate equations (4.22) and (4.23) for photon density and the phase of optical field in DFB lasers have to be used to solve the frequency chirp.

5.3 Propagation of optical signals in fibers

5.3.1 Time-bandwidth product of chirped pulses

In order to estimate the spectral width for a given pulse shape *S(t),* one has to consider the field with respect to amplitude and phase by, e.g., considering the complex field amplitude

$$E(t) = \sqrt{S(t)} \; exp(j\phi(t)) \tag{5.10}$$

$\phi(t)$ is related to $S(t)$ according to (5.9) by considering

$$\frac{d\phi(t)}{dt} = 2\pi\,(\nu - \nu_{th}) \tag{5.11}$$

For a first-order estimation we shall neglect the influence of nonlinear gain, carrier inhomogeneity and spontaneous emission. Thus, (5.9) yields

$$\frac{d\phi(t)}{dt} \approx \frac{\alpha}{2} \frac{d ln\, S(t)}{dt} \tag{5.12}$$

Using (5.12), the relation between the complex amplitude $E(t)$ and the photon density $S(t)$ is obtained as

$$E(t) = \left[S(t)\right]^{(1+i\alpha)/2} \tag{5.13}$$

We are going to consider a Gaussian pulse shape which has normalized photon density as

$$S(t) = exp\ (-(t//\tau_0)^2) \tag{5.14}$$

with a pulse width (full width half maximum)

$$\tau = 2\sqrt{ln\ 2}\ \tau_0 \tag{5.15}$$

(5.12) yields a linear chirp for this Gaussian pulse:

$$\frac{d\phi(t)}{dt} = -\ \alpha\, t / \tau_0^2 \tag{5.16}$$

After performing the Fourier transform, the Gaussian pulse also yields a Gaussian shape spectrum

$$I_E(\omega) = |E(\omega)|^2 \approx exp(-(\omega/\Omega_g)^2) \tag{5.17}$$

with

$$\Omega_g = (1/\tau_0)\ \sqrt{1+\alpha^2} \tag{5.18}$$

The spectrum of the pulse is obtained as the Fourier transform of (5.14)

$$E(\omega) = \int_{-\infty}^{+\infty} E(t)\ exp(-i\omega t)\ dt \tag{5.19}$$

The spectral width (full width half maximum) Δν with respect to the optical frequency is related to Ω_g as

$$\Delta\nu = 2\sqrt{ln\ 2}\ \Omega_g\ /2\pi \tag{5.20}$$

finally yielding for the time-bandwidth product of Gaussian pulses [16]

$$\Delta\nu\ \ \Delta\tau = 0.44\ \Omega_g\ \tau_0\ = 0.44\ \sqrt{1+\alpha^2} \tag{5.21}$$

5.3.2 Transmission of chirped pulses over single-mode fibers

If a single-mode fiber of length L is used as the transmission medium, the transmission of field to the output field is described by a propagation factor *exp(-iβL)* with the propagation constant β. Since the optical pulse only comprises frequency components close to the center frequency ω_0, the propagation constant β may be expanded around $\omega=\omega_0$, yielding

$$\beta(\omega) = \beta_0 + \ \beta_1\ (\omega\text{-}\omega_0) + \frac{1}{2}\,\beta_2(\omega\text{-}\omega_0)^2 + \cdots \tag{5.22}$$

The parameters β_1 and β_2 are related to the refractive index n and its derivatives through the relations

$$\beta_1 = \frac{1}{c}\left[n + \omega\frac{dn}{d\omega}\right] = \frac{1}{v_g} \tag{5.23}$$

$$\beta_2 = \frac{1}{c}\left[2\frac{dn}{d\omega} + \omega\frac{d^2n}{d\omega^2}\right] \approx \frac{\lambda^3}{2\pi c^2}\ \frac{d^2n}{d\lambda^2} \tag{5.24}$$

Optical pulses broaden with the distance of propagation due to the group velocity dispersion of the fiber $\frac{dv_g}{d\omega} \neq 0$. We define the dispersion parameter

$$D = \frac{d\beta_1}{d\lambda} = -\frac{2\pi c}{\lambda^2}\beta_2 \approx -\frac{\lambda}{c}\frac{d^2n}{d\lambda^2} \tag{5.25}$$

Most of the installed fiber base in the world today has a zero dispersion at $\lambda \approx 1.33\ \mu m$ and a $D \approx 17$ psec/nm-km at $\lambda = 1.55\ \mu m$.

The input and output pulses are described by their slowly varying complex field amplitudes according to (5.10) with $E(t)=E_{in}(t)$ for the input pulse and $E(t)=E_{out}(t)$ for the output pulse or their respective Fourier transforms $E_{in}(\omega)$ and $E_{out}(\omega)$ as in (5.19) yielding

$$E_{out}(\omega) = exp(-i\beta_0 L)\ exp(-i\beta_1 L\omega)\ exp(i\,\frac{\lambda^2}{4\pi c}DL\omega^2)\ E_{in}(\omega) \tag{5.26}$$

After applying the Fourier-transform relationships to $E_{in}(\omega)$ and $E_{out}(\omega)$, the relation between the input and output fields, $E_{in}(t)$ and $E_{out}(t)$, is obtained. Therefore, the related input and output pulse shape in the optical power $P_{in}(t) \sim |E_{in}(t)|^2$ and $P_{out}(t) \sim |E_{out}(t)|^2$ are obtained. For input/output relationship the phase term $exp(-i\beta_0 L)$ is irrelevant and the term $exp(-i\beta_1 L\omega)$ just corresponds to a time delay of $\beta_1 L$ between the input and output pulses so that the change in pulse shape between the input and output pulses is solely described by the term $exp[i\,(\lambda^2/4\pi c)DL\omega^2]$. The formalism described above can be applied to any shape of the input pulse. In this chapter, we restrict discussion to the transmission of Gaussian pulses.

After applying the Fourier transform to an input Gaussian pulse, which is described by (5.14), one obtains $E_{in}(\omega)$. (5.26) then yields $E_{out}(\omega)$ from which the inverse Fourier transform $E_{out}(t)$ is obtained. For the Gaussian input, the output is also Gaussian,

$$P_{out}(t) \sim \left|E_{out}(t)\right|^2 \sim exp(-[(t-\beta_1 L)/\tau(L)]) \tag{5.27}$$

with

$$\left[\tau(L)\right]^2 = \frac{D^4 L^2 (\lambda^2/2\pi c)^2 + (\tau_0^2 + \alpha D^2 L\, \lambda^2/2\pi c)^2}{\tau_0^2} \tag{5.28}$$

$\tau(L)$ becomes very large for large τ_0 as well as very small $\tau_0 \rightarrow 0$. The minimum output pulse width is obtained for

$$\tau_0^2 = \sqrt{1+\alpha^2}\, D^2 L\, \lambda^2/2\pi c \tag{5.29}$$

yielding $\tau_0 \rightarrow \tau_{0,\, min}$

$$\left(\tau(L)\right)^2_{min} = 2\left(\sqrt{1+\alpha^2}+\alpha\right) D^2 L\, \lambda^2/2\pi c \tag{5.30}$$

With (5.15) and (5.30), the output pulse width is given as

$$\Delta\tau_{min}(L) = 2\sqrt{ln\ 2}\ \tau_{min}(L) = \left(\frac{\sqrt{1+\alpha^2}+\alpha}{\sqrt{1+\alpha^2}}\right)^{1/2} \Delta\nu\ D^2 L\, \lambda^2/c \tag{5.31}$$

Numerous research efforts are pursuing various approaches for alleviating the broadening of optical pulses in fibers. These include:

1. Using two fibers in each link with opposite dispersion $D_1 L_1 = -D_2 L_2$ to renarrow broadened pulses,
2. Using mid-span optical phase conjugation to renarrow the pulses,

3. Eliminating chirp from lasers or generating pre-chirped laser pulses.

We will focus our effort on reducing the laser chirp, which, comparing with other methods, could be the most efficient and economic way to overcome the broadening of the pulses in fibers.

5.4 Theoretical foundation of the frequency chirp reduction in two-section DFB lasers

The optical field in DFB laser is described by the coupled-mode equations (2.14) and (2.15). The solution of the equations is obtained through a spatial integration of Green's function weighted with driving force[17-18]. The rate equations for the optical power and the phase of the optical field are given in Chapter 4 as

$$\frac{d}{dt}P(t) = 2P(t)\left[\int_0^l Re\{C_N(z)\}\Delta N(z,t)\,dz + \int_0^l Re\{C_S(z)\}\Delta S(z,t)\,dz\right] + R + F_P(t) \tag{5.32}$$

$$\frac{d}{dt}\phi(t) = \left[\int_0^l Im\{C_N(z)\}\Delta N(z,t)\,dz + \int_0^l Im\{C_S(z)\}\Delta S(z,t)\,dz\right] + F_\phi(t) \tag{5.33}$$

where

$$C_X = -j\, E^+(z)\, E^-(z) \frac{\partial\beta}{\partial X}(z) \,/\, \{ \int_0^l E^+(z')\, E^-(z') \frac{\partial\beta}{\partial\omega}(z')\, dz' \} \tag{5.34}$$

and for a single-mode DFB laser, the transverse electric field can be represented by

$$E(z,t) = E^+(z,t)\, exp[-i\beta z+i(\omega_0+\Delta\omega)t] + E^-(z,t)\, exp[+i\beta z+i(\omega_0+\Delta\omega)t] \tag{5.35}$$

where $X= N, S$. Here R is the spontaneous emission coupled into lasing mode, and S , the photon density. $E^+(z), E^-(z)$ are the forward and backward propagating electric fields in the laser, and β is the propagation constant of the lasing mode. $\Delta N(z,t), \Delta S(z,t)$ are the deviations of carrier and photon densities from their stationary distributions under DC bias. F_P and F_ϕ are Langevin noise sources related to spontaneous emission. The derivatives of β are

$$\frac{\partial\beta}{\partial N} = \frac{j}{2}(1+j\alpha)\frac{\partial g}{\partial N} \tag{5.36a}$$

$$\frac{\partial\beta}{\partial S} = -\frac{j}{2}\frac{\varepsilon g}{1+\varepsilon S} \tag{5.36b}$$

$$\frac{\partial\beta}{\partial\omega} = \frac{1}{v_g} + \frac{j}{2}\frac{\partial g}{\partial\omega} \tag{5.37}$$

and the modal gain g is given as

$$g\ (z,t) = \frac{a\ [N(z,t)-N_{tr}]}{[\ 1+\varepsilon S(z,t)\ ]} \tag{5.38}$$

where v_g is the group velocity, ε is the nonlinear gain suppression coefficient, and a is the differential gain.

The evolution of carrier density distribution is given by the rate equation

$$\frac{dN(z,t)}{dt}=\frac{J(z,t)}{ed}-\frac{N(z,t)}{\tau}-BN(z,t)^2-CN(z,t)^3-\frac{a\,[N(z,t)-N_{tr}]}{[\,1+\varepsilon S(z,t)\,]}v_g S(z,t) \tag{5.39}$$

In this equation, the nonlinear gain suppression the last term and the Auger recombination rate (CN^3) are included. S is the photon density, and τ is the carrier lifetime.

For small signal modulation, the dynamic variables $J(z,t)$, $N(z,t)$, and $S(z,t)$ can be written as the sum of their stationary distributions and the variations due to RF modulation

$$J(z,t) = J_0(z)+J_1(z,t) \tag{5.40a}$$

$$S(z,t) = S_0(z)+S_0(z)S_1(t) \tag{5.40b}$$

$$N(z,t) = N_0(z)+N_1(z,t) \tag{5.40c}$$

Here $J_0(z)$, $N_0(z)$, and $S_0(z)$ are the stationery distributions in the laser. The dynamic frequency $\omega(t)=\omega_{lase}+\delta\omega(t)$. Combining (5.32), (5.33), (5.39) and (5.40), the frequency chirp of the laser is obtained

$$\delta\omega(t)=\int_0^l Im\{C_N(z)\}N_1(z,t)\,dz+S_1(t)\int_0^l Im\{C_S(z)\}S_0(z)\,dz \tag{5.41}$$

The Langevin noise source F_P and F_ϕ are neglected in the case when the laser bias current is modulated. A temperature dependent adiabatic chirp should be included in (5.41) if the modulation frequency is less than 10 MHz. The first term in (5.41) is known as transient chirp, which is proportional to modulation current; the second term is adiabatic chirp, which depends on the bias current. In our case, the transient chirp is about two orders of magnitude larger than the adiabatic chirp.

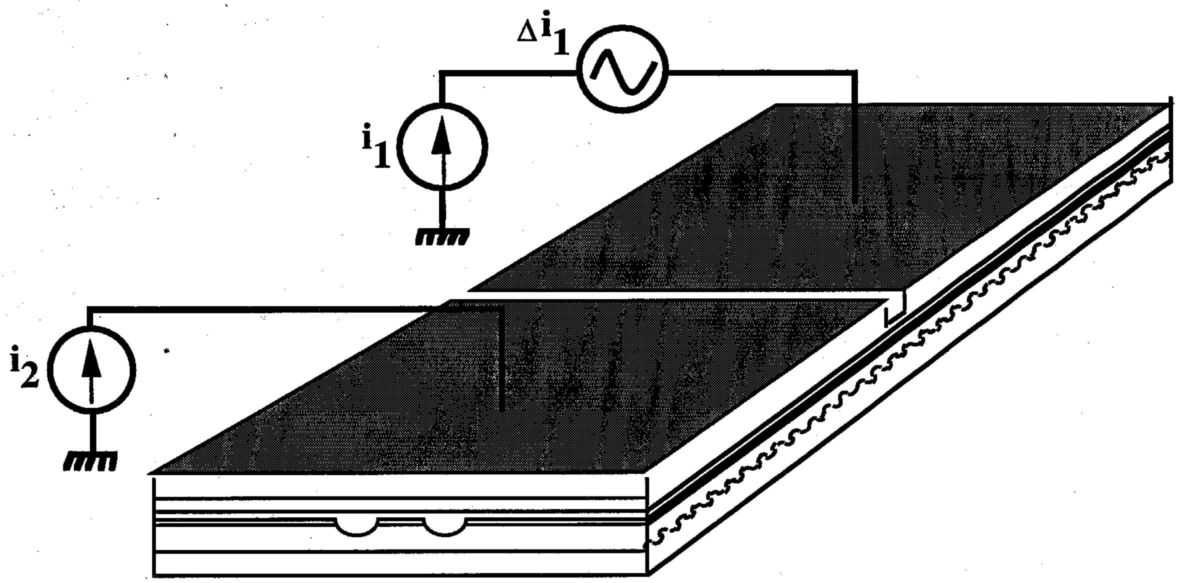

Figure 5.1: A two-section distributed feedback semiconductor laser.

The imaginary part of $C_N(z)$ is the contribution of the local carrier density variation $N_1(z)$ to the frequency chirp. Contrary to its expression in the case of a laser with uniform photon density, where it is a spatially independent constant proportional to α, $Im\{C_N(z)\}$ strongly depends on the distribution of traveling fields $E^+(z)$, $E^-(z)$ and can vary greatly. A small α DFB laser could have very large chirp because $C_N(z)$ is more sensitive to the distribution of $E^+(z)$ and $E^-(z)$. For a two-section DFB laser, if one of the sections is RF modulated, the carrier density variation $N_1(z)$ has two contributions, one from injected modulation current, the other due to carrier depletion of photon density variation. The "zero" chirp of two-section DFB lasers can be realized when one section contributes positive chirp and the other one, equal amount of negative chirp, which is expressed as

$$\int_0^{l_1} Im\{C_N(z)\} N_1(z)\, dz + \int_{l_1}^{l_1+l_2} Im\{C_N(z)\} N_1(z)\, dz \approx 0 \tag{5.42}$$

To calculate the chirp in multisection DFB lasers, a comprehensive computer simulation program introduced in Chapter 3 has been used. The program includes the nonuniformity of optical intensity and carrier density in lasers, which can compute threshold, linewidth and frequency chirp of multisection index coupling and gain coupling distributed feedback lasers.

5.5 Measurement of the frequency chirp in two-section DFB lasers under small signal modulation

5.5.1 Experiment No. 1: Frequency chirp in 1.55μm two-section DFB laser

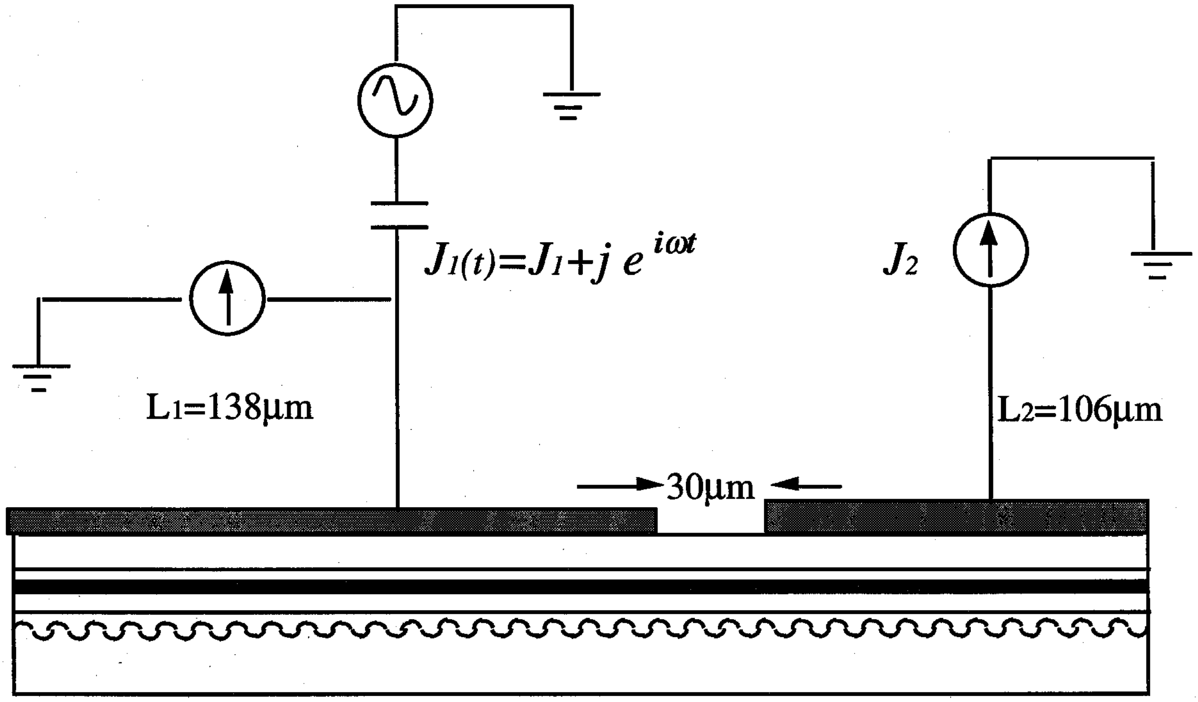

Figure 5.2: A 1.55μm two-section DFB laser used in experiment. The laser has two sections of 138μm and 106μm long, respectively.

A two-electrode 1.55μm InGaAsP/InP DFB laser is fabricated. The laser has one cleaved facet and one AR coated, and the two sections are 106μm and 138μm long with an electric isolation of 1kΩ. The detailed laser structure has been described in Section 4.4. The two sections are pumped with DC currents while one of them is also RF modulated. The laser output is fed into an optical fiber after an isolator of more than 45 dB isolation. The output from the fiber is collimated and sent to a Burleigh RC-140 Fabry-Perot with a resolution of 0.2 GHz and a free spectral range of 15 GHz. The output from the Fabry-Perot is incident on a Ge detector, and the time average spectral density of the optical field of the laser is displayed on an oscilloscope.

The spectral width (frequency chirp) versus the current ratio I_2/I_1 is measured at a modulation frequency of 50 MHz and an RF current of 4mA. The total current into the laser is kept at 70 mA. The result is shown in Fig. 5.3. When the long section is RF modulated, the spectral width of laser has a minimum for $I_1=20mA$ ($I_2/I_1=2.5$). If the short section is RF modulated, the minimum of the chirp occurs for $I_1=15mA$ ($I_2/I_1=3.7$). The chirp increases dramatically when the injected currents are changed from conditions where the chirp is at its minimum. The minima in Fig. 5.3 are less than the resolution of the Fabry-Perot. The behavior of the measured spectral width will be the same as long as the modulation frequency is much smaller than the oscillation frequency of the laser.

The photon density and carrier density distributions at minimum chirp bias are shown in Fig. 5.4. Carrier density is close to uniform in each of the sections due to the different pumpings in two sections. But the photon density shows strong nonuniformity and varies from 6×10^{18} cm^{-3} to 14×10^{18} cm^{-3}. $C_N(z)$ and $N_1(z)$ for the DFB laser are also calculated and shown in Fig. 5.5 and Fig. 5.6. The product of $Im\{C_N(z)\}$ and $N_1(z)$, which gives the chirp form (5.41), can be obtained and is plotted in Fig. 5.6. When the chirp is at its minimum, it can be seen that $N_1(z)$ in the section two is out phase with that in the section one, and the integration of the $Im\{C_N(z)\} \bullet N_1(z)$ along the laser axis is very close to zero. This verifies the minimum chirp condition given by (5.42).

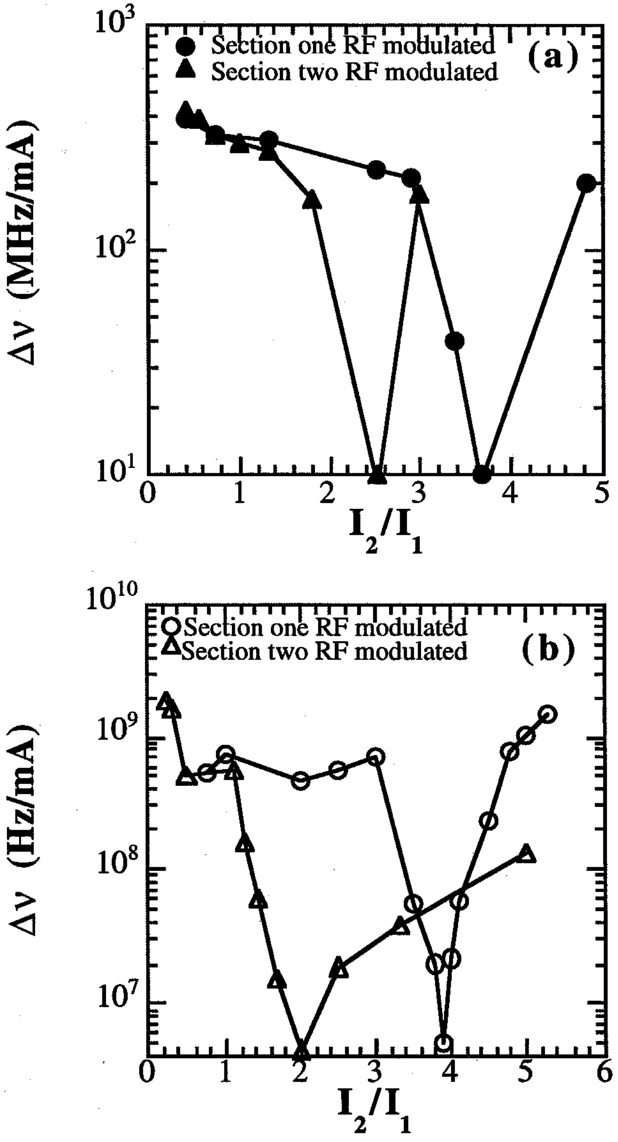

Figure 5.3: (a) The measured spectrum width of 1.55μm two-section DFB laser (L_1=106μm, L_2=138μm), at various ratios, with bias current I_1+I_2=70mA.

(b) The calculated chirp of the two-section DFB laser. The bias current $I_1+I_2=1.75I_{th}$. I_{th} is the calculated threshold current of the DFB laser uniformly pumped.

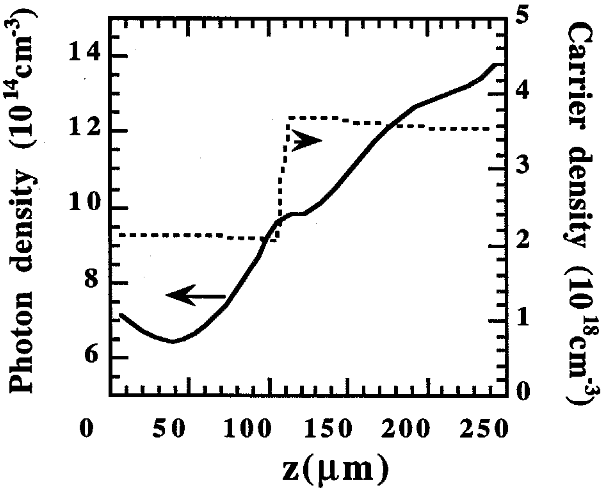

Figure 5.4: Calculated photon and carrier densities of the two-section DFB laser with the 1st section RF modulated. The bias current $I_1+I_2=1.75I_{th}$ and current ratio $I_2/I_1 = 3.9$, which correspond to the minimum chirp condition in (5.42).

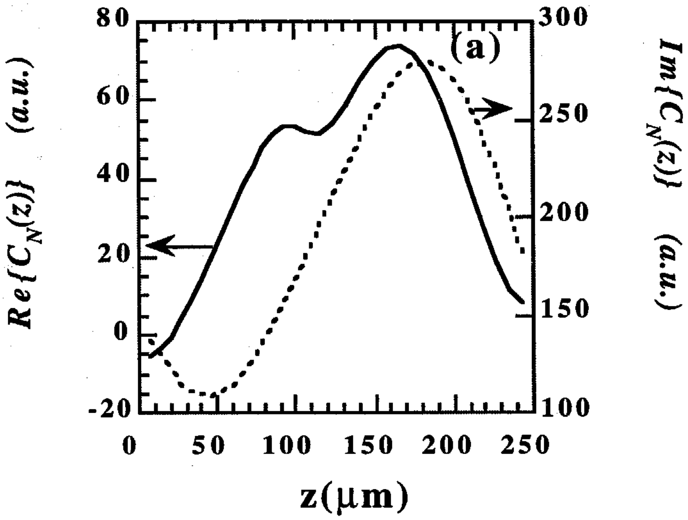

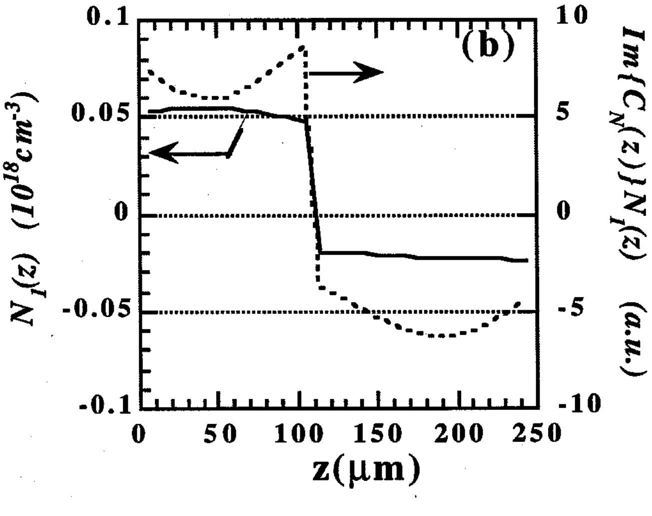

Figure 5.5: (a) Calculated $C_N(z)$ and (b) calculated $N_1(z)$, $N_1(z) \cdot Im(C_N(z))$ at the minimum chirp condition in Fig. 5.2.

5.5.2 Experiment No. 2: Frequency chirp in 1.3μm InGaAsP/InP quantum well two-section DFB laser

A two-electrode 1.32μm strained quantum well InGaAsP-InP DFB laser is used. The laser has cleaved facets, and the two sections are 375μm and 250μm long with an electric isolation 1kΩ. The DFB laser has at least 40 dB of SMSR under CW condition. It has a threshold of 18 mA when uniformly pumped. The coupling coefficient is calculated at κL=3. The light output is collimated and divided by a beamsplitter. One beam is sent to a Coherent No. 240 Fabry-Perot interferometer where FM spectrum is measured, and the other beam is sent to an Ortel 2516A photodiode to determine the intensity modulation index *m* (see Fig. 5.6). The laser is optically isolated with minimum 60 dB isolation.

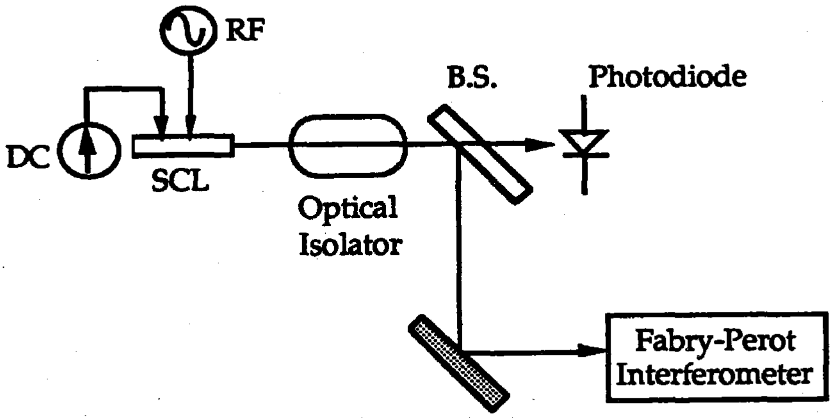

Figure 5.6: Experimental setup for measuring FM/AM response in DFB lasers.

Fig. 5.7 shows a typical measured FM spectrum from the Fabry-Perot interferometer. The phase difference between the AM and FM modulations depends on the modulation frequency ω_m and optical power. Normally, the FM spectrum is asymmetrical at modulation frequency much smaller than the resonant frequency. As the ω_m approaches the resonance frequency, the FM modulation is $\pi/2$ out phase with the AM response and the FM spectrum has equal sidebands around the lasing frequency.

The optical field $E(t)$ can be represented as

$$E(t) = E_0[1+m\ Sin\{(\omega_m t)+\theta_1\}]^{1/2}\bullet exp[i\{\omega_l t-\beta\ Cos(\omega_m t+\theta_2)\}]. \tag{5.43}$$

Here β is the phase modulation index. We write the AM modulation, and FM or frequency chirp as

$$p(t) = m\ Sin(\omega_m t+\theta_1) \tag{5.44}$$

$$\delta\omega(t) = \beta\omega_m Sin(\omega_m t+\theta_2) \tag{5.45}$$

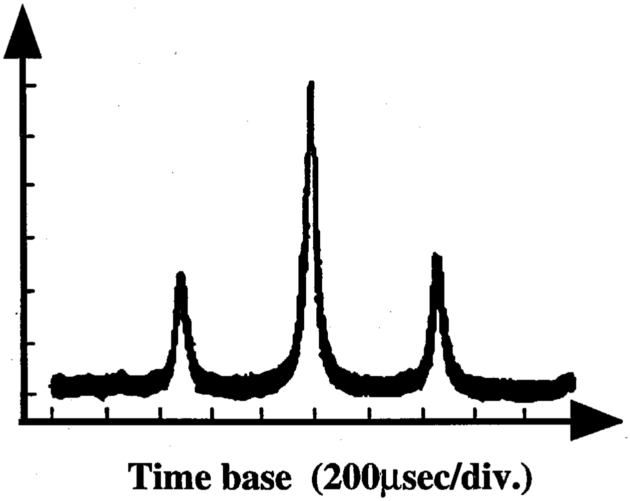

Figure 5.7: A typical output intensity from Fabry-Perot interferometer.

To determine the phase modulation index β and the $\theta_2-\theta_1$, we directly measure the intensity modulation index m from AC output of the Ortel 2516A photodiode with an HP 8565A spectrum analyzer and observe the FM spectrum on the Fabry-Perot interferometer (Fig. 5.7). The heights of the central peak and the first order FM sidebands are given by [19-20]

$$|E(\omega)|^2=J_0^2(\beta)+m^2 J_1^2(\beta)\, sin^2(\theta_2-\theta_1) \tag{5.46}$$

$$\begin{aligned}|E(\omega\pm\omega_m)|^2=J_1^2(\beta)+m^2[J_0^2(\beta)+J_2^2(\beta)]/4+m^2 J_0(\beta)\, J_2(\beta)\, cos[2(\theta_2-\theta_1)]/2 \\ \pm m J_1(\beta)\,[J_0(\beta)+J_2(\beta)]\, cos(\theta_2-\theta_1)\end{aligned} \tag{5.47}$$

where J_n is the nth-order Bessel function of the first kind. The β and the $\theta_2-\theta_1$ can be solved with (5.46) and (5.47).

The measurement is conducted at modulation frequencies $f_m=\omega_m/2\pi=250\ MHz,\ 500\ MHz,\ 800\ MHz$ *and* $1.5\ GHz$. The injection current distribution is changed by adjusting the DC currents into the two sections and the optical power is kept at P = 0.8 mW throughout the measurement. In Fig. 5.8 we show the values of β/m as function of the injection current distribution. We use current density ratio $i_2/i_1=I_2L_1/I_1L_2$, where I_1 and I_2 are the DC currents into the two sections. The uniform pumping condition corresponds to $i_2/i_1=1$. From Fig. 5.8, we see that as the current density ratio i_2/i_1 is increasing, the β/m has large drops at $i_2/i_1=1.3$ (at 250 MHz), 1.7 (at 500 MHz) and 1.85 to 2.3 (at 800 MHz). The β/m decreases approximately by one order of magnitude. It is expected that the condition for 'zero chirp' (5.42), is approximately satisfied at those injection current distributions. For $f_m = 1.5\ GHz$, the modulation frequency is close to the resonant frequency, and the β/m is much less sensitive to the optical density distribution and expected to be closed to $\alpha/2$ [21-22]. That is why we have much smaller reduction of β/m at 1.5 GHz modulation by a factor of less than 2 from Fig. 5.8d.

The phase difference $\theta_2-\theta_1$ is also calculated from the observed FM spectrum according to (5.46) and (5.47), and the result is shown in Fig. 5.9. The $\theta_2-\theta_1$ is less than $\pi/2$ for small current ratio i_2/i_1, which corresponds to $|E(\omega+\omega_m)|>|E(\omega-\omega_m)|$. As i_2/i_1 increases until the chirp reaches its minimum, the $\theta_2-\theta_1$ approaches $\pi/2$. If i_2/i_1 increases further, the $\theta_2-\theta_1$ is larger than $\pi/2$ and $|E(\omega+\omega_m)|<|E(\omega-\omega_m)|$.

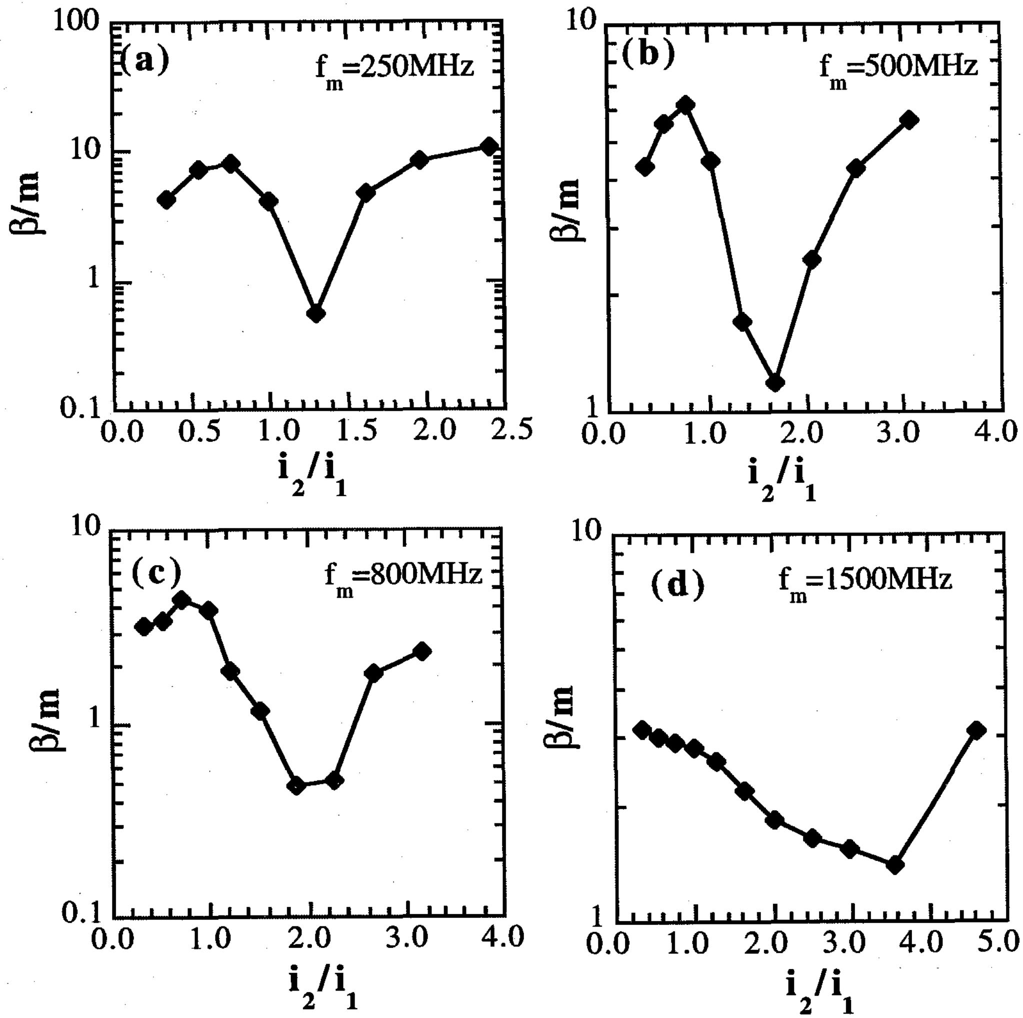

Figure 5.8: The measured β/m of 1.3μm InGaAsP/InP QW two-section DFB laser (L_1=375μm, L_2=250μm) for various current density ratios i_2/i_1. The two-section DFB laser is under AM modulation: (a) $f_m = 250$ MHz, (b) $f_m = 500$ MHz, (c) $f_m = 800$ MHz, (d) $f_m = 1.5$ GHz.

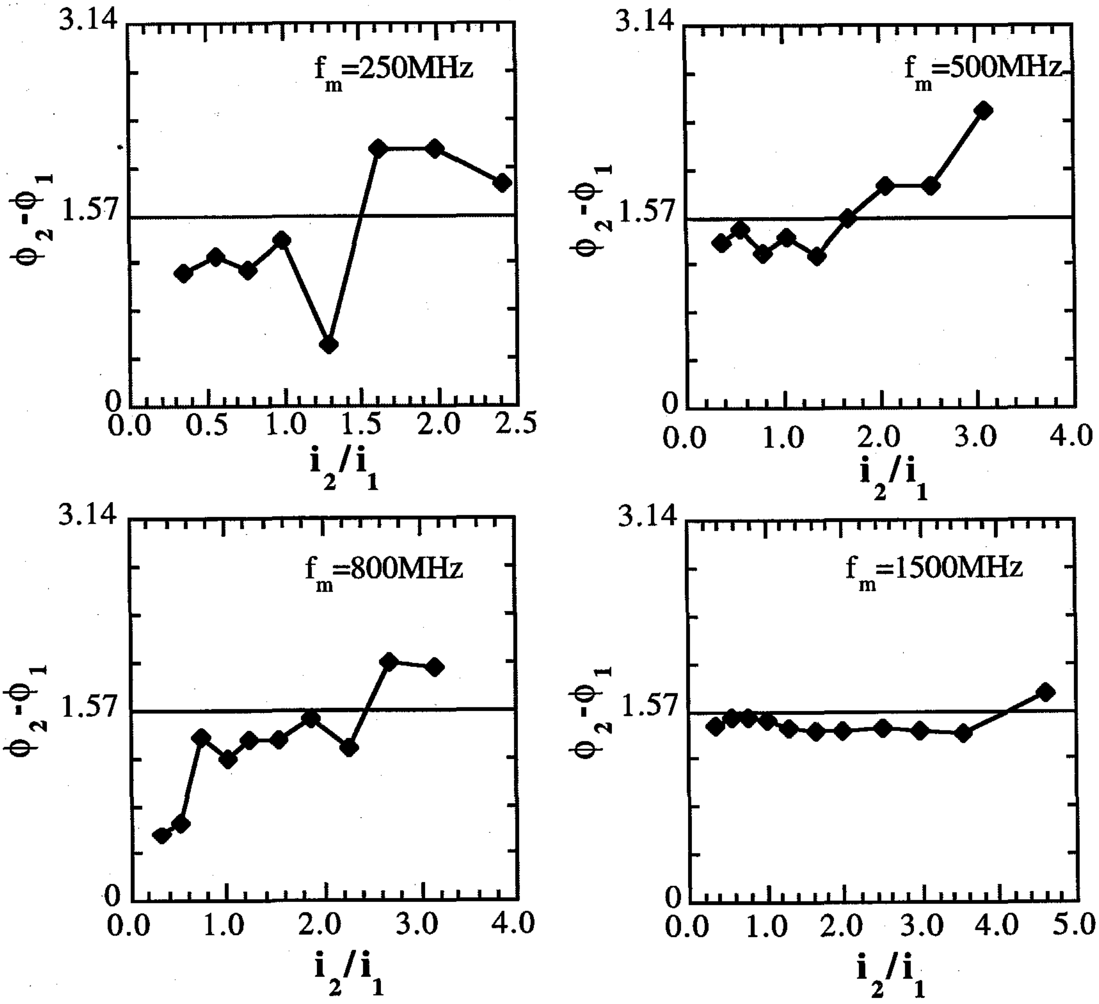

Figure 5.9: The phase difference $\theta_2 - \theta_1$ as a function of the current density ratio i_2/i_1 from the measured FM spectrum of the two-section DFB laser under AM modulation.

5.6 Measurement of the frequency chirp in two-section DFB lasers under large signal modulation

If the photon density is uniform, the frequency chirp can be expressed simply as the combination of the "transient" chirp, which is proportional to the time derivative of the photon density in lasers, and "adiabatic" chirp, which is proportional to the photon density. The chirp in DFB lasers has to be calculated numerically due to the longitudinal photon density variations in the lasers. Numerical simulations of the frequency chirp of one-section DFB lasers have been proposed by several groups [8, 23]. We study the frequency chirp of multisection DFB lasers with a model based on the time-dependent coupled mode wave equations (3.6) and (3.7). The model explains the basic observed features of the frequency chirp of the two-section DFB lasers.

A two-electrode 1.3 μm InGaAsP/InP DFB laser has been used in the experiment. The laser structure has been given in Section 5.5. The two sections are 400μm and 100μm long with an electric isolation of 1.4 kΩ. The threshold current for section one is measured as a function of the injection current in section two and is shown in Fig. 5.10. As the current in section two increases, the active material of section two becomes less absorptive and, eventually, increasingly amplifying. The threshold for section one will thus gradually decrease. The peak in the figure is the stage when the laser switches from one single mode to another mode.

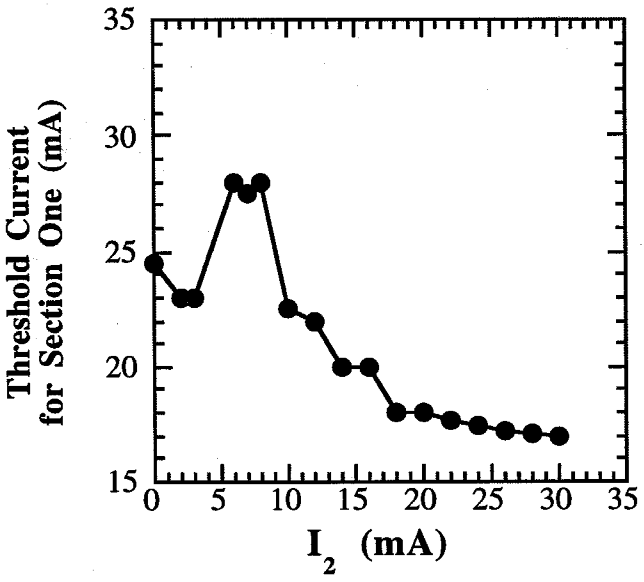

Figure 5.10: Measured threshold of the 1.3μm two-section DFB laser (L_1=400μm, L_2=100μm) for various current ratios.

The two sections are pumped with DC currents while the long one is also AC modulated. In all measurements, section one is biased above threshold. The laser output is collimated and divided by a beamspliter into two beams. One beam is focused onto an Ortel 2516A high speed photodiode, while the other beam is focused on a SPEX 1870 monochromator slit with a resolution of 0.5 Å to observe the modulated light spectrum. The monochromator detection system consists of a Ge detector and a lock-in amplifier. The wavelength of the monochromator is scanned at a low speed of 0.1 Å/s so that the envelope of the dynamic wavelength shift is recorded. The full width at half maximum of the optical spectrum is measured to evaluate the frequency chirp. The output of the photodiode is fed to a sampling oscilloscope where the time waveforms for the modulated light are observed. The section one is biased at $I_1/I_{th}=1.8$ for $I_2=0$, and the optical power is then maintained at that level for various I_2 values by changing the current I_1. The optical modulation index m is monitored by the sampling oscilloscope and fixed at 100 percent by adjusting the AC microwave power (typically 10 dBm) into the section one (see Fig. 5.11).

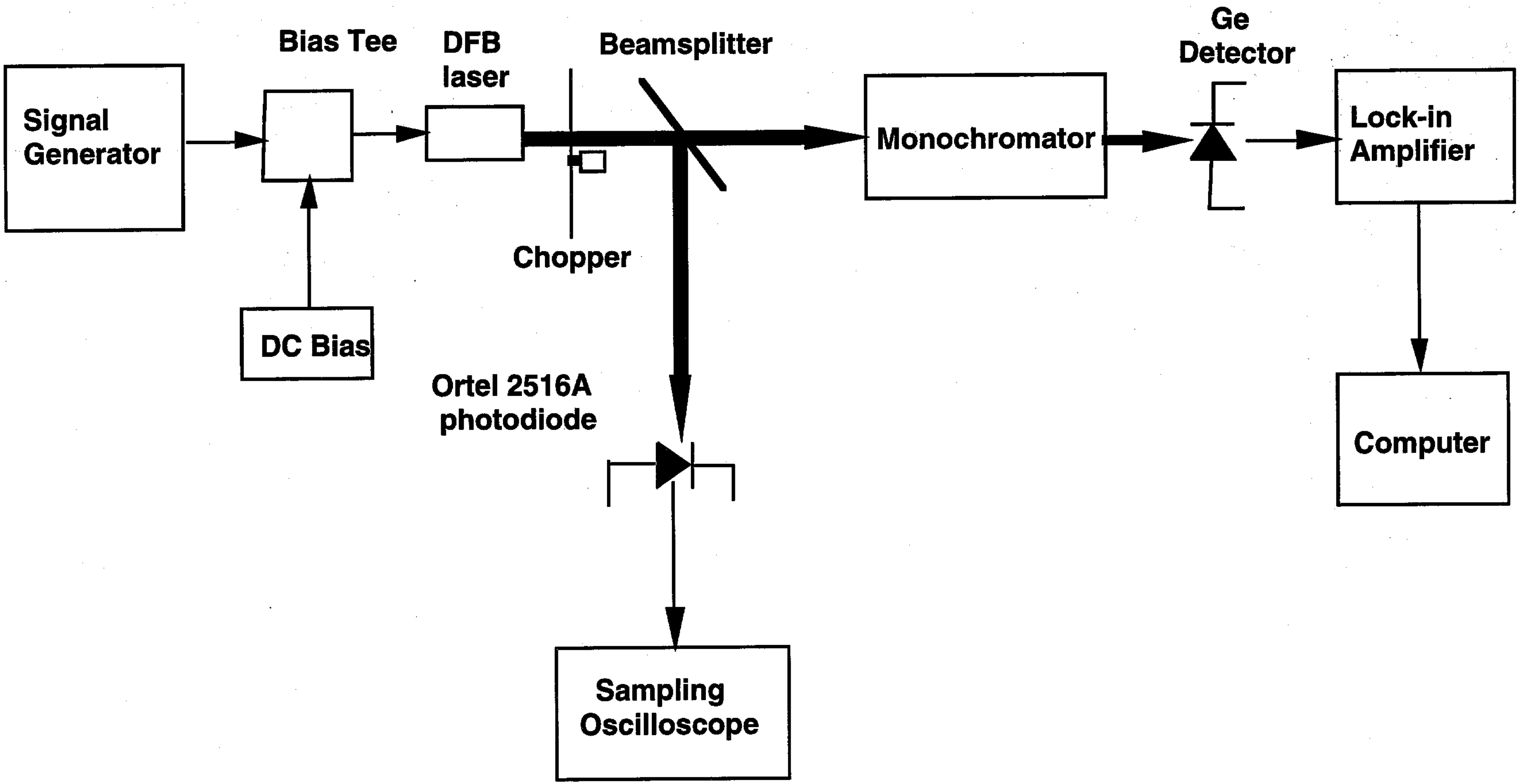

Figure 5.11: Experimental setup for the measurement of the chirp of two-section DFB laser under large signal modulation

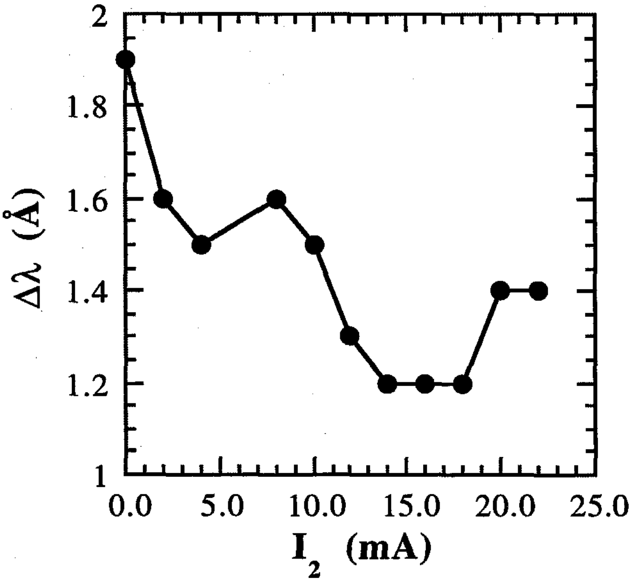

Figure 5.12: The measured frequency chirp of the two-section DFB laser with optical modulation index $M=100\%$; average optical power is kept at the same level as that of $I_1=1.8I_{th}$ and $I_2=0$. I_{th} is the threshold current for section one when $I_2=0$.

The frequency chirp is measured at a modulation frequency of 5 GHz, and the result is shown in Fig. 5.12. A minimum nears 1.2Å when I_2 is in the range of 14 mA to 18 mA. We find the frequency chirp to be strongly dependent on the modulation frequency. The chirp of the laser is also measured at modulation frequencies of 3 GHz and 2 GHz. The frequency chirp at those modulation frequencies is much smaller than that at 5 GHz. The features of the frequency chirp at those frequencies can not be obtained because for some of the cases the chirp is less than the resolution of the monochromator. It is observed that the distortion of output optical waveform becomes serious when either the modulation current or the modulation frequency increases. The distortion is a result of the relaxation oscillation which is accompanied by a large frequency chirp [9, 24].

Taking into account the spatial hole burning along the laser axis, we calculate the complex reflectivities of a two-section DFB laser by means of the propagator F matrices [25]. The dynamics of the laser under high frequency, large single modulation is calculated with the coupled mode equations (3.6), (3.7) and the rate equation (5.39).

The frequency chirp of the two-section laser using this numerical simulation is shown in Fig. 5.13. The modulation frequency is set to be 5 GHz, and the optical modulation index at 100% with the average optical power kept a constant. The parameters used in the calculation are: a linewidth enhancement factor of 4.8, a nonlinear gain suppression coefficient of 10^{-17} cm^3, a spontaneous emission factor of 10^{-4}, a carrier life-time of 2ns, and a photon lifetime of 1ps. In Fig. 5.13, we observe that the calculated frequency chirp also has a minimum value of 1.43 Å when I_2=7.3mA. For values of I_2

less than 1 mA or greater than 14 mA, we have difficulty with the convergence of the solution for the dynamic lasing condition because the photon density distribution is very asymmetrical. We find that the calculated chirp hardly changes when other values of the phases of the facet reflectivities are used in the calculation. In our calculation, the phases are assumed to be zero. The basic features and the range of values of the numerical analysis are in agreement with the observation.

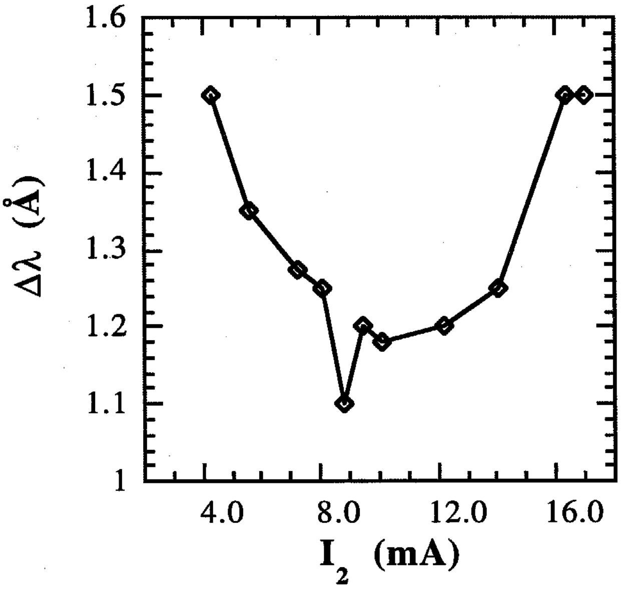

Figure 5.13: The calculated frequency chirp for the two-section DFB laser used in the experiment with optical modulation index *M=100%*, average optical power kept the same. The peak to peak modulation current is about 10 mA.

To explain the reduction of the chirp in two-section DFB laser, we use the average photon densities in each section and the mode frequency shift $\Delta\omega_l$ due to average gain change. ΔG_i in the two sections is then given by [25]

$$\Delta\omega_l = A\ \left(L_1^{eff}\Delta G_1 + L_2^{eff}\Delta G_2 \right) / \left(L_1^{eff} + L_2^{eff} \right) \tag{5.48}$$

Here A is the material constant of the active layer, and we define the effective lengths of the sections as

$$L_i^{eff} \equiv (v_g/2)\frac{\partial \phi_i}{\partial \omega_l} \tag{5.49}$$

To maintain oscillation, the gain change in one section must be compensated by an opposite change in the other section (ΔG_1, ΔG_2 have the opposite values), and L_i^{eff} depends on both the gain (or injection current) [25] and the wavelength detune $\delta=\lambda-\lambda_{bragg}$, where λ_{bragg} is the Bragg wavelength. By adjusting the current distribution in the DFB laser, the effective lengths can be changed significantly. In theory, the frequency chirp $\Delta\omega_l$ can be reduced to zero if we can change the effective lengths by adjusting the current distribution so that $L_1^{eff}\Delta G_1+L_2^{eff}\Delta G_2$ equals zero. However, when taking spatial hole burning into account, a finite frequency chirp $\Delta\omega_l$ results.

5.7 Control of the frequency chirp in DFB lasers

Chirped pulses have been used for pulse compression in optical fibers as a compensation for chromatic dispersion of the fiber [26-28]. To achieve pulse compression, positively chirped or blue-shift chirped (frequency increases with time) pulses are sought in order to compensate the fiber dispersion due to the negative chromatic dispersion ($\beta_2<0$) of fiber at long wavelength (> 1.3μm). Negatively chirped or red-shift chirped (frequency decreases with time) pulses, however, will broaden after traveling in any distance of optical fiber (Fig. 5.14). The time-averaged power spectrum of single section DFB lasers under high speed modulation has been measured by several groups [2-3]. In Fig. 5.15, we show two time-averaged power spectra of directly modulated SLM DFB lasers. One is negatively chirped, the other is positively chirped. Unfortunately, for most directly modulated single section DFB lasers, the spectra are found to be associated with predominantly negative frequency chirp. To get the blue-shift chirped optical pulses, an FM DFB laser and an external intensity modulator had to be used [28].

Pulse Compression in Optical Fiber

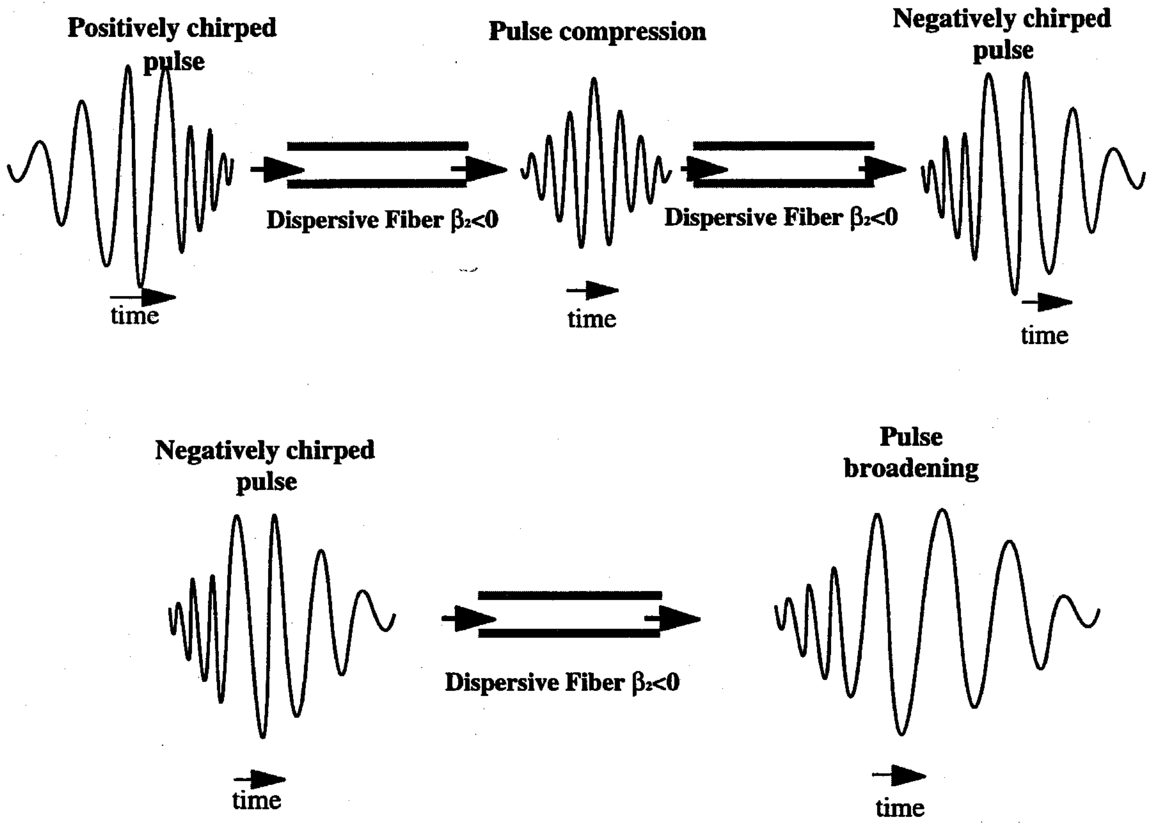

Figure 5.14: Optical pulse propagation in optical fibers.

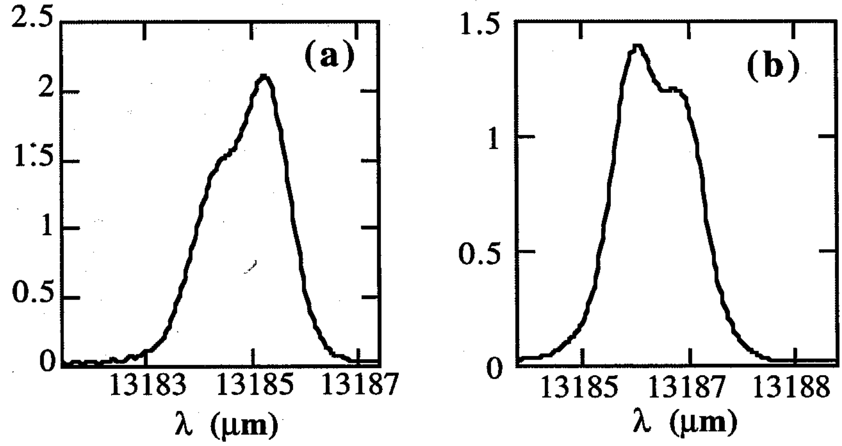

Figure 5.15: Time-averaged power spectra from directly modulated DFB lasers; (a) Negatively chirped spectrum (b) Positively chirped spectrum.

We show in this section the control of frequency chirp of a two-section DFB laser by nonuniform current injection and the achievement of blue-shift optical signals from the two-section DFB laser under direct current modulation. The 1.3 µm InGaAsP/InP DFB laser has two sections of 400µm and 100µm long. Through a measurement of the time-averaged power spectrum of the laser at 5 GHz modulation with fixed optical modulation index, the changing frequency chirp is demonstrated for various distributions of longitudinal photon density. The detailed experimental procedure has been described in Section 5.6.

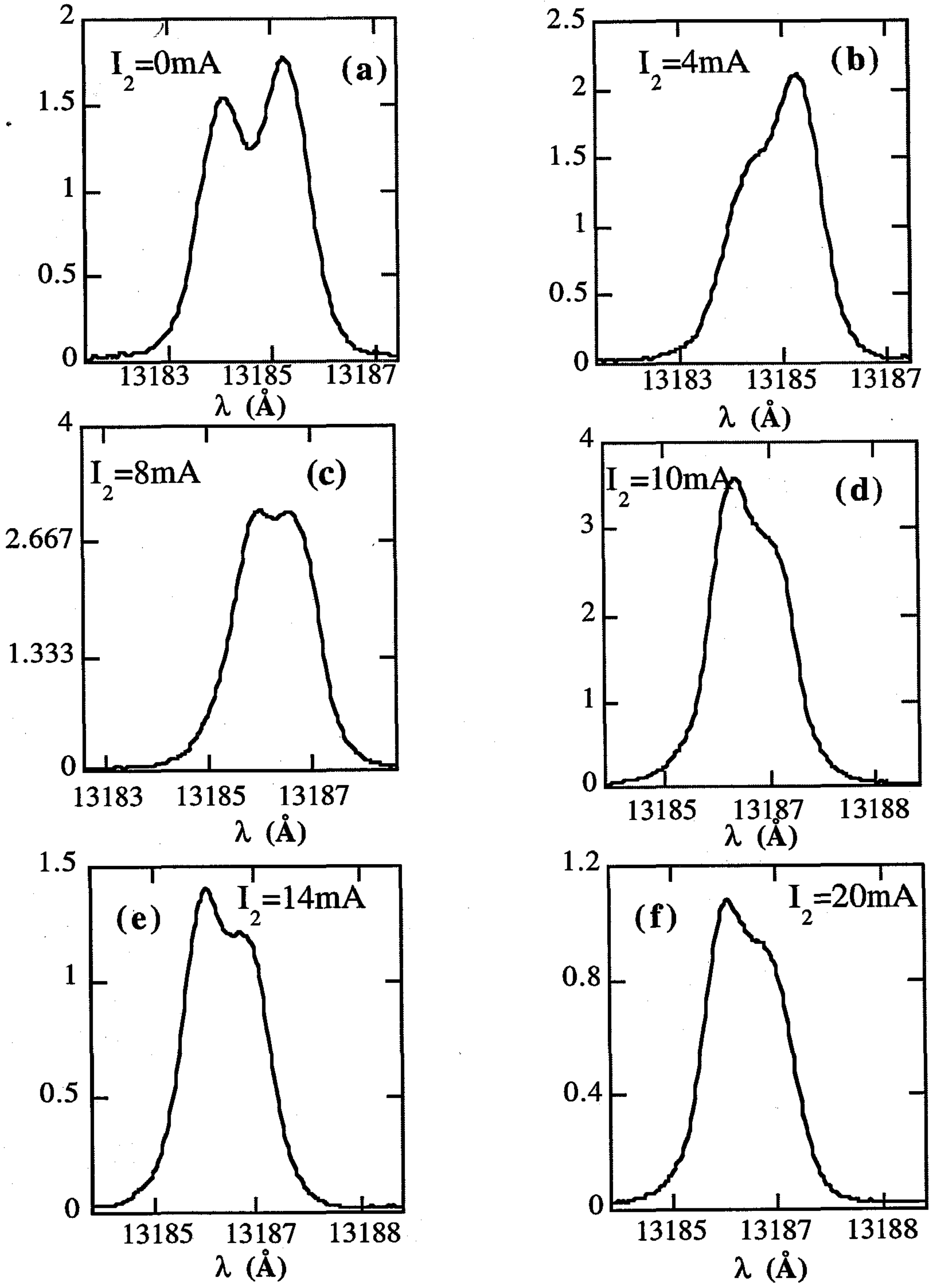
(a)
I_2=0mA
2
1.5
1
0.5
0
13183
13185
13187
λ (Å)
(b)
I_2=4mA
2.5
2
1.5
1
0.5
0
13183
13185
13187
λ (Å)
(c)
I_2=8mA
4
2.667
1.333
0
13183
13185
13187
λ (Å)
(d)
I_2=10mA
4
3
2
1
0
13185
13187
13188
λ (Å)
(e)
I_2=14mA
1.5
1
0.5
0
13185
13187
13188
λ (Å)
(f)
I_2=20mA
1.2
0.8
0.4
0
13185
13187
13188
λ (Å)

Figure 5.16: The measured time-averaged optical power spectrum of a two-section DFB laser at 5 GHz modulation for various injection current distributions. The optical modulation index M=100%, and average optical power is kept at the same level.

The spectrum of the laser is measured for various I_2, the injection current into section two. The results are shown in Fig. 5.16 (a)-(f). For low injection current I_2 (Fig. 5.16(a),(b)), the spectrum is similar to those of single section DFB lasers and is characterized by a predominantly negative chirp. As the I_2 increases to $I_2=8mA$, the spectrum becomes nearly symmetrical about the lasing frequency (Fig. 5.16(c)), and for I_2 larger than 10mA, the laser is mostly positively chirped (Fig. 5.16(d)-(f)).

The field spectrum of the current modulated laser can be calculated and it is a combination of AM and FM modulations. The time-averaged power spectrum is proportional to the spectral density of the laser field *E(t)*, which is given by [29-30]

$$S_E(\omega) = \frac{1}{\pi} \int_{-\infty}^{\infty} C_E(\tau)\, e^{-i\omega\tau}\, d\tau \tag{5.50}$$

and autocorrelation function is written as

$$C_E(\tau) = \lim_{T\to\infty} \frac{1}{T} \int_{-T/2}^{T/2} \frac{<E^*(t+\tau)\, E(t)+c.c.>}{4}\, dt \tag{5.51}$$

The optical field *E(t)* can be represented as

$$E(t) = E_0[1+m\,Sin\{(\omega_m t)+\theta_1\}]^{1/2}\bullet exp[i\{\omega_l t-\beta\,Cos(\omega_m t+\theta_2)\}]. \qquad (5.52)$$

Here m is the intensity modulation index, β is the phase modulation index, and ω_l is the lasing frequency without modulation. We write the AM and FM or frequency chirp as

$$p(t)= m\,Sin(\omega_m t+\theta_1), \qquad (5.53)$$

$$\omega(t)-\omega_l = \beta\omega_m Sin(\omega_m t+\theta_2). \qquad (5.54)$$

Combining (5.50), (5.51) with (5.52), the $S_E(\omega)$ can be calculated for several values of θ_2-θ_1 and is shown in Fig. 5.17. The $S_E(\omega)$ has a negative chirp for $\theta_2-\theta_1 \approx \pi$, and a positive chirp for $\theta_2-\theta_1 \approx 0$. This is consistent with the FM spectrum of small signal modulation derived previously [31]. In the case of small signal modulation ($m \ll 1$), the $S_E(\omega)$ is symmetrical when $\theta_2-\theta_1 = \pi/2$. However, we found that the symmetry of the $S_E(\omega)$ occurs when $\theta_2-\theta_1$ is somewhere between $\pi/2$ and π, depending on the intensity modulation index m and phase modulation index β.

The instantaneous frequency deviation $\delta\omega(t)$ is calculated from (5.41) and AM modulation can be got from (5.32). The phase difference between FM and AM, $\theta_2-\theta_1$, can be obtained. For small I_2, the injected current in section two, $\theta_2-\theta_1$, is approximately equal to π, which gives the red-shifted spectrum (as shown in Fig. 5.17b), and is consistent with the observed spectrum of small I_2 (Fig. 5.16(a),(b)). The value of $\theta_2-\theta_1$ sharply decreases to zero for I_2 >10 mA, which results in the blue-shifted spectrum at large I_2 (Fig. 5.16(d)-(f)). The calculated $\theta_2-\theta_1$ is shown in Fig. 5.19.

The frequency deviation $\delta\omega(t)$ involves, according to (5.41), a spatial integration of the imaginary part of $C_N(z)$ and $N_1(z)$, the AC component of local carrier density. The z-dependent $N_1(z)$ and $Im\{C_N(z)\}$ in DFB lasers determine the phase of $\delta\omega(t)$. In the two-section DFB laser, by adjusting the injection current distribution, distributions $N_0(z)$, $S_0(z)$, the function $C_N(z)$, and $N_1(z)$ can be controlled. This results in a control of the phase difference $\theta_2-\theta_1$ and thus the characteristics of the frequency chirp. Qualitatively, when the photon density in section one is much smaller than that in section two (Fig. 5.18b), $N_1(z)$ is in phase with the modulation current in the longer section (section one) where the injected modulation current is the dominant contribution. This, according to (5.41), results in a positive chirp (Fig. 5.18b). Our calculation also shows that in most of single section DFB lasers, the phase difference $\theta_2-\theta_1$ is close to π, which according to the above analysis, results in a red-shifted chirp consistent with the observed spectra of single section DFB lasers[2-3].

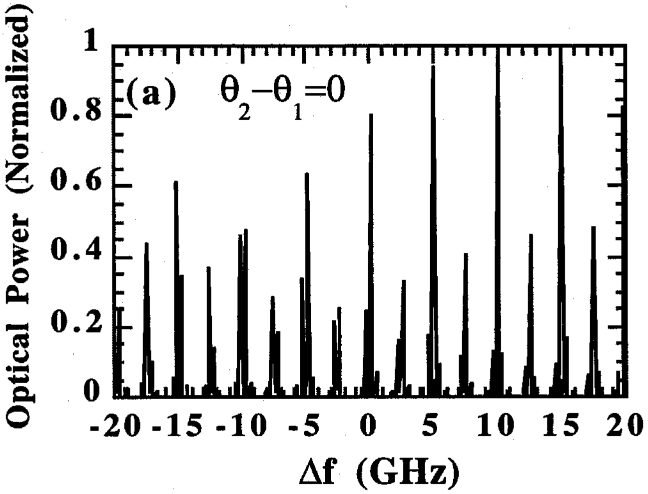

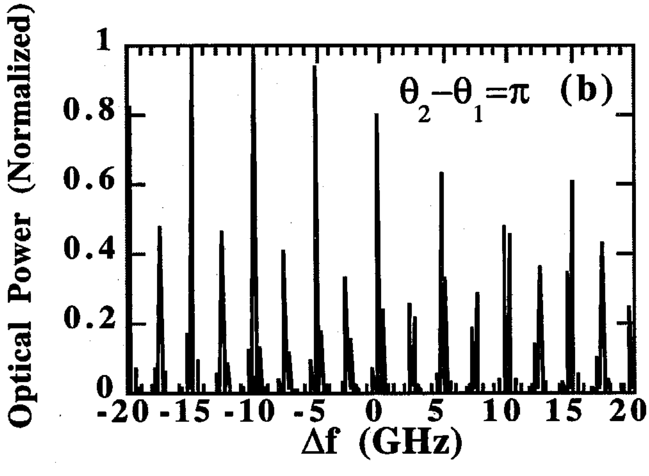

Figure 5.17: The calculated spectral density of the optical field of a single mode laser under 5 GHz modulation. The intensity modulation index and phase modulation index are set at $m=1$, $\beta=3$.

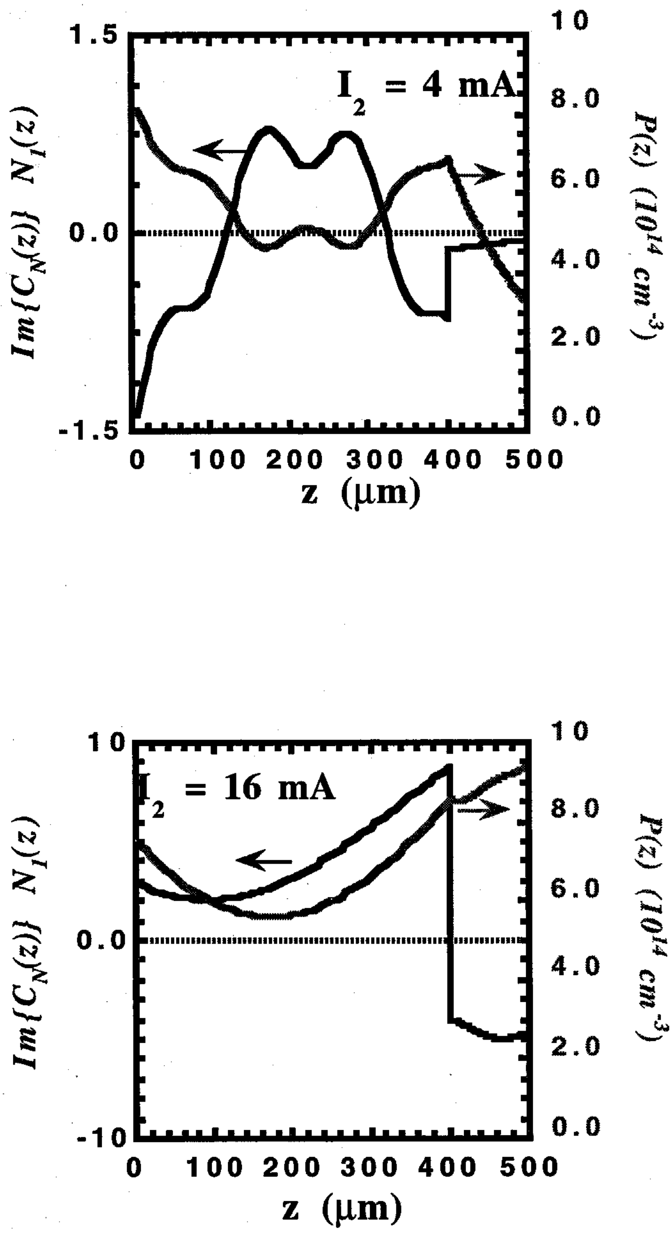

Figure 5.18: Calculated photon density and the product of $N_1(z)$ and $Im\{C_N(z)\}$ in the two-section DFB laser for injection current in section two as (a) $I_2=4\ mA$, (b) $I_2=16mA$.

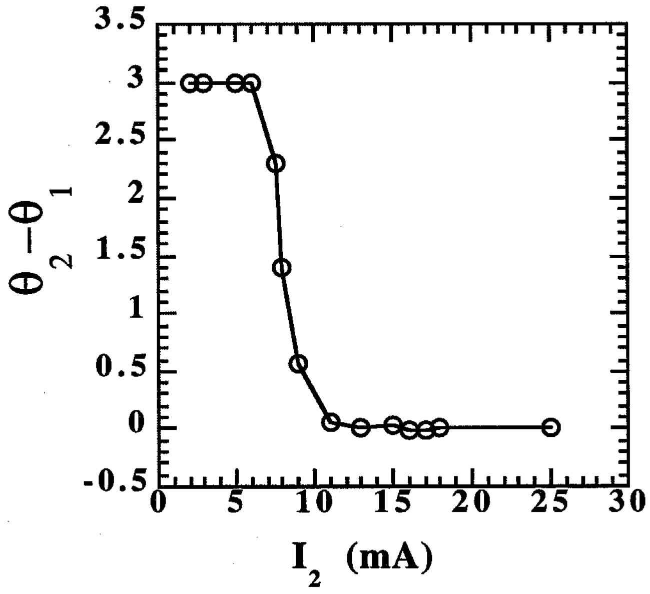

Figure 5.19: Calculated phase difference $\theta_2 - \theta_1$ of the directly modulated two-section DFB laser used in the experiment for various I_2, the injection current into the section two.

5.8 Conclusion

In this chapter, we have demonstrated chirp reduction and chirp control in DFB lasers by controlling the longitudinal distribution of the photon density. This changes the dynamics of spatial hole burning, and consequently, laser chirp. The expression for chirp in DFB lasers has been derived based on the rate equations with considering the LSHB. The nonuniform photon and carrier density distributions have been obtained from the coupled-mode equations by using the Green's function method. The relation between the phase and intensity of the lasing mode involves not only the α parameter, but also the distribution of electric traveling fields in the DFB laser. It is found that, unlike the case of a single section laser, the measured chirp does not depend directly on the α parameter but rather on the traveling field distributions in multisection DFB lasers. This is very different from the case of chirp in uniform photon density lasers. By fabricating two-section DFB lasers and changing the injection current into the two sections independently, we can adjust the photon density distribution and change the chirp characteristics. The reduction of the chirp by a factor of ten has been realized, and we also achieved blue-shift optical signals from the two-section DFB laser under direct current modulation. The unique advantage for using two-section DFB lasers is that frequency chirp can be reduced even when spatial hole burning is not suppressed.

References

[1] K. Lau, C. Harder, and A. Yariv, *IEEE J. Quantum Electron.,* **QE-20**, 71 (1984)

[2] Y. Yoshikuni, T. Matsuoka, G. Motosugi, and N. Yamanaka, *Appl. Phys. Lett.* 45, 820 (1984)

[3] C. Lin, G. Eisenstein, C.A. Burrus, and R.S. Tucker, *Appl. Phys. Lett.* 46, 12 (1985)

[4] K. Kishino, S. Aoki, and Y. Suematsu, *IEEE J. Quantum Electron.,* **QE-18**, 343 (1982)

[5] G.P. Agrawal, *IEEE J. Quantum Electron.,* **QE-21**, 680 (1985)

[6] T. L. Koch and R. A. Linke, *Appl. Phys. Lett.* 48, 613 (1986)

[7] T. L. Koch, and J.E. Bower, *Electron. Lett.* 20, 1038 (1984)

[8] J. I. Kinoshita, and K. Matsumoto, *IEEE J. Quantum Electron.,***QE-24**, 2160 (1988)

[9] H. Soda, Y. Kotaki, H. Sudo, H. Ishikawa, S. Yamakoshi, and H. Imai, *IEEE J. Quantum Electron.*, **QE-23**, 804 (1987)

[10] K. Uomi, S. Sasaki, T. Tsuchiya, H. Nakano, and N. Chinone, *IEEE Phot. Tech. Lett.* 2, 229 (1990)

[11] S. Kakimoto, Y. Nakajima, Y. Sakakibara, H. Watanabe, A. Takemoto, and N. Yoshida, *IEEE J. Quantum Electron.,* **QE-26**, 1460 (1990)

[12] Y. Luo, R. Takahashi, Y. Nakano, K. Tada, T. Kamiya, H. Hosomatsu, and H. Iwaoka, *Appl. Phys. Lett.* , 59, 307 (1991)

[13] J. Feng, T.R. Chen, and A. Yariv (to be published)

[14] J. Feng, T.R. Chen, B. Zhao, and A. Yariv, *Appl. Phys. Lett.* 66, 2028 (1995)

[15] J. Feng, T.R. Chen, and A. Yariv, *Appl. Phys. Lett.* 67, 2913 (1995)

[16] P. Anderson, and T. Anderson, *IEEE J. Lightwave Technol.* **LT-4**, 795 (1986)

[17] B. Tromborg, H. Oslesen, and X. Pan, *IEEE J. Quantum Electron.,* **QE-27**, 178 (1991)

[18] T. Schrans, *Ph.D. Thesis, California Institute of Technology*, Pasadena, Calif., 1994

[19] W. Length, *IEEE J. Quantum Electron.,* **QE-20**, 1045 (1984)

[20] J.J.M. Iannelli, T. Schrans, T.R. Chen, Y.H. Zhuang, and A. Yariv, *Appl. Phys. Lett.* 63, 1468 (1993)

[21] R. Schimpe, J. E. Bowers, and T. L. Koch, *Electron. Lett.* 22, 453 (1986)

[22] K. Petermann, *Laser Diode Modulation and Noise* (Kluwer Academic, Dordrecht, The Netherlands, 1991), p. 121

[23] L.M. Zhang, and J.E. Carroll, *IEEE J. Quantum Electron.,* **QE-28**, 604 (1992)

[24] N. Nakamara, K. Aiki, J. Umeda, A. Yariv, H. W. Yen, and T. Morikawa, *Appl. Phys. Lett.* 25, 487 (1974)

[25] M. Yamada, and K. Sakuda, *Appl. Opt.* 26, 3474 (1987)

[25] M. Kuznetsov, A. E. Willner, and I. P. Kaminow, *Appl. Phys. Lett.* 55, 1826 (1989)

[26] T.L. Koch, and R.C. Alferness, *IEEE J. Lightwave Technol.* **LT-3**, 800 (1985)

[27] N. Henmi, T. Saito, and T. Ishida, *IEEE J. Lightwave Technol.* **LT-10**, 1706 (1994)

[28] T. Morioka, and M. Saruwatari, *Electron. Lett.* 25, 646 (1989)

[29] A. Yariv, *Optical Electronics, 4th Editon* (Holt, Rinehart and Winton, New York, 1991), p. 380-382

[30] G.P. Agrawal, *IEEE J. Quantum Electron.,* **QE-21**, 680 (1985)

[31] S. Kobayashi, Y. Yamammoto, M. Ito, and T. Kimura, *IEEE J. Quantum Electron.,* **QE-18**, 582 (1982)

Chapter 6

Spectral Dynamics and High Speed Performance of Uncooled Distributed Feedback Lasers

6.1 Introduction

In most of the present laser transmitters, thermoelectric coolers are required to keep the laser operating temperature constant. The thermoelectric cooler adds to the costs of the transmitter, and its long-term reliability is also a concern. Uncooled laser transmitters are cheaper and more reliable than thermoelectric cooled laser transmitters because of their simplicities in laser packaging. It is desirable to have uncooled semiconductor lasers that can perform well in an extreme temperature environment. Extensive research efforts [1-10] have been made to improve the temperature characteristics of lasers, and there are a lot of progresses in achieving high temperature operation and small deteriorating external differential quantum efficiency over extensive temperature range. It is believed that the poor temperature characteristics of conventional lasers are partly due to Auger recombination [11] in the low bandgap material and partly due to poor electron confinement resulting from the small conduction band offset ($\Delta E_c = 0.4\ \Delta E_g$) of the InGaAsP/InP lasers [1]. It had been proposed that the laser threshold, Auger recombination, and intervalence band absorption can be reduced by using the combination of biaxial strain and quantum confinement to reduce the in-plane hole effective mass [12-13]. The $Al_xGa_yIn_{1-x-y}As$/InP material system, for its large conduction band offset ($\Delta E_c = 0.72\ \Delta E_g$) [14-15], has been chosen to provide a strong electron confinement. The design of high temperature lasers in terms of the quantum well number and mirror loss is quite different from that of low threshold current lasers [1,16]. To avoid gain saturation at high temperature operation, the optimum operating point should be designed by using the gain curve of the highest operating temperature at the expense of a slightly high threshold current at room temperature.

For both analog CATV applications and long haul, high speed digital communications, uncooled SLM DFB lasers are very attractive because of their low costs. However, most research efforts now have been devoted to uncooled Fabry-Perot (FP) lasers. In this chapter, we intend to investigate the high temperature performance of single mode distributed feedback (DFB) lasers. The methods are basically the same on minimizing the change of threshold current and slope efficiency both in uncooled FP lasers and in uncooled DFB lasers. Additionally for uncooled SLM DFB lasers, it is essential to maintain single mode operation and good SMSR at high temperatures.

In this chapter, we first review the gain profile of semiconductor materials at high temperature and DC characteristics (such as threshold current and external differential quantum efficiency) of uncooled DFB lasers. Then we are going to give our studies on the spectral dynamics and high speed response of uncooled DFB lasers with wavelength detune (e.g., the lasing wavelength is different from that at the gain peak). In wavelength-detune uncooled DFB lasers, the gain is not as a linear function of the injected carrier density as that in FP lasers, which lase at the gain peak. The gain, as a function of injected carrier density, has to be numerically calculated for certain wavelength detune. DFB lasers with negative wavelength detunes, which lase at the short wavelength away from the gain peak, have relatively larger differential gain. The lasers with negative wavelength detunes have smaller linewidth enhancement factors and better high speed responses than those lasers without wavelength detune. But the negative wavelength-detune DFB lasers have slightly higher threshold currents. Also, we will show that the high speed response of the DFB lasers with large negative detune deteriorates faster over high temperature. To achieve best performance of uncooled DFB lasers, it is necessary to design wavelength detune carefully for specific applications.

6.2 Gain spectrum

6.2.1 Gain expression

The temperature dependence of the band gap of 1.3μm InGaAsP lattice-matched to InP has been obtained from measurements of the wavelength of InGaAsP/InP lasers. $E_g(T)$ is an almost linear function of temperature and is given by the experimental relation [17]

$$E_g(T) = E_g^0 - 3.6*10^{-4}(T - 300) \quad (eV) \tag{6.1}$$

Here E_g^0 is the bandgap energy at 300°K.

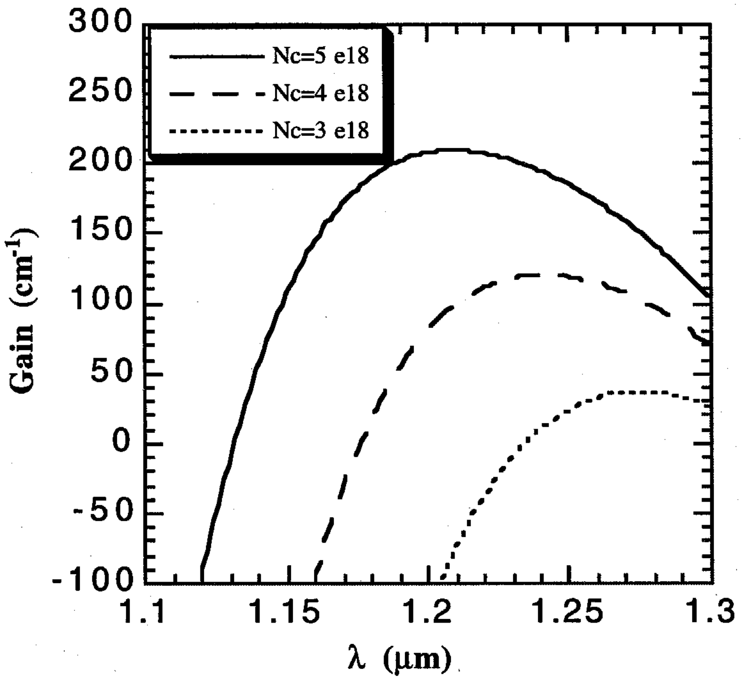

Figure 6.1: Optical gain of 1.3 InGaAsP material as function of wavelength for various carrier densities.

The modal gain is given by [18]

$$g(E,N)=-\Gamma\frac{2\pi}{\lambda_0 n}\sum_{i=l,h}\int A_i(E)\rho_i^r(E)(f_e+f_h-1)\frac{\hbar/\tau}{(\hbar/\tau)^2+(E-E)^2}dE \tag{6.2}$$

E is the photon energy, τ is the collisional dephasing time, and ρ is the density of states function. $A(E)$ includes the transition dipole moment and the polarization modification factor for the dipole moment in the QW structure. f_e and f_h are quasi-Fermi distribution functions for electrons and holes, which are given as

$$f_e=\frac{1}{exp\left(\frac{E_e-E_F^e}{kT}\right)+1} \tag{6.3a}$$

$$f_h=\frac{1}{exp\left(\frac{E_h-E_F^h}{kT}\right)+1} \tag{6.3b}$$

where E_F^e, E_F^h are the quasi-Fermi energy levels for electrons and holes, respectively.

Typical gain curves for three different injected carrier densities are shown in Fig. 6.1. From numerical calculation of the optical gain (6.2), the peak gain is found to vary almost linearly with the injected carrier density, and can be approximately expressed by

$$g^{peak}(N,T) = A(T)\,[N- N_{tr}(T)] \tag{6.4}$$

where A is the differential gain, and N_{tr} is the transparency carrier density. A and N_{tr} are temperature dependent. The gain expression (6.4) has been used extensively in FP lasers. However, if the lasing wavelength of a DFB laser is detuned from that of gain peak, we have to use (6.2) to calculate the gain at the detuned wavelength, and the gain can not be described by (6.4) [19].

6.2.2 Collisional dephasing time

It can be seen that the collisional dephasing time τ is important to determine the gain profile. Theoretical calculations show that major mechanisms contributing to the collisional dephasing rate are: carrier-carrier scattering [20], carrier phonon scattering [21], and alloy scattering [22], and their temperature dependencies have been well known. It is difficult to predict theoretically the temperature dependence of τ since the three major mechanisms have comparable magnitude in the temperature range of our interest. The temperature dependence of τ has been measured through measuring photoluminescence spectrum and comparing it with the theoretically calculated spectrum. The experimental temperature dependence of τ has the following formula [23]:

$$\tau(T) = \tau_0\left[1+\beta\left(\frac{T-T_0}{T_1-T_0}\right)\right]^{-1} \tag{6.5}$$

where τ_0, β, T_0 and T_1 have to be determined through experiment.

Quasi-Fermi level E_F^e, E_F^h do not change much as temperature changes from 20°C to 120°C, so carriers spread over a larger energy range in conduction and valence bands as we can see from quasi-Fermi distributions (6.3). The gain curves over different temperatures have been calculated in Fig. 6.2. At the same injected carrier density, gain becomes smaller at high temperature. Decrease of $\tau(T)$ at high temperature makes $g(\lambda)$ broader and reduces its peak height (Fig. 6.2). That gain peak moves to long wavelength at high temperature is due to the reduction of bandgap energy according to (6.1).

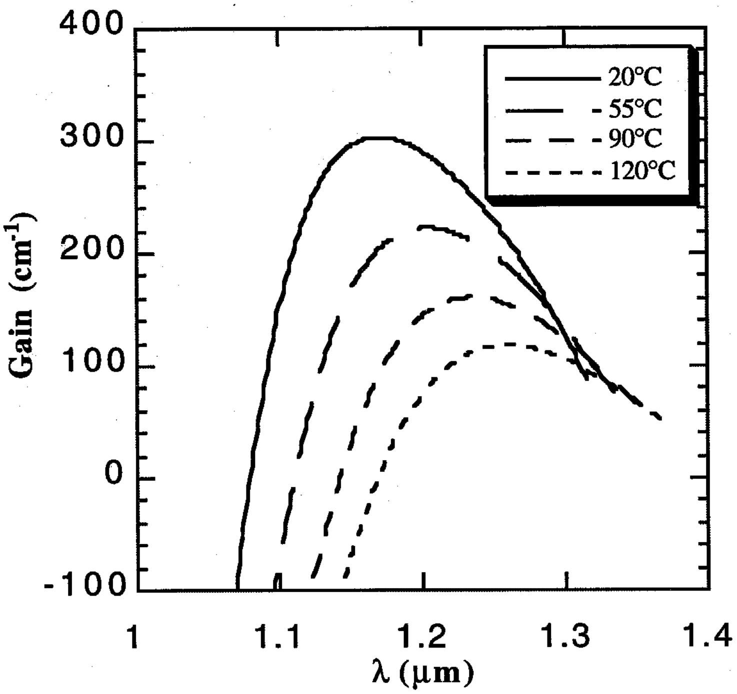

Figure 6.2: The calculated optical gain of 1.3 InGaAsP material as function of wavelength at various temperatures for carrier density $N_c=6x10^{18}cm^{-3}$.

6.2.3 Gain spectrum in detuned DFB lasers

In FP lasers, the oscillation wavelength is around the peak of the gain curve. Accordingly, the peak gain (6.4) is considered to describe laser characteristics, and the differential gain A is one of the important factors determining high speed performance of the lasers. In DFB lasers, the lasing wavelength is mainly determined by the grating pitch. Normally, the Bragg wavelength of a DFB laser sets at a shorter wavelength than that of the gain peak

[19]. The laser is also referred to as negatively detuned. In a detuned DFB laser, the gain as a function of injection carrier density has to be numerically calculated. The gain as a function of injected carrier density is shown in Fig. 6.3 for various detuned wavelengths. In comparison, the peak gain is also plotted. Because the gain distribution (Fig. 6.1) moves to the shorter wavelength as the injection carrier density increases, the differential gain is larger at the wavelength which is shorter than that at the gain peak (Fig. 6.1 and Fig. 6.3). Therefore, the negatively detuned DFB lasers are expected to result in a higher resonance frequency through the increase in differential gain.

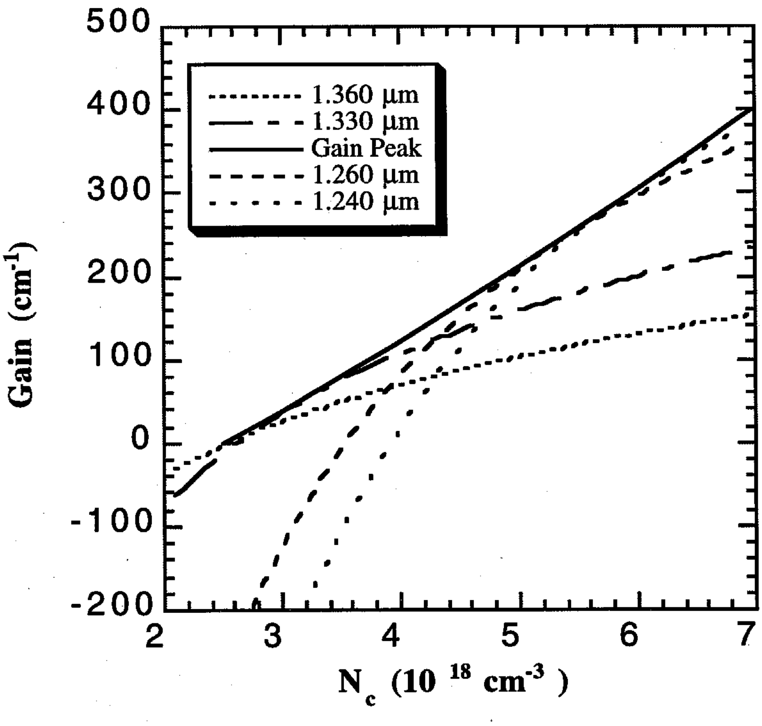

Figure 6.3: Calculated gain of 1.3µm InGaAsP material as function of injection carrier density for various wavelength detunes.

6.3 DC characteristics of uncooled DFB lasers

High temperature performance of uncooled lasers suffers from Auger recombination in the low bandage materials and poor electron confinement resulting in the small conduction band offset ($\Delta E_c=0.4\Delta E_g$ for $Ga_xIn_{1-x}As_yP_{1-y}/InP$ materials). The increase of intervalence absorption reduces the external differential quantum efficiency.

6.3.1 Threshold current density

The threshold current density in typical long wavelength lasers is taken as [11]

$$J_{th} = An_{th}+Bn_{th}^2 +Cn_{th}^3 \tag{6.6}$$

where the first term is the monomolecular nonradiative recombination, and the second term is the bimolecular radiative current density. The third term is the Auger recombination in which an electron and a hole recombine across the bandgap and, instead of emitting a photon, they excite a third carrier into the valence or conduction band. The recombination coefficients themselves, *A*, *B* and *C*, also have a temperature dependence.

We assume that Auger is an activated process and the Auger recombination coefficient is given by [24]

$$C = C_0 \, exp(-E_a/kT) \tag{6.7}$$

where E_a is the Auger activation energy, which is determined by the band structure.

The radiative recombination coefficient, B, is assumed to vary with temperature as for an ideal QW with [25]

$$B \propto \frac{1}{T} \tag{6.8}$$

The threshold carrier density, $n_{th} \propto T$, for an ideal QW laser. However, the temperature dependence of the threshold carrier density is taken as [26]

$$n_{th} \propto T^{1+x} \tag{6.9}$$

due to nonideal factors such as carriers occupying higher subbands, carrier spillover into the barrier material, or intervalence band absorption, which all may increase the temperature sensitivity of the threshold beyond linearity.

It has been shown that the monomolecular nonradiative processes depend weakly on the temperature, and therefore it is ignored.

The temperature dependence of a semiconductor laser is usually described by the T_0 parameter, which is given by the experimental relation

$$T_0 = \frac{d[ln(J_{th})]}{dT} \tag{6.10}$$

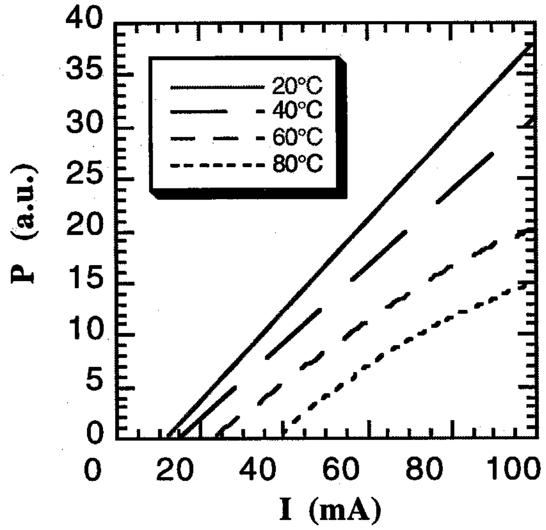

Figure 6.4: Measured L-I of 1.3μm InGaAsP/InP QW DFB lasers at various temperatures.

6.3.2 Carrier leakage in quantum well lasers

Taking into account Auger recombination in the active region, free-carrier absorption in the active region and waveguide, and current leakage to the cladding barrier, total current through a laser includes the following components [27]:

$$J_{total}=J_{active}+J_{wg}+J_{Auger}+J_{leakage}=J_{majority}+J_{leakage} \tag{6.11}$$

where J_{active} and J_{wg} represent radiative recombination current in the active region and waveguide, respectively. J_{Auger} is nonradiative Auger recombination current in the active region and $J_{leakage}$ is a current of minority carrier overflowing from the waveguide to the cladding layer. $J_{leakage}$ is essentially a current of electrons leaking to the *p*-cladding layer and eventually recombining on the boundary with the highly doped p-contact layer. A higher effective mass of holes results in a quasi-Fermi level position close to the valence band edge of the active layer, and hole leakage current may be effectively neglected. The first three terms in (6.11) are calculated according to standard theory to give $J_{majority}$. The analytical approximation for leakage current can be obtained by analytically solving the diffusion-drift equation while assuming constant electric field [27-28]

$$J_{leakage} = qD_n n \left[\sqrt{\frac{1}{L}+\left(\frac{kT}{2qE_0}\right)^2}\, coth\sqrt{\frac{1}{L}+\left(\frac{kT}{2qE_0}\right)^2}+\frac{kT}{2qE_0}\right] \tag{6.12}$$

where

$$E_0 \approx \frac{1}{q\mu_p P_0}\left(J_{majority}+\frac{D_p}{D_n}J_{leakage}\right) \tag{6.13}$$

6.3.3 Internal loss in quantum well lasers

Applying the linear relationship between the internal loss of the QW and temperature, we have [29]

$$\alpha_i^{QW}=\alpha_1+\gamma(T-T_1) \tag{6.14}$$

where

$$\gamma=d\alpha_i^{QW}/dT \tag{6.15}$$

The total internal loss is

$$\alpha_1=N^{QW}\alpha_i^{QW}+\alpha_i^{SCH} \tag{6.16}$$

6.3.4 External differential quantum efficiency

The power emitted by stimulated emission is expressed by [30]

$$P_e = \frac{(I - I_{th})\eta_i}{e} h\nu \tag{6.17}$$

The external differential quantum efficiency is defined as the ratio of the photon output rate that results from an increase in the injection rate to the increase in the injection rate

$$\eta_{ex} = \frac{d(P_0/h\nu)}{d[(I - I_{th})/e]} \tag{6.18}$$

In DFB lasers, the external differential quantum efficiency can be derived from the measured or calculated L-I characteristics. A simplified expression for η_{ex} can be obtained by writing the threshold gain for DFB lasers as

$$g_{th} = \alpha_m + \alpha_i \tag{6.19}$$

with α_i as the internal loss and α_m as the so-called cavity loss accounting for the power leaving the DFB laser cavity. α_m may be obtained from numerical calculation of the threshold gain in DFB lasers [31-34]. For a typical DFB laser with $\kappa L=2$, we have

$$\alpha_m L \approx 1.95 \tag{6.20}$$

In order to compare this cavity loss with the mirror of an FP laser, α_m is found by recalling the expression for g_{th} in the FP laser

$$\alpha_m = 1/2L \ \ln(1/R_1R_2) \tag{6.21}$$

In this sense, the cavity loss $\alpha_m L$ may be related to an effective reflectivity $R=0.14$ (for $R=R_1=R_2$).

With considering leakage current, we write the output power of a DFB laser as

$$P_o=\frac{(I-I_{th}-I_{leakage})\eta_i h\nu}{e}\,\frac{\alpha_m}{\alpha_m+\alpha_i} \tag{6.22}$$

and the external differential quantum efficiency is

$$\eta_{ex}=(\eta_i-\frac{dI_{leakage}}{dI})\,\frac{\alpha_m}{\alpha_m+\alpha_i} \tag{6.23}$$

With (6.16), the temperature dependence of η_{ex} can be obtained as

$$\eta_{ex}(T)=(\eta_i-\frac{d[I_{leakage}(T)]}{dI})\,\frac{\alpha_m(T)}{\alpha_m(T)+N^{QW}[\alpha_1+\gamma(T-T_1)]+\alpha_i^{SCH}} \tag{6.24}$$

where η_i is the internal quantum efficiency, and it shows little temperature dependence in the temperature range of our interest.

6.4 Gain spectrum of uncooled DFB laser

Several 1.3μm InGaAsP/InP strained quantum well (QW) DFB lasers have been fabricated. The lasers are AR (<5%) coated at front facets and HR (>70%) coated at back facets. AR/HR coating is essential for the DFB lasers to maintain SLM operation at high temperatures. This is specially important for wavelength-detune DFB lasers. The wavelength-detune DFB lasers lase away from the gain peak, and at high temperatures the FP modes are normally much stronger than the main mode of the DFB lasers if the front facet is not appropriately AR coated. AR/HR coating will suppress the FP modes to keep the SLM operation of DFB lasers. The spectrum of a 1.3μm InGaAsP/InP QW DFB laser has been measured at various temperatures (Fig. 6.5-Fig. 6.8). The laser is negatively detuned and the wavelength detune is $\Delta\lambda_D=\lambda_{lase}-\lambda_{gain\ peak}\approx$ 10nm at room temperature. It can be seen from Fig. 6.5-Fig. 6.8 that the laser keeps its SLM to 80°C. The lasing wavelength of the laser is 1290 nm at room temperature and only increases to 1295 nm at 80°C.

6.4.1 The measurement of gain spectrum

The gain spectra can be calculated by measuring the FP mode spectra below threshold bias current. We show here the spectrum (Fig. 6.9 and Fig. 6.10) of the DFB laser for I=9.5 mA (below threshold) at room temperature, and the threshold current is about 10.6 mA. The modal gain of lasers can be calculated from modulation depth of the measured spectra, which is given by Hakki and Paoli as [35]

$$g(E)=\frac{1}{L}\,ln\left(\frac{1}{\sqrt{R_1R_2}}\frac{\sqrt{V}-1}{\sqrt{V}+1}\right)+\alpha_{loss} \tag{6.25}$$

$$V=\frac{P_{max}}{P_{min}} \tag{6.26}$$

where R_1 and R_2 are the respective reflectivities of the front and rear facets. The P_{max} and P_{min} donate the FP peaks and valleys. When the gain spectra are estimated from the measured spectra by using (6.6), the results are shown in Fig. 6.11-Fig. 6.14. The calculated gain from spectra is not accurate at the wavelength around the Bragg condition due to the influence of the corrugation grating in the lasers.

From Fig. 6.11-Fig. 6.14, we get the wavelength detune of the DFB laser at various temperatures, which is shown in Fig. 6.15. It can be seen that the detune increases greatly with temperature. The increase of the wavelength detune is largely due to the shift of the gain peak. The gain peak moves to long wavelength as we increase the substrate temperature of the laser (Fig. 6.11-Fig. 6.14).

6.4.2 The influence of the corrugation grating on the measured gain spectra

In measuring the DFB laser gain spectra below threshold, the corrugation grating, formed within the laser cavity, has effects on the FP mode spectra. The gain spectra we calculated from (6.25) are only valid for the FP mode spectra. The gain spectra (Fig. 6.11-Fig. 6.14) are a combination of the FP spectra and additional loss generated by the grating. Using F-matrix [36] method, the loss due to the grating can be numerically calculated. Fig. 6.16 shows the gain deviation of the estimated normalized gain as a function of normalized deviation. The normalized gain deviation is defined as [37]

$$\Delta\tilde{G} = \frac{G_{DFB} - G_{FP}}{G_{FP}} \tag{6.27}$$

where G_{DFB} and G_{FP} denote the modal gains for DFB and FP lasers and are given by

$$G_{DFB} = \Gamma g_{material} - \alpha_{loss} - \alpha_{grating} \tag{6.28}$$

$$G_{FP} = \Gamma g_{material} - \alpha_{loss} - \alpha_{mirror} \tag{6.29}$$

The normalized deviation is given as

$$\Delta\beta = \beta - \beta_{Bragg} \tag{6.30}$$

where β is the propagation constant at reference wavelength λ and β_{Bragg} is the propagation constant at the Bragg wavelength.

The gain deviation is large when the normalized deviation is close to zero, e.g., the reference wavelength is close to the lasing wavelength. This indicates that the estimated gain for the DFB laser is quite different from that for the FP laser near the Bragg wavelength and we can find that there are sharp changes around the lasing wavelength from the estimated gain spectra (Fig. 6.11-Fig. 6.14). Away from the lasing point ($|\Delta\beta L|>20$), the estimated gain is only slightly different from its accurate value.

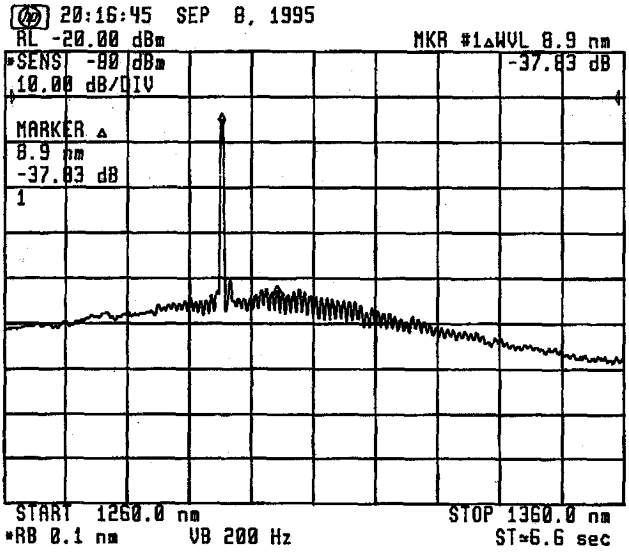

Figure 6.5: The spectrum of a 1.3μm InGaAsP/InP QW DFB laser at 20°C.

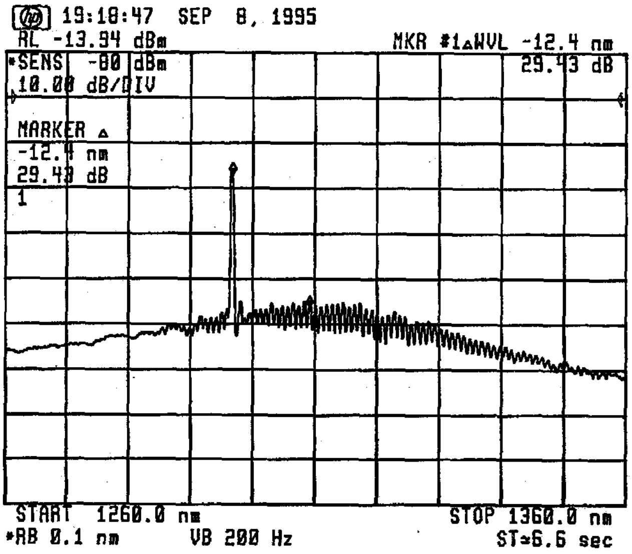

Figure 6.6: The spectrum of the DFB laser at 40°C.

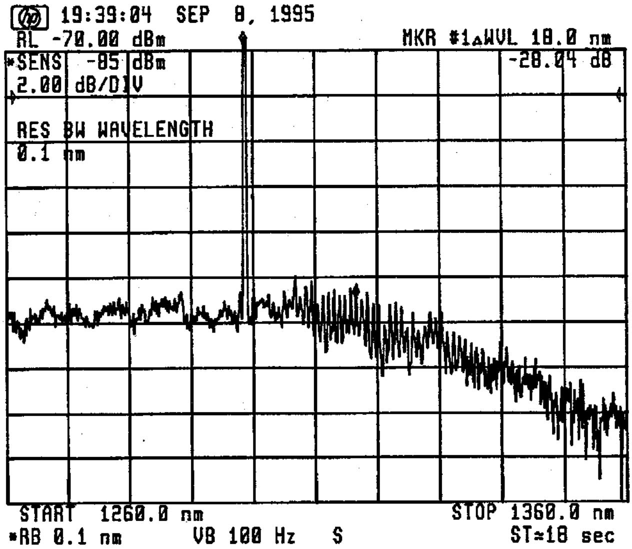

Figure 6.7: The spectrum of the DFB laser at 60°C.

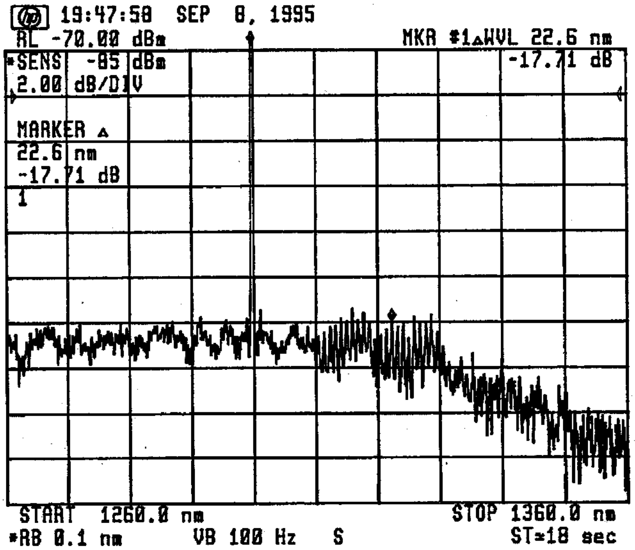

Figure 6.8: The spectrum of the DFB laser at 80°C.

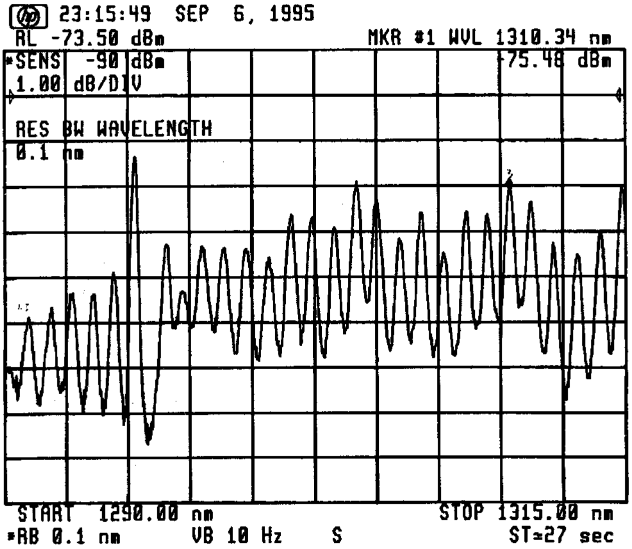

Figure 6.9: The spectrum of the DFB laser below threshold for λ=1290 nm-1315 nm.

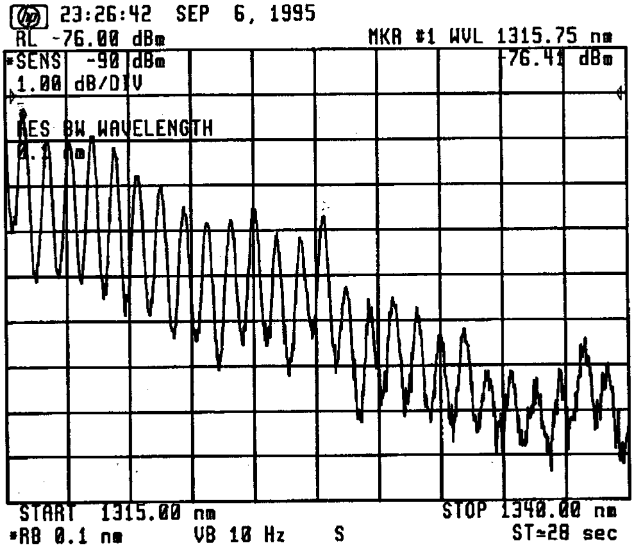

Figure 6.10: The spectrum of the DFB laser below threshold for λ=1315 nm-1340 nm.

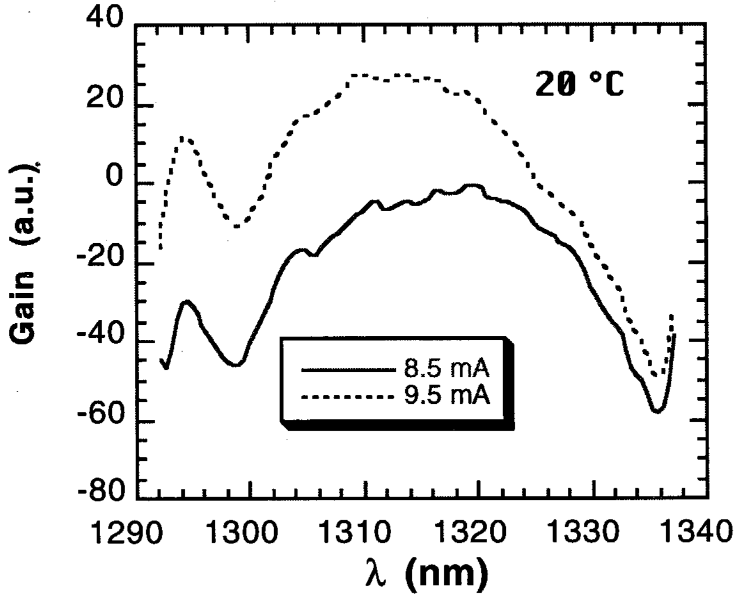

Figure 6.11: The estimated modal gain of the DFB laser at 20°C.

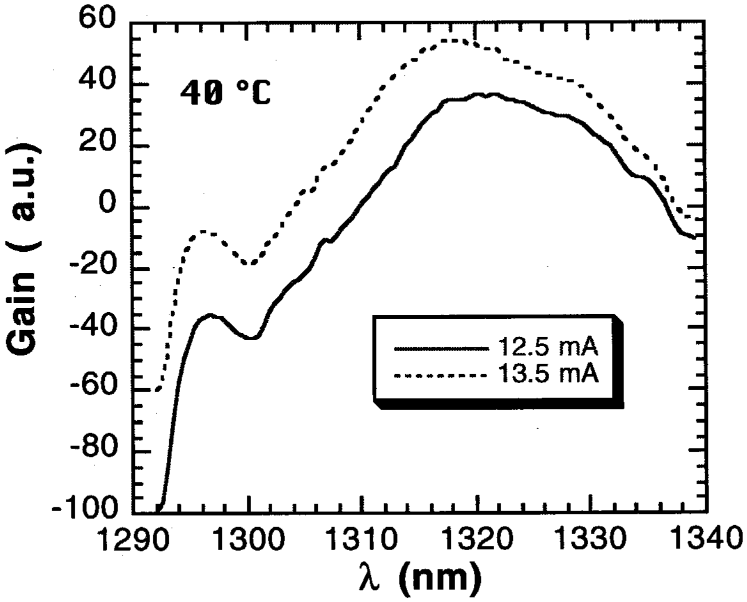

Figure 6.12: The estimated modal gain of the DFB laser at 40°C.

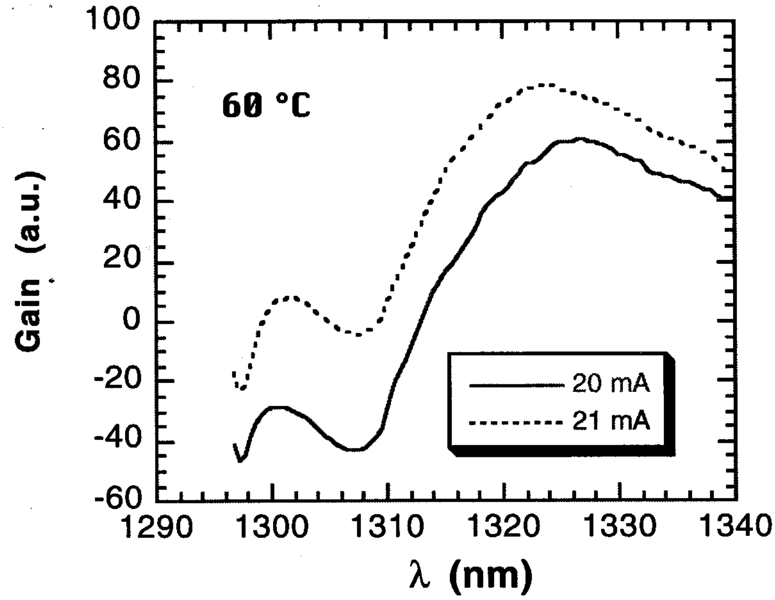

Figure 6.13: The estimated modal gain of the DFB laser at 60°C.

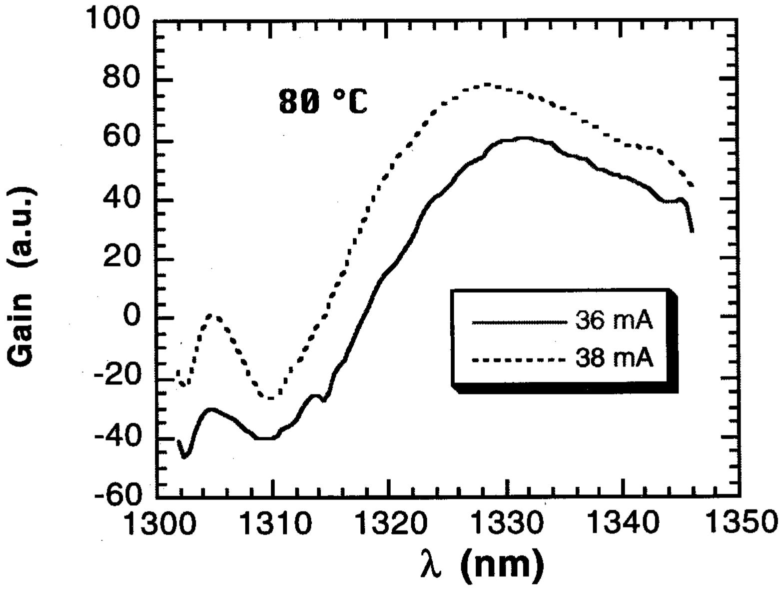

Figure 6.14: The estimated modal gain of the DFB laser at 80°C.

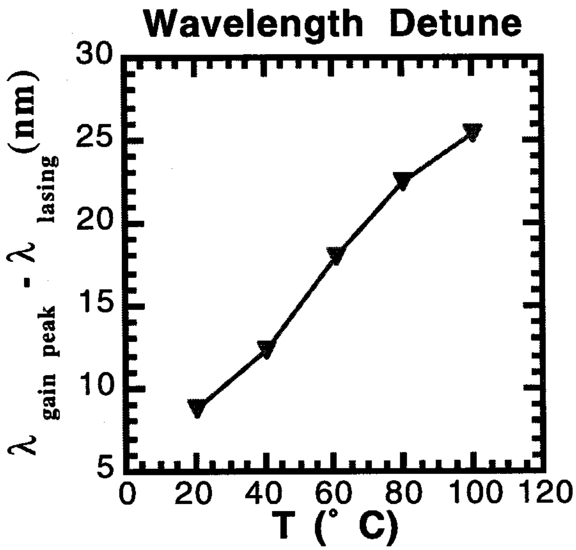

Figure 6.15: Measured wavelength detune of the 1.3μm InGaAsP/InP QW DFB laser at different temperatures.

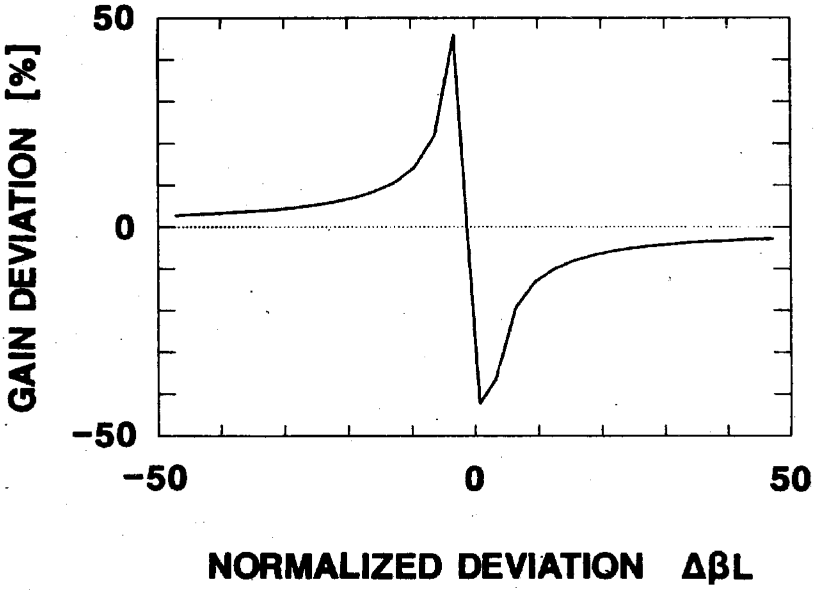

Figure 6.16: Calculated normalized gain deviation versus normalized deviation.

6.5 Linewidth enhancement factor, linewidth of uncooled DFB laser

6.5.1 Measurement of α factor

We have a direct relation (5.9) between photon density and lasing frequency [38, 39, 40]

$$\nu - \nu_{th} = \frac{\alpha}{4\pi}\left(\frac{d(lnS)}{dt} + \frac{1}{\tau_{ph}}\varepsilon S\right) \tag{6.31}$$

If a small signal sinusoidal modulation of the photon number S is assumed according to

$$S = \langle S\rangle + Re(\Delta S\ exp(i\omega_m t)\ ), \tag{6.32}$$

here $|\Delta S| \ll \langle S\rangle$ and ω_m is denoted to the modulation frequency. The frequency modulation may be written as

$$\nu = \langle \nu\rangle + Re(\Delta\nu\ exp(i\omega_m t)\ ) \tag{6.33}$$

and (6.31) yields

$$\Delta\nu/\Delta S = \frac{\alpha}{4\pi\langle S\rangle}(i\omega_m + \omega_g) \tag{6.34}$$

with

$$\omega_g = \frac{\varepsilon}{\tau_{ph}}\langle S\rangle \tag{6.35}$$

It is often more convenient to relate the FM-modulation index

$$\beta = |2\pi\Delta\nu/\omega_m| \tag{6.36}$$

to the AM-modulation index

$$m = |\Delta S / \langle S \rangle| \tag{6.37}$$

yielding

$$\frac{\beta}{m} = \frac{\alpha}{2}\sqrt{1+\left(\frac{\omega_g}{\omega_m}\right)^2} \tag{6.38}$$

In Fig. 6.17, the β/m generally decreases with increasing modulation frequency and approaches to $\alpha/2$ at high frequency as predicted by (6.38). The measured linewidth enhancement factor is found to be α = 6.6 (20°C), 4 (40°C), 4 (60°C), and 5.6 (80°C), respectively. The α is smaller at high temperatures than that at room temperature. The reason for smaller α at high temperatures, as we can see in the next section, is due to the increase of wavelength detune at high temperature (Fig. 6.15). By carefully examining the Fig. 6.17, we can see that not all the points satisfy (6.38). That is because in DFB lasers, the exact relation between FM and AM modulations should be derived from rate equations (4.22) and (4.23) which include the LSHB. Although the β/m can be approximately described by (6.38), for some modulation frequencies, the FM modulation is strongly influenced by LSHB and does not satisfy (6.38).

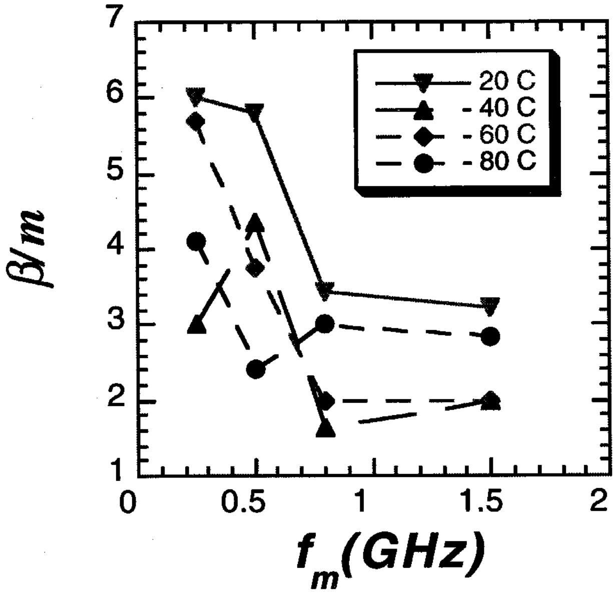

Figure 6.17: Measured *β/m* of 1.3μm InGaAsP/InP QW DFB laser as function of modulation frequency at different temperatures.

6.5.2 Calculation of α factor in uncooled DFB lasers

The effective linewidth enhancement factor in a semiconductor laser generally consists of the interband transition component and free carrier component, which is due to the plasma effect of injected carriers in active layer and the optical confining region.

The α factor can be written as [41,42]

$$\alpha=\alpha_{interband}+\alpha_{free\ carrier} \tag{6.39}$$

The $\alpha_{interband}$ is the interband transition component and can be defined as

$$\alpha_{Interband}=\frac{\partial\chi_r^{Int}}{\partial N}/\frac{\partial\chi_i^{Int}}{\partial N} \tag{6.40}$$

where $\chi^{Int}(N)=\chi_r^{Int}+i\,\chi_i^{Int}$ is the optical susceptibility due to interband transition. The $\alpha_{interband}$ has to be calculated at lasing frequency of a DFB laser which is normally detuned from the gain peak.

The real and imaginary parts of the optical susceptibility are given by [42,43]

$$\chi_i(E,N)=-\Gamma\sum_{i=l,h}\int A_i(\mathbf{E})\,\rho_i^r(\mathbf{E})\,(f_e+f_h-1)\,\frac{\hbar/\tau}{(\hbar/\tau)^2+(\mathbf{E}-E)^2}\,d\mathbf{E} \tag{6.41}$$

$$\chi_r(E,N)=-\Gamma\sum_{i=l,h}\int A_i(\mathbf{E})\,\rho_i^r(\mathbf{E})\,(f_e+f_h-1)\,\frac{\mathbf{E}-E}{(\hbar/\tau)^2+(\mathbf{E}-E)^2}\,d\mathbf{E} \tag{6.42}$$

E is the photon energy, τ is the collisional dephasing time, f_e and f_h are quasi-Fermi distribution functions for electrons and holes, and ρ is the density of states function. $A(E)$ includes the transition dipole moment and the polarization modification factor for the dipole moment in the quantum well structure.

The $\alpha_{interband}$ can be calculated as a function of temperature by using (6.34) and is shown in Fig. 6.18. The calculated $\alpha_{interband}$ decreases with temperature due to the increase of wavelength detune (Fig. 6.15). The DFB laser with large negative wavelength detune has larger differential gain than the one lasing at gain peak (Fig. 6.3), which may contribute to the decline of $\alpha_{interband}$ at high temperatures. The $\alpha_{free\ carrier}$ is due to free carriers in the active layer and barrier layers. It increases with temperature and does not change greatly with wavelength. Combining the contribution from interband transition and that from free carrier, the α parameter reaches its smallest value around 60°C, beyond which $\alpha_{interband}$ changes slowly and the α parameter could increase again due to $\alpha_{free\ carrier}$. This may explain our measured results of α parameter (Fig. 6.17).

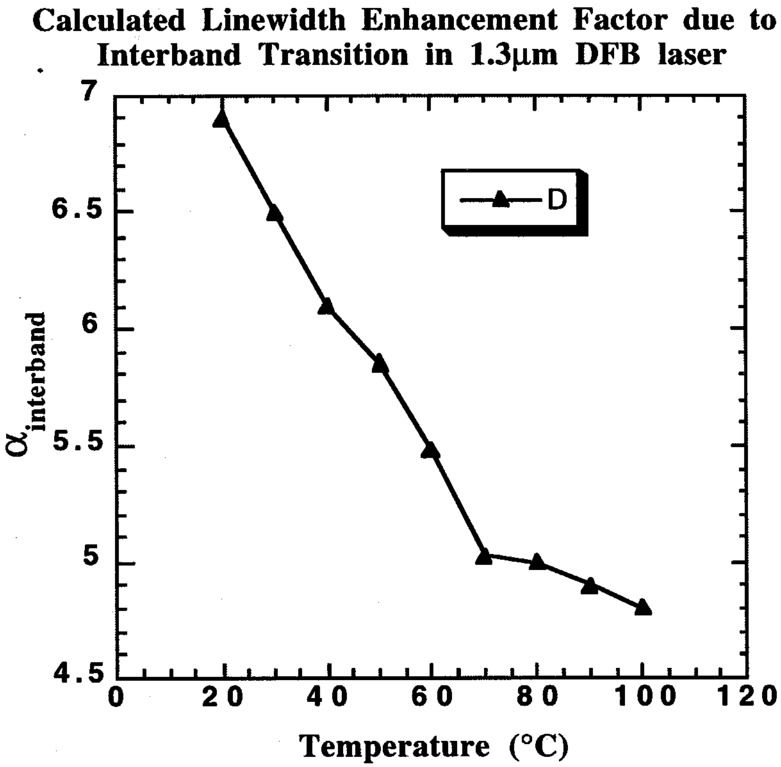

Figure 6.18: Calculated linewidth enhancement factor of 1.3μm DFB laser as function of temperature. The wavelength detune used in the calculation is from the experimental results (Fig. 6.15).

6.5.3 Linewidth of uncooled DFB lasers

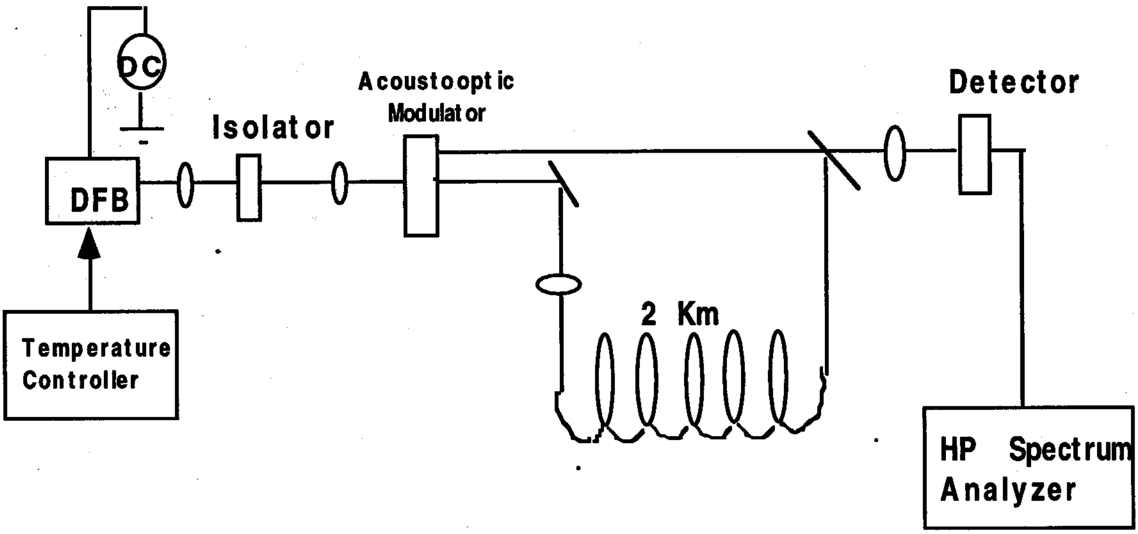

Figure 6.19: The experimental setup for linewidth measurement.

A time delay self-heterodyne detection scheme is used in our measurement of laser linewidth. The laser is isolated and an acoustooptic (A-O) modulator is used to modulate the laser at 85 MHz. The experimental setup for linewidth measurement is shown in Fig. 6.19, and measured linewidth for the 1.3μm 10 QW DFB laser is in Fig. 6.20. We can see that the linewidth is generally proportional to P^{-1} and there is enhancement of linewidth at large optical power for low temperatures. The possible causes for the enhancement have been mentioned in Chapter 4. Due to decreasing external differential quantum efficiency at high temperatures, we haven't injected sufficient current into the laser to observe the enhancement of linewidth in order to avoid damaging the laser.

From Fig. 6.20, the smallest linewidth is obtained as 1.8 MHz at 20°C, 1.5 MHz at 40°C, 1 MHz at 60°C, and 1.2 MHz at 80 °C, respectively. From expression (4.50) for linewidth in DFB lasers and the measured α parameter (Fig. 6.17), it is not difficult to understand that, in a DFB laser with wavelength detuning, the linewidth could be smaller at high temperatures.

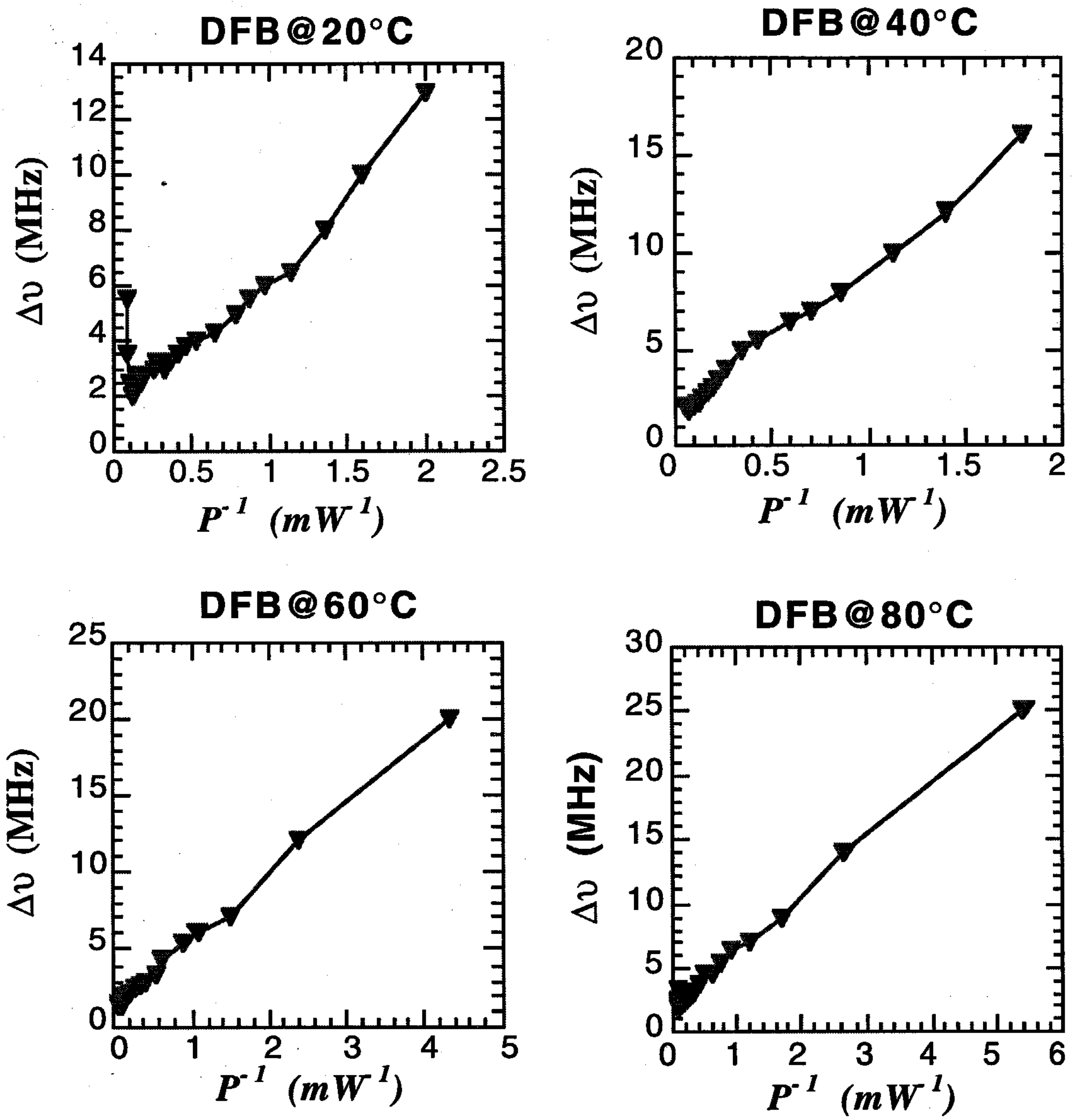

Figure 6.20: Measured linewidth of 1.3μm InGaAsP/InP QW DFB laser vs. the inverse of optical power at 20°C, 40°C, 60°C, and 80°C.

6.6 High speed response of uncooled DFB lasers

In low optical power limit, we have simplified expression (4.38) for resonance frequency in an uncooled DFB laser as [44]

$$\overline{\omega}_R^2(T) \approx \eta\, v_g^2\, [dg(T)/dN]\, \overline{g(T)}\, \overline{S_0} \tag{6.43}$$

Here the differential gain *dg/dN* and threshold gain *g* are both dependent on temperature. In FP lasers, the high speed performance deteriorates at high temperature due to the reduction of the differential gain. In DFB lasers, wavelength detune plays an important role in the high speed response of the lasers. Due to increasing detune over high temperature, the differential gain does not drop as fast as that at the gain peak. We calculate the product of the differential gain and threshold gain for several detuned DFB lasers with increasing temperature. The DFB lasers lase at 1.29μm, 1.30μm, 1.31μm, and they are detuned at $\Delta\lambda_D=\lambda_{lase}-\lambda_{gain\ peak}$=-20nm, -10nm, and -3nm, respectively. The 1.29μm laser with the largest detune among the three lasers has the largest *[dg/dN g]* at room temperature, and the 1.31μm laser, which is the least detuned, has the smallest *[dg/dN g]*. When we increase temperature, the *[dg/dN g]* of 1.29 μm laser has the fastest dropping rate, while the *[dg/dN g]* of 1.31 μm laser only changes slightly. This means that for high temperature application of uncooled DFB lasers, we have to optimize the wavelength detune to achieve the best high speed performance over extensive temperature range.

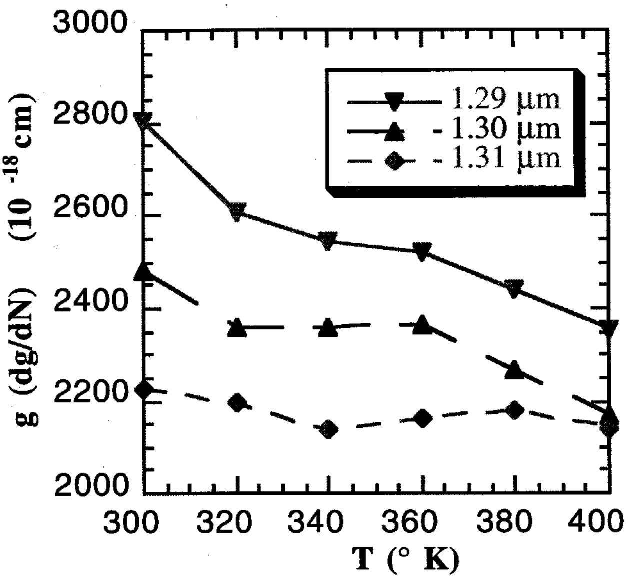

Figure 6.21: The calculated *dg/dN •g* as function of temperature in DFB lasers with various wavelength detunes ($\Delta\lambda_D=\lambda_{lase}-\lambda_{gain\ peak}$=-20nm for 1.29μm laser, -10nm for 1.3μm laser, and -3nm for 1.31μm laser, respectively).

Two DFB lasers (1.29μm and 1.30 μm) have been fabricated to compare their high speed performances at high temperature. The DFB lasers have wavelength detune of $\Delta\lambda_D$=-10 nm (for 1.29μm laser), and -5 nm (for 1.30μm laser).

The measured high speed response of 1.3 μm laser is shown in Fig. 6.22 for various temperatures. The resonance frequency is approximately to be

$$f_R(GHz) \approx 2\sqrt{P}(mW^{1/2}) \text{ for all temperatures.} \qquad (6.44)$$

From (6.43), the resonance frequency can be expressed as

$$f_R=AP^{1/2} \tag{6.45}$$

where

$$A= C\ v_g^2\, dg/dN\, g \tag{6.46}$$

Here C is a constant dependent on the facet reflectivity of the laser.

From the experimental results, the *[dg/dN g]* changes little with increase of temperature, which agrees with our calculation of 1.31μm DFB laser (Fig. 6.22), which has detune of $\Delta\lambda_D$=-3 nm.

The measurement of 1.29μm DFB laser is shown in Fig. 6.23. The resonance frequency has relation with optical power as

$$f_R(GHz) \approx 3.5\sqrt{P}(mW^{1/2}) \text{ at } 20°\text{C}. \tag{6.47}$$

But A drops from *3.5 GHz/mW*$^{1/2}$(20°C) to *2.4 GHz/mW*$^{1/2}$ at 80°C. Because 1.29μm laser has larger wavelength detune of 10 nm, *[dg/dN g]* will drop as temperature increases (Fig. 6.23). The reduction of A is predicted in our calculation of detuned DFB lasers (Fig. 6.21).

It is desirable to achieve fast DFB lasers by using a large detune. From gain curves for various detunes (Fig. 6.3), in order to get threshold gain, we have to inject more current to reach threshold for larger negative wavelength detune. Also, as we have shown in our measurement, the high speed response of the DFB lasers with large negative detune deteriorates faster over high temperature. To achieve the best performance of uncooled DFB lasers, it is necessary to design wavelength detune carefully for specific applications.

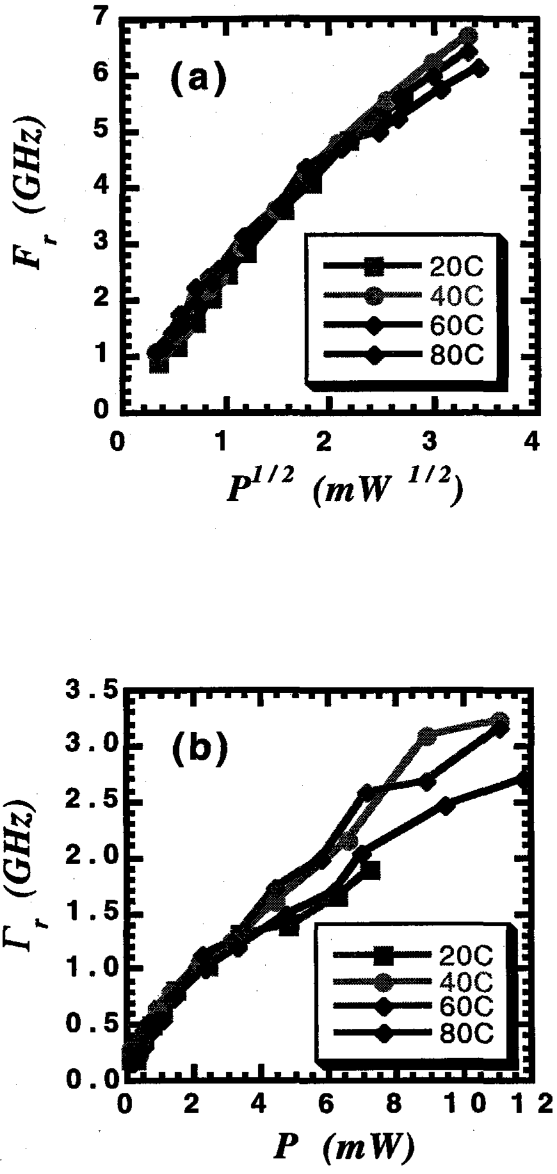

Figure 6.22: (a) The measured resonance frequency as a function of square root of optical power in 1.3μm DFB laser ($\Delta\lambda_D$= -5 nm) for various temperatures; (b) The measured damping rate as function of optical power in 1.3μm DFB laser.

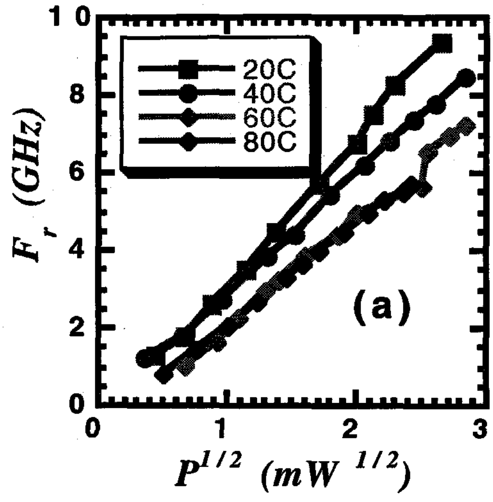

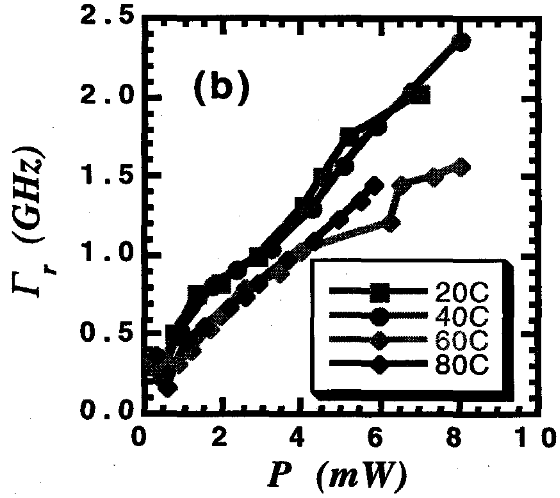

Figure 6.23: (a) The measured resonance frequency as a function of square root of optical power in 1.29μm DFB laser ($\Delta\lambda_D$=-10 nm) for various temperatures; (b) The measured damping rate as function of optical power in 1.29μm DFB laser.

6.7 Conclusion

In this chapter a detailed study of spectral dynamics and high speed response of uncooled DFB lasers has been presented. The most distinguished element differentiating the uncooled DFB lasers from uncooled FP lasers is that in uncooled DFB lasers, the wavelength detune plays an important role in determining their spectral and high speed characteristics at high temperatures. In uncooled DFB lasers, the linewidth actually decreases with increasing temperature due to the increasing wavelength detune at high temperature. The increase of the wavelength detune is mostly contributed by the shift of the gain peak to the longer wavelength at high temperatures. To achieve the best high speed performance of uncooled DFB lasers, the wavelength detune has to be chosen properly. Choosing a large negative wavelength detune could enhance the high speed performance of an uncooled DFB laser at room temperature. But the penalties for the DFB laser are a slightly higher threshold current at room temperature and fast deteriorating high frequency response at high temperatures. To achieve optimum performance of uncooled DFB lasers, it is necessary to design wavelength detune carefully based on their specific applications and requirements for threshold current and high speed performance. A computer model for the uncooled DFB lasers has been used to calculate high speed responses of two lasers with different wavelength detunes. By including LSHB and wavelength detune, the model can give us a satisfactory explanation for the results from our high speed measurement of the uncooled DFB lasers.

Reference

[1] C.E. Zah, R. Bhat, B. Pathak, F. Favire, W. Lin, M.C. Wang, N.C. Anderadakis, D.M. Hwang, M.A. Koza, T.P. Lee, Z. Wang, D. Darby, D. Flanders, and J.J. Hsieh, *IEEE J. Quantum Electron.,* **QE-30**, 511 (1994)

[2] P.J.A. Thijs, T. van Dongen, L.F. Tiemeijer, and J.J.M. Binsma, *IEEE J. Lightwave Technol.* **LT-12**, 28 (1994)

[3] M. Usami, Y. Matsushima, and Y. Takahashi, *Electron. Lett.* 31, 192 (1995)

[4] P.J.A. Thijs, J.J.M. Binsma, E.W.A. Young, and W.M.E. van Gils, *Electron. Lett. 27*, 791(1991)

[5] H. Temkin, D. Coblentz, R.A. Logan, J.P. van der Ziel, T. Tanbun-Ek, R.D. Tadvish, and A.M. Sergent, *Appl. Phys. Lett.* 62, 2402 (1993)

[6] H. Temkin, D. Coblentz, R.A. Logan, J.M. Vandenberg, R.D. Tadvish, and A.M. Sergent, *Appl. Phys. Lett.* 63, 2321 (1993)

[7] T. Namegaya, A. Kasukawa, N. Iwai, and T. Kikuta, *Electron. Lett.* 29, 392 (1993)

[8] T. Fukushima, N. Matsumoto, H. Nakayama, Y. Ikegami, T. Namegaya, A. Kasukawa, and M. Shibata, *IEEE Phot. Tech. Lett.* 5, 963 (1993)

[9] H. Nobuhara, K. Tanaka, T. Yamamoto, T. Machida, T. Fujii, and K. Wadao, *IEEE Phot. Tech. Lett.* 5, 961 (1993)

[10] R.J. Fu, C.S. Hong, E.Y. Chan, D.J. Booher, and L. Figeroa, *IEEE Phot. Tech. Lett.* 3, 308 (1991)

[11] E.P. O'Reilly, and M. Silver, *Appl. Phys. Lett.* 63, 3318 (1993)

[12] A.R. Adams, *Electron. Lett.* 22, 249 (1986)

[13] E. Yablonvitch, and E.O. Kane, *IEEE J. Lightwave Technol.* **LT-6**, 1292 (1988)

[14] Y. Sugiyama, T. Inata, T. Fujii, Y. Nakata, S. Muto, and S. Hiyamizu, *Jpn. J. Appl. Phys.* 25, L648 (1986)

[15] C.G. van de Walle, *Phys. Rev. B* 39, 1871 (1989)

[16] P.W. MacIlroy, A. Kurobe, and Y. Uematsu, *IEEE J. Quantum Electron.,* **QE-21**, 1958 (1985)

[17] G.P. Agrawal and N.K. Dutta, *Long-wavelength Semiconductor Lasers* (Van Nostrand Reinhold, New York, 1986), p. 161

[18] A. Yariv, *Optical Electronics, 4th Editon* (Holt, Rinehart and Winton, New York, 1991), ch. 15

[19] H. Nishimoto, M. Yamaguchi, I. Mito, and K. Kobayashi, *IEEE J. Lightwave Technol.* **LT-5**, 1399 (1987)

[20] M. Asada, K. Kameyama, and Y. Suemastu, *IEEE J. Quantum Electron.,* **QE-20**, 745 (1984)

[21] A. Fortini, D. Diguet, and J. Lugand, *J. Appl. Phys.* 41, 3121 (1978)

[22] K. Masu, E. Tokumitsu, M. Konagai, and K. Takahashi, *J. Appl. Phys.* 54, 5785 (1983)

[23] H.J. Yi, J. Diaz, I. Eliashevich, M. Stanton, M. Erdtmann, X. He, L.J. Wang, and M. Razeghi, *Appl. Phys. Lett.* 66, 253 (1995)

[24] R.I. Taylor, R.A. Abram, M.G. Burt, and C. Smith, *IEE Proc. J. Optoelectron.* 132, 364 (1985)

[25] A. Ghiti, M. Silver, and E.P. O'Reilly, *J. Appl. Phys.* 71, 4626 (1992)

[26] E.P. O'Reilly, and A. R. Adams, *IEEE J. Quantum Electron.,* **QE-30**, 366 (1994)

[27] J. Diaz, I. Eliashevich, H.J. Yi, X. He, M. Stanton, M. Erdtmann, L.J. Wang, and M. Razeghi, *Appl. Phys. Lett.* 65, 2260 (1994)

[28] *QuantumWell Lasers* (Ed. by P. Zory, Academic, San Diego, CA , 1993), p. 315

[29] Y. Zou, J.S. Osinski, P. Grodzinski, P.D. Dapkus, W. C. Rideout, W.F. Sharfin, J. Schlafer, and F.D. Crawford, *IEEE J. Quantum Electron.,* **QE-29**, 1565 (1993)

[30] A. Yariv, *Optical Electronics, 4th Editon* (Holt, Rinehart and Winton, New York, 1991), p. 574

[31] H. Kogelnik, and C.V. Shank, *J. Appl. Phys.* 43, 2327 (1972)

[32] W. Streifer, D.R. Scifres, and R.D. Burnham, *IEEE J. Quantum Electron.,* **QE-13**, 134 (1977)

[33] K. Kojima, K. Kyuma, and T. Nakayama, *IEEE J. Lightwave Technol.* **LT-3**, 1048(1985)

[34] S.L. McCall, and P.M. Platzman, *IEEE J. Quantum Electron.*, **QE-21**, 1899 (1985)

[35] B.W. Hakki, and T.L. Paoli, *J. Appl. Phys.* 46, 1299 (1975)

[36] M. Yamada, and K. Sakuda, *Appl. Opt.* 26, 3474 (1987)

[37] H. Yasaka, K. Takahata, and M. Naganuma, *IEEE J. Quantum Electron.*, **QE-28**, 1294 (1992)

[38] C. Harder, K.Vahala, and A.Yariv, *Appl. Phys. Lett.* 42, 328 (1983)

[39] T. L. Koch, and R. A. Linke, *Appl. Phys. Lett.* 48, 613 (1986)

[40] K. Petermann, *Laser Diode Modulation and Noise* (Kluwer Academic, Dordrecht, The Netherlands, 1991), p. 120

[41] C.H. Henry, R.A. Logan, and K.A. Bertness, *J. Appl. Phys.* 52, 4457 (1981)

[42] K. Vahala, L.C. Chiu, S. Magalit, and A. Yariv, *Appl. Phys. Lett.* 42, 631 (1983)

[43] B. Zhao, T.R. Chen, and A. Yariv, *IEEE J. Quantum Electron.*, **QE-29**, 1027 (1993)

[44] J. Feng, T. R. Chen, and A. Yariv, *Appl. Phys. Lett.* 67, 3706 (1995)